Strategies for Wireless Network Control with Applications to LTE

Von der Fakultät für Elektrotechnik und Informationstechnik
der Rheinisch-Westfälischen Technischen Hochschule Aachen
zur Erlangung des akademischen Grades eines Doktors
der Ingenieurwissenschaften genehmigte Dissertation

vorgelegt von

Master of Science
Xiang Xu

aus China

Berichter: Universitätsprofessor Dr. rer. nat. Rudolf Mathar
Universitätsprofessor Dr.-Ing. Gerd Ascheid

Tag der müdlichen Prüng: 15. December 2014

Diese Dissertation ist auf den Internetseiten der Universitätsbibliothek online verfügbar.

Preface

This thesis was prepared during my time in the DFG Graduate School "Software for Mobile Communication Systems" and at the Institute for Theoretical Information Technology of RWTH Aachen University.

My deep gratitude goes to my supervisor Univ.-Prof. Dr. rer. nat. Rudolf Mathar for the encouragement and support of my work. I am also grateful for the freedom to pursue my own research interests.

Many thanks to Univ.-Prof. Dr.-Ing. Gerd Ascheid for accepting to act as the second referee for this thesis.

I would like to thank Dipl.-Ing. Henning Maier, M.Sc. Omid Taghizadeh and Dipl.-Ing. Florian Schröder for critical reading of this thesis.

I would also like to thank the whole staff of the Institute for Theoretical Information Technology of RWTH Aachen University for providing a pleasant working atmosphere and exchanging interesting ideas.

Finally, I thank my family for being supportive for the last six years.

Aachen, July 2014 Xiang Xu

Contents

1 Introduction **3**

2 Preliminaries **7**
2.1 Wireless communication links 7
2.2 Orthogonal frequency division multiplexing 9
2.3 Multi-antenna transmission 12
2.4 Cellular networks 13
2.5 3GPP LTE 14
2.5.1 System architecture 14
2.5.2 Physical layer transmission 15

3 Link Level Modeling **19**
3.1 Analytical models 19
3.1.1 Rayleigh fading process 19
3.1.2 Kronecker model 22
3.1.3 Weichselberger model 24
3.2 Deterministic models 25
3.3 Geometry-based stochastic channel models 26
3.3.1 Double directional channel model 26
3.3.2 Multi-path component clusterization 27
3.3.3 Standardized models 28
3.4 Semi-stochastic channel model 30
3.4.1 Combining deterministic model and stochastic model 31
3.4.2 Model validation 31
3.4.3 Adaptation to OFDM systems 35
3.4.4 Obtaining geographical information 36

4 Feedback Strategies for Link level Information **39**
4.1 Information feedback in cellular networks 39
4.1.1 LTE resource structure and CQI basics 39
4.1.2 SINR to CQI mapping 42
4.1.3 Throughput and CQI feedback 44
4.2 Channel statistics 46
4.2.1 Expectation of SINR 48
4.2.2 Higher-order moments of SINR 50
4.2.3 Variance of SINR 51
4.2.4 Autocorrelation function of SINR 52

4.2.5 Normalized autocovariance function and its approximation . . . 56
4.2.6 Numerical results . . . 57
4.3 Compensation of temporal variation . . . 59
4.3.1 Prediction accuracy and throughput . . . 60
4.3.2 Average bandwidth efficiency . . . 61
4.3.3 Prediction schemes for CQI feedback . . . 62
4.3.4 Numerical results . . . 67
4.3.5 Prediction noise and Gaussian approximation . . . 67
4.4 Channel prediction in the presence of HARQ . . . 72
4.4.1 HARQ basics . . . 72
4.4.2 HARQ in LTE . . . 74
4.4.3 CQI feedback with different QoS constraints . . . 75
4.4.4 Numerical results . . . 78
4.5 Multi-user system . . . 82
4.5.1 Multi-user resource allocation . . . 82
4.5.2 Numerical results . . . 83

5 Cellular Network Control 87
5.1 Interference management in heterogeneous network through Tx power control . . . 87
5.1.1 System model . . . 89
5.1.2 Autonomous Tx power control . . . 93
5.1.3 Numerical results . . . 97

6 Conclusion and Outlook 105
6.1 Summary . . . 105
6.2 Outlook . . . 106

A Multivariate Gaussian integral 107

Notation 109

Abbreviations 113

List of Tables 117

List of Figures 119

Bibliography 121

Abc

1 Introduction

With the mass deployment of long-term evolution (LTE) systems, the wireless cellular network has evolved to the 4th generation (4G). The 4G mobile standards aim at providing ubiquitous connectivity and high data rate services. To avoid coverage holes, sophisticated algorithms for antenna tilting, handover and load balancing are implemented. To serve densely located indoor users, small cell technologies are developed. To increase spectrum efficiency, radio resource management is performed. To minimize manual effort in adjusting network performance, self-organizing network (SON) schemes are proposed. All these functionalities make the design of network controlling strategies more challenging than ever. In order to tackle various problems during deployment and operation by numerical analysis, the cellular network has to be modeled properly.

Due to the limitation of the computational power and memory, modeling a cellular network from head to toe is extremely difficult, if possible at all. Therefore, the modeling methodology is usually divided into two levels, namely, link level modeling and network level modeling. Link level modeling concentrates on characterizing communication channels between transmitter-receiver pairs, while network level modeling focuses on describing communication networks on a larger scale.

In this dissertation, strategies on both link and network level for wireless network control are investigated, with emphasising on the application to LTE systems. To accomplish this task, link level modeling of wireless channels is presented first. Based on the link level models, channel state information (CSI) feedback strategies are studied. As a feature of SON, future trends of wireless network control depend heavily on the real time status of the network. A majority of status data comes from user reports. However, due to the inevitable delay of wireless transmission, the feedback information will be outdated. Therefore, proper strategies for compensating the feedback delay are proposed in this dissertation. Furthermore, with the feedback information, self-organizing network control strategies can be deployed. Self-organizing network control strategies cover many different areas including handover optimization, load balancing, neighbor list optimization, etc. In this thesis, a case study is given, where transmit power management is discussed.

A unique point of this dissertation is its matching to the industrial standards made by the 3rd generation partnership project (3GPP). As a standardization body, 3GPP is a collaboration of several telecommunication associations. At the end of last century, Nortel Networks and AT&T Wireless established 3GPP as a strategic initiative to define the 3G standard. Later, this initiative was turned into a larger alliance with many major vendors and operators. Now 3GPP already has six organizational partnerships

across the continents of America, Europe and Asia. Their work is extending from 3G universal mobile telecommunications system (UMTS) to 4G LTE and long-term evolution advanced (LTE-A) and possibly future 5G standards.

3GPP standards are structured as releases. Each release consists of hundreds of individual standard documents and each document may have many revised versions. LTE is firstly specified in Release 8, which by the time of finishing this thesis has already been frozen, such that no further changes will be applied to this release.

By following the 3GPP technical specifications, many realistic constraints in implementing wireless communication systems are considered in this work. Moreover, realistic constraints prevent from getting close to the theoretical optimum. Thus, this dissertation puts more focus on low complexity heuristics, which are relatively easy to implement in real systems.

Due to the author's expertise, this thesis mainly targets at the physical layer related aspects of cellular networks, except for a small part in Chapter 4. The remainder of this dissertation is organized as follows:

In Chapter 2, preparatory information about wireless communications on both link level and network level is given. Basics about some of the key technologies of LTE are explained in this chapter.

For investigating a mobile cellular system, proper modeling of the wireless channel between base stations (BSs) and mobile stations (MSs) is usually the first step. Therefore, the methodology of channel modeling is addressed in Chapter 3, particularly considering multi-antenna transmission. In LTE, to achieve high capacity, up to 4×4 multi-input multi-output (MIMO) systems are supported [8]. And later in LTE-A, it is increased to 8×8 [7]. In this work, different existing MIMO channel models, including analytical models and stochastic models, are explained in detail.

Chapter 4 tackles the problem of imperfect feedback of CSI. The feedback mechanism following the 3GPP LTE standards is first introduced, where the CSI must be compressed to quantized data with a few levels only. Statistical properties of the time varying wireless channel in a multi-cell network are then carefully examined. Using the statistics, novel temporal variation compensation schemes are derived and compared with the conventional ones by numerical simulations. Moreover, the hybrid automatic repeat request (HARQ), which operates in the physical layer but is controlled by the media access control (MAC) layer, is explained in this chapter. HARQ is a retransmission mechanism to offer better error protection. This study also shows the effects of HARQ on feedback strategies.

The main goal of cellular network control is to optimize the network performance in terms of key performance indicators (KPIs). The most popular KPIs are capacity and coverage, where capacity indicates the overall throughput in the network and coverage shows the quality of service (QoS) of the users with poor signal reception. In Chapter 5, a case study on heuristic network control strategies is given. In this case study, transmit power management in a heterogeneous network with overlayed macro- and femtocells is investigated. The optimization procedure is based on the user report,

namely, the feedback information discussed in Chapter 4. System level simulators are built to serve the purpose of testing and evaluating the algorithms.

Finally, in Chapter 6, conclusions are given. And last but not least, the evolution of wireless communication does not stop at the 4th generation. Many efforts are made to improve the technology of wireless communications, which is shaping the society and people's daily life in a unprecedented manner. Therefore, some outlooks on potential advances of wireless technology are presented in this chapter.

Parts of this thesis and related topics have already been published in [19] [29] [43] [64] [93] [94] [95] [96] [97] [98] [99] [100] [101] [102]. A number of further publications based on this work is in preparation.

2 Preliminaries

In this chapter, some important facts of wireless networks are introduced. Firstly, the basic mathematical representation of a wireless communication link is described in Section 2.1. Secondly, the transmission technology of orthogonal frequency division multiplexing (OFDM) is presented in Section 2.2. Furthermore, multiple antenna techniques are explained in Section 2.3. Finally, the wireless cellular network is briefly discussed in Section 2.4.

2.1 Wireless communication links

A simple communication link consists of three parts, namely, transmitter, receiver and communication channel in between. The most fundamental question in wireless communications is how to recover the transmitted signals at the receiver side, or in another word, to remove the distortion caused by the communication channel.

In wireless communication systems, while the transmitter and receiver can be designed and controlled, the wireless channel can not be manipulated. Thus, in scientific works, accurate channel models are desired, in order to recreate a close-to-reality environment for testing ideas and developing new concepts.

In a single antenna system, the baseband received signal after multi-path propagation can be written as:

$$y(t) = \int_0^{\tau_{\max}} h(t,\tau)x(t-\tau)\mathrm{d}\tau + w(t), \tag{2.1}$$

where $x(t) \in \mathbb{C}$ is the transmitted (Tx) symbol, $y(t) \in \mathbb{C}$ is the received (Rx) symbol, $w(t) \in \mathbb{C}$ is the additive white Gaussian noise (AWGN) term, $h \in \mathbb{C}$ is the channel impulse response (CIR), $\tau_{\max}$ is the maximum delay spread, t denotes time and τ is delay. Due to the movement of the mobile stations and multi-path propagation, the CIR has a two dimensional structure, as depicted in Fig. 2.1, where time t and delay τ are normalized by symbol duration T and sampling interval T_s, respectively.

In wide-band communication systems, a wireless channel can be modeled by a tapped delay line with irregularly spaced tap delays. Each channel tap is the superposition of a large number of scattered plane waves that arrive with approximately the same delay. The wide-band channel has a time-variant impulse response, which can be written as

$$h(t,\tau) = \sum_{l=1}^{L} \xi_l(t)\delta(\tau - \tau_l), \tag{2.2}$$

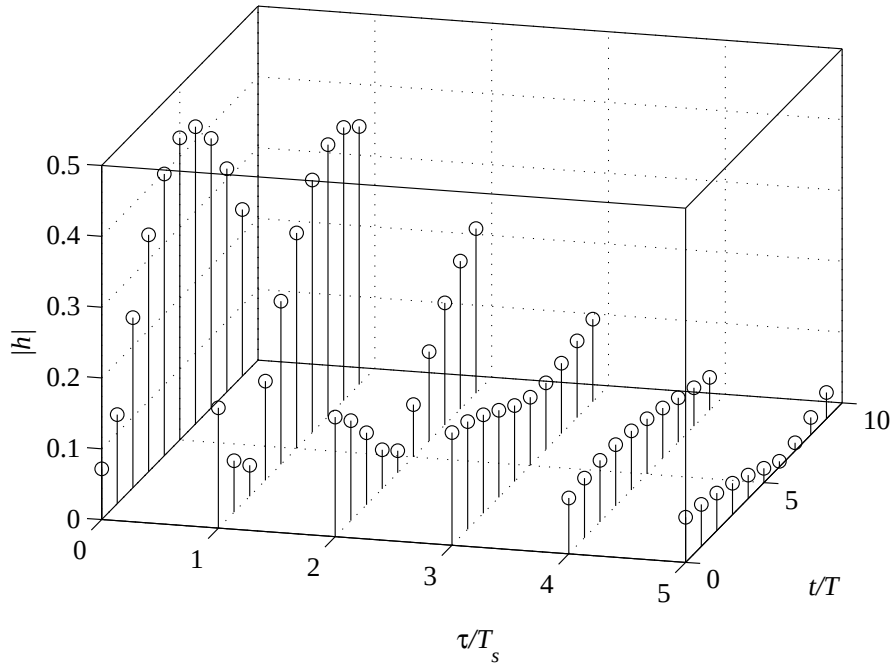

Figure 2.1: Two dimensional structure of channel impulse response.

where ξ is the time-varying complex amplitude, L is the total number of taps, l is the index tap and τ_l is the delay of the lth tap.

An important class of channels is widely used, where taps with different propagation delays are uncorrelated and the complex amplitude is a wide-sense stationary process. This class of channels is referred to as wide-sense stationary uncorrelated-scattering (WSSUS) channels. In WSSUS channels, $\xi_l(t)$'s are wide-sense stationary (WSS) complex Gaussian processes and independent for different taps with average power σ_l^2. The average power of each tap σ_l^2 is usually described by the power-delay profile (PDP) as shown in Fig. 2.2. Furthermore, $\xi_l(t)$ is generally assumed to have the same correlation function $r_{\mathrm{t}}(\Delta t)$. Hence

$$R_{\xi_l\xi_l}(\Delta t) \triangleq \mathrm{E}\{\xi_l(t)\xi_l^*(t+\Delta t)\} = \sigma_l^2 r_{\mathrm{t}}(\Delta t), \tag{2.3}$$

where $R_{\xi_l\xi_l}$ is the auto-correlation function (ACF) of ξ_l, $(\cdot)^*$ is the complex conjugate.

A special case of WSSUS model is often considered, where there is no line of sight (LoS) between the transmitter and receiver. The signal envelope follows a Rayleigh distribution, thus, this model is referred as Rayleigh fading. Using Clarkes' isotropic scattering model [21], the temporal correlation function can be obtained as

$$r_{\mathrm{t}}(\Delta t) = J_0(2\pi f_{\mathrm{D}} \Delta t), \tag{2.4}$$

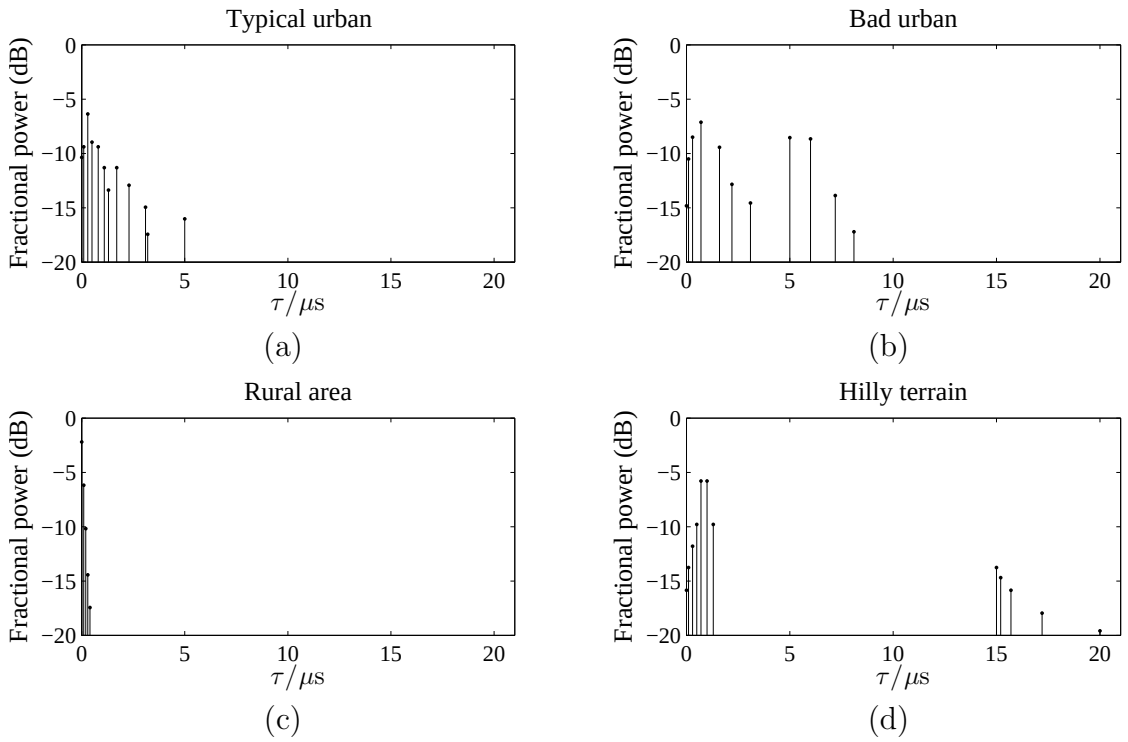

Figure 2.2: Power-delay profile for (a) typical urban, (b) bad urban, (c) rural area, (d) hilly terrain, from COST 207 [30]. The figures show the average power for each tap, normalized by the total power.

where $J_0(x) = \sum_{m=0}^{\infty} \frac{(-1)^m}{m!\Gamma(m+1)} \left(\frac{x}{2}\right)^{2m}$ is the zero order Bessel function of the first kind, f_D is the maximum Doppler frequency. f_D is associated with the carrier frequency f_c and moving speed of the MS v by

$$f_\mathrm{D} = \frac{v}{c} f_\mathrm{c}, \tag{2.5}$$

where c is the speed of light.

2.2 Orthogonal frequency division multiplexing

In wide-band wireless communications, due to multipath propagation, the channel frequency response (CFR) is generally not flat. The frequency fluctuation causes erroneous Rx signal, which can be compensated with OFDM [53]. In OFDM, the transmission frequency band is divided into K equally spaced subbands, such that in each subband the frequency response is nearly flat.

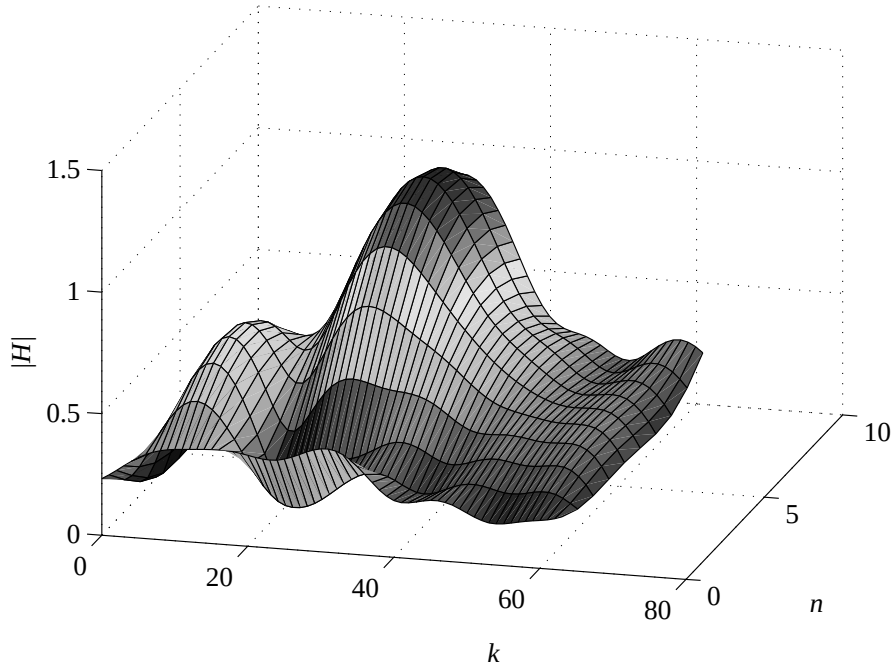

Figure 2.3: Two dimensional structure of CFR corresponds to CIR in Figure 2.1

In practice, the Tx signal x is obtained by the inverse discrete Fourier transform (IDFT). The frequency domain discrete Tx signal can be written as

$$\begin{aligned} X[n,k] &= \sum_{m=0}^{K-1} x(nT + mT_{\mathrm{s}}) \exp\left\{-\jmath 2\pi k m \Delta f T_{\mathrm{s}}\right\} \\ &= \sum_{m=0}^{K-1} x(nT + mT_{\mathrm{s}}) \exp\left\{-\jmath 2\pi \frac{km}{K}\right\}, \end{aligned} \tag{2.6}$$

where n is discrete the time index and k is the subcarrier index. And the sampling interval T_{s} is defined as T/K. $X[n,k]$ can be recovered at the Rx side by the discrete Fourier transform (DFT). If K is a power of two, DFT and IDFT can be efficiently implemented using the fast Fourier transform (FFT). To avoid inter-carrier interference, the subcarrier spacing has to satisfy the orthogonality condition

$$\Delta f \triangleq \frac{1}{T}. \tag{2.7}$$

Suppose the delay taps are on the sampling grid with sampling rate T_{s}

$$\tau_l = lT_{\mathrm{s}}, \tag{2.8}$$

the CFR of the kth subcarrier can be written as

$$H(t,k) = \sum_{l=1}^{L} \xi_l(t) \exp\left\{-\jmath 2\pi \frac{k\tau_l}{T}\right\} \tag{2.9}$$

$$= \sum_{l=1}^{L} \xi_l(t) \exp\left\{-\jmath 2\pi \frac{kl}{K}\right\}, \tag{2.10}$$

and the corresponding discrete CFR of the nth OFDM block can be written as

$$H[n,k] = \sum_{l=1}^{L} \xi_l(nT) \exp\left\{-\jmath 2\pi \frac{kl}{K}\right\}. \tag{2.11}$$

The corresponding CFR of the CIR from Figure 2.1 with 64 subcarriers is shown in Figure 2.3, where it can be seen that the fluctuation within one subcarrier is much smaller than within the whole frequency band. This property leads to simplification of equalization. And it also enables radio resource allocation.

Consider time indices t_1, t_2 and subcarrier k_1, k_2, the correlation function of the CFR for different times and frequencies is

$$\begin{aligned}
& \mathrm{E}\left\{H(t_1,k_1)H^*(t_2,k_2)\right\} \\
= \; & \mathrm{E}\left\{\sum_{l=1}^{L}\sum_{m=1}^{L} \xi_l(t_1)\xi_m^*(t_2) \exp\left\{-\jmath 2\pi \frac{k_1 l}{K}\right\} \exp\left\{\jmath 2\pi \frac{k_2 m}{K}\right\}\right\} \\
= \; & r_{\mathrm{t}}(t_2 - t_1) \sum_{l=1}^{L} \sigma_l^2 \exp\left\{-\jmath 2\pi \frac{(k_2-k_1)l}{K}\right\} \\
= \; & r_{\mathrm{t}}(\Delta t) r_{\mathrm{f}}[\Delta k],
\end{aligned} \tag{2.12}$$

where $\Delta t = t_2 - t_1$, $\Delta k = k_2 - k_1$ and $r_{\mathrm{f}}[\Delta k]$ is the discrete frequency correlation function, defined as

$$r_{\mathrm{f}}[\Delta k] \triangleq \sum_{l=1}^{L} \sigma_l^2 \exp\left\{-\jmath 2\pi \frac{\Delta k l}{K}\right\}. \tag{2.13}$$

From (2.12), it is clear that the correlation in time and frequency domain can be decoupled, and the frequency correlation depends on the PDP.

Moreover, OFDM can be extended to multiple users, with each user using a subset of the subbands. This multiple access scheme is called orthogonal frequency division multiple access (OFDMA). Due to their unique advantages, OFDM and OFDMA are adopted for many industrial standards, such as LTE, wireless local area network (WLAN) and digital video broadcasting - terrestrial (DVB-T). Thus, in the foreseeable future, OFDM and OFDMA will be the dominant technology in wireless communications.

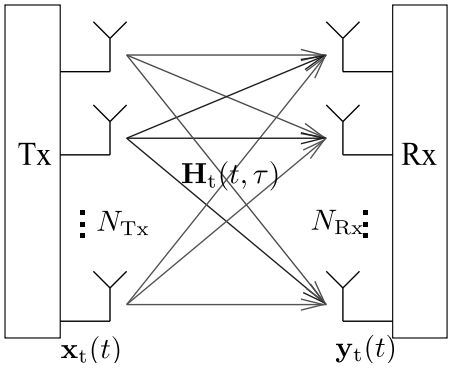

Figure 2.4: MIMO channel

2.3 Multi-antenna transmission

Another trend in wireless communications is MIMO transmission. Using multiple Tx and Rx antennas, the energy efficiency and spectral efficiency can be improved significantly [31] [83]. Consider a MIMO channel with N_{Tx} Tx antennas and N_{Rx} Rx antennas, as shown in Figure 2.4, the wireless channel can be expressed in matrix form

$$\mathbf{H}_{\mathrm{t}}(t,\tau) = \begin{pmatrix} h_{1,1}(t,\tau) & h_{1,2}(t,\tau) & \cdots & h_{1,N_{\mathrm{Tx}}}(t,\tau) \\ h_{2,1}(t,\tau) & h_{2,2}(t,\tau) & \cdots & h_{2,N_{\mathrm{Tx}}}(t,\tau) \\ \vdots & \vdots & \ddots & \vdots \\ h_{N_{\mathrm{Rx}},1}(t,\tau) & h_{N_{\mathrm{Rx}},2}(t,\tau) & \cdots & h_{N_{\mathrm{Rx}},N_{\mathrm{Tx}}}(t,\tau) \end{pmatrix}, \tag{2.14}$$

where $h_{n_{\mathrm{Rx}},n_{\mathrm{Tx}}}$ represents the channel between the n_{Rx}th Rx antenna and n_{Tx}th Tx antenna. Similar to (2.1), the received symbols can be described in the vector form:

$$\mathbf{y}_{\mathrm{t}}(t) = \int_0^{\tau_{\max}} \mathbf{H}_{\mathrm{t}}(t,\tau)\mathbf{x}_{\mathrm{t}}(t-\tau)\mathrm{d}\tau + \mathbf{w}_{\mathrm{t}}(t), \tag{2.15}$$

with

$$\mathbf{y}_{\mathrm{t}}(t) = \begin{pmatrix} y_1(t) \\ y_2(t) \\ \vdots \\ y_{N_{\mathrm{Rx}}}(t) \end{pmatrix}, \mathbf{x}_{\mathrm{t}}(t) = \begin{pmatrix} x_1(t) \\ x_2(t) \\ \vdots \\ x_{N_{\mathrm{Tx}}}(t) \end{pmatrix}, \mathbf{w}_{\mathrm{t}}(t) = \begin{pmatrix} W_1(t) \\ W_2(t) \\ \vdots \\ W_{N_{\mathrm{Rx}}}(t) \end{pmatrix} \tag{2.16}$$

being the Rx symbol vector, Tx symbol vector and AWGN vector, respectively.

Although the energy and spectral efficiency can be improved by using multiple antennas, for wide-band MIMO transmission with larger numbers of antennas, the equalization problem can become increasingly difficult. Therefore, OFDM and MIMO techniques are often combined into MIMO-OFDM systems, in which the CFR is quasi-constant for each subband, and equalization can be done in the frequency domain [93].

Using (2.6) and (2.11), the received signal vector in frequency domain can be written as

$$\mathbf{y}_{\mathrm{f}}[n,k] = \mathbf{H}_{\mathrm{f}}[n,k]\mathbf{x}_{\mathrm{f}}[n,k] + \mathbf{w}_{\mathrm{f}}[n,k], \tag{2.17}$$

where $\mathbf{y}_{\mathrm{f}}$, $\mathbf{x}_{\mathrm{f}}$ $\mathbf{w}_{\mathrm{f}}$ are vectors collecting the frequency domain Rx, Tx signals and AWGN, respectively. Elements of CFR matrix $\mathbf{H}_{\mathrm{f}}$ are the IDFT of $\mathbf{H}_{\mathrm{t}}$ as defined in (2.11).

In addition to the two dimensional structure described in Figure 2.3, MIMO-OFDM channels have the third dimension of space. The spatial correlation can degrade the channel capacity [47], thus, should be properly described. Models for spatial correlation are elaborated in Chapter 3.

2.4 Cellular networks

Cellular networks are one of the most widely deployed wireless communication networks. Figure 2.5 shows the common layout of a cellular network. Typically, a cellular network consists a number of BSs and a big amount of MSs. The behavior of the network depends on many facts, such as the distribution, movement and service types of the MSs, the antenna tilts, Tx power of the BSs, etc. Theoretical analysis of such complex system is usually very difficult, thus, computer simulation is quite commonly used. Moreover, due to the large amount of entities in the network, simulation of the network level cannot cover all the phenomena in the communication links. A higher level of abstraction is desirable.

In link level modeling, the wireless channel is characterized by the relative location and velocity of the user, number and orientations of the antennas, frequency and bandwidth of the signal, as well as the propagation environment. In network level modeling, all the factors that affect the channel condition are translated into a measure of CSI. Furthermore, in a multi-cell network, the CSI takes also the interferences from neighboring cells into consideration. Signal to interference plus noise ratio (SINR) is a common measure of the CSI. For an OFDM system, the SINR of user i served by base station s at time t and subcarrier k can be written as

$$\gamma_{i,s}(t,k) = \frac{P_{i,s}(t,k)}{\sum\limits_{j\in\mathcal{S}\setminus s} P_{i,j}(t,k) + \sigma_w^2}, \tag{2.18}$$

where P is the Rx power and σ_w^2 is the noise power, $\mathcal{S}$ is the set of all the cells within the network.

Theoretically, the CSI should be given as input to the cellular network control entities. However, in practice, this information is typically unavailable at the BS and must be provided by the MS periodically through a feedback channel. From the aforementioned wireless communication links, a dilemma arises. On one hand, due to the doubly selectivity of the channel, optimizing the cellular network requires as much and as detailed information as possible. And on the other hand, a large amount of feedback information leads to a large packet overhead, which deteriorates the spectral efficiency.

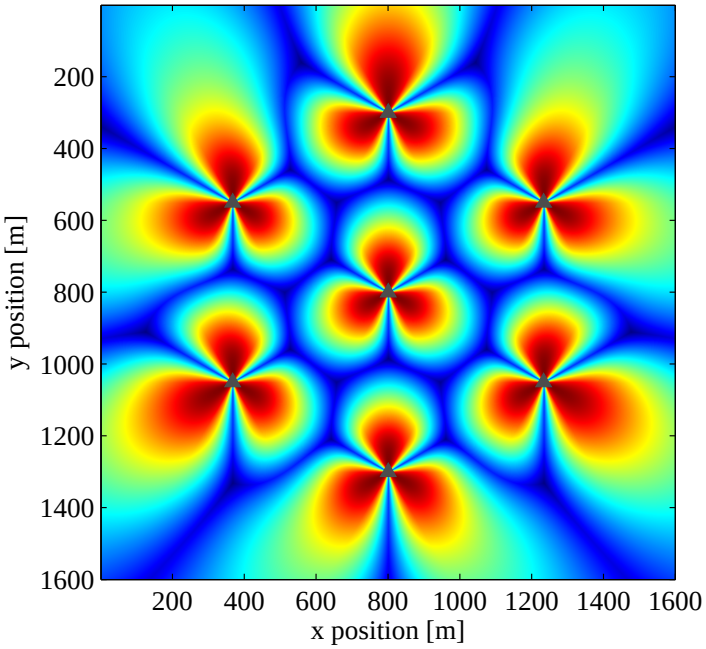

Figure 2.5: Rx signal level of a network with 7 base stations and 21 cells in hexagonal layout, where the basestations are located on the joints of the hexagonal cells

In the current LTE standards, the CSI is compressed for different subcarrier before the feedback process. The influence of CSI feedback is elaborated in Chapter 4. With the CSI available at the BS, the cellular network can be optimized through network control strategies, such as radio resource allocation, handover optimization, antenna tilt and Tx power management, etc.

2.5 3GPP LTE

An important part of this thesis are physical layer downlink control strategies based on the user reported CSI, especially with application to LTE systems.

To comply with the standards, some LTE terminologies are used in this thesis, e.g. the base stations is called evolved node B (eNB) and the mobile station is called user equipment (UE).

2.5.1 System architecture

Comparing with older generations, LTE does not only offer a new radio interface but also a new system architecture. 3GPP specifies the system architecture evolution (SAE) in Release 8. As an all-IP system, there is no more circuit switching center

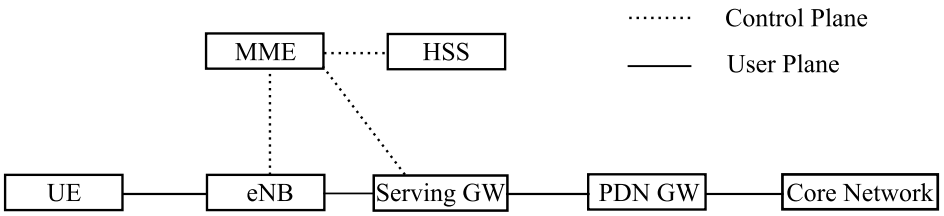

Figure 2.6: LTE system architecture

in LTE. To reduce latency, the architecture of LTE is flatter than of older systems. Especially for the user plane (UP), data can be directly passed from BSs to gateways without going through a control entity [39].

The network architecture of LTE is illustrated in Figure 2.6, where the UE is connected to some eNB via evolved universal terrestrial radio access (E-UTRAN). In the user plane, data is sent to some serving gateway (S-GW), which is the mobile anchor point. The S-GW is in charge of inter-eNB handover, downlink packet buffering, initiation of network-triggered service requests, etc. The S-GW is connected to a PDN gateway (P-GW), where the IP address of UE is allocated. Through the P-GW, the data finally reaches the core network.

In the control plane, the mobility management entity (MME) is the main control unit. Main functions of the MME include authentication and mobility management. Basically, MME is a server identifies the UE, request proper resources in the eNB for the UE and decides which S-GW the UE is connected to. To engage authentication and mobility management functions, the MME has to request subscription data from the home subscription server (HSS), which is a repository for all permanent user data.

2.5.2 Physical layer transmission

In the LTE downlink, user data is transmitted via the physical downlink shared channel (PDSCH) and control information is transmitted via the physical downlink control channel (PDCCH). The following procedure is applied to the downlink user data [11]:

Transport Block Cyclic redundancy check (CRC) Attachment: A 24-bit CRC message of the whole transport block is calculated and attached, where CRC is for error detection at the Rx side.

Code Block Segmentation and Code Block CRC Attachment: The transport block attached with CRC bits is chopped up in to smaller blocks and each block is attached with another 24-bit CRC. To fit into the turbo interleaver, the minimum and maximum block size is 40 bits and 6144 bits including the CRC bits, respectively. Moreover, filler bits are appended to the start of the first segment to match the turbo interleaver.

Turbo Encoding: Turbo coding is applied to each segment to enhance error performance [17]. The turbo encoder is a parallel concatenated convolutional code (PCCC) with two recursive convolutional encoders and a quadratic permutation polynomial (QPP) interleaver [65].

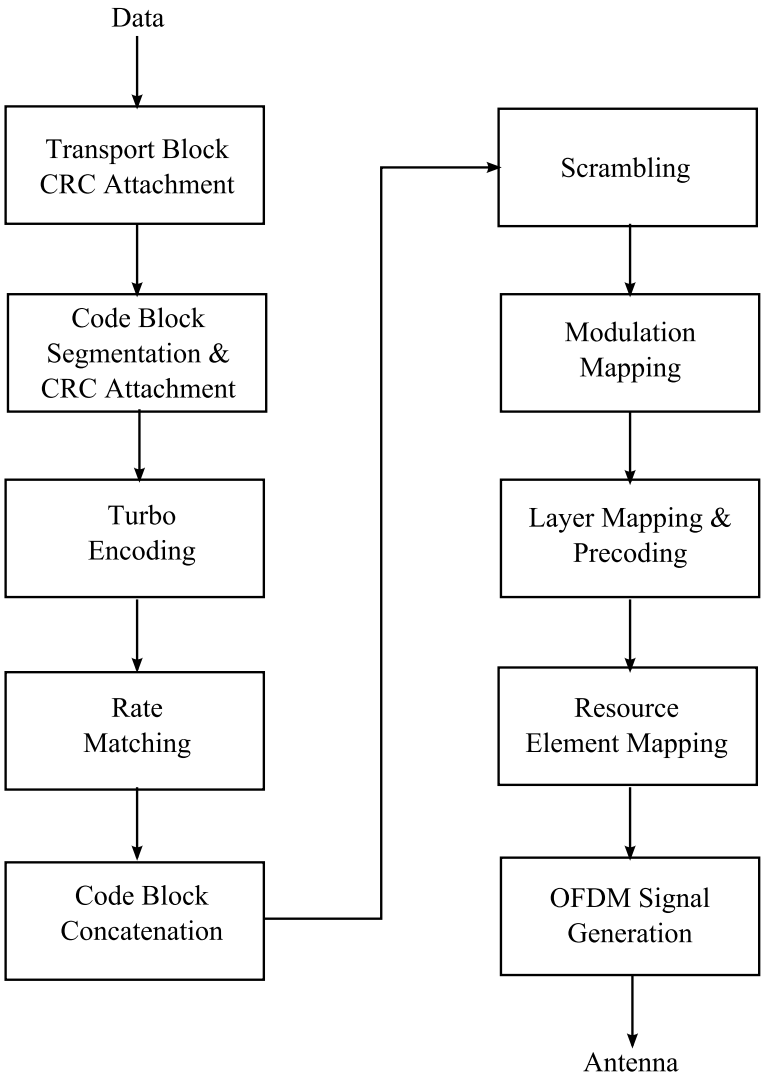

Figure 2.7: LTE downlink signal generation

Rate Matching: The encoded streams are further processed by a rate matching algorithm. Together with the turbo encoder, the rate matching algorithm is capable of producing any arbitrary rate to match for the transmission resources [20].

Code Block Concatenation: The output blocks of rate matching are sequentially concatenated to create the final output of channel coding.

Scrambling: The codewords are bit-wise multiplied by an orthogonal sequence and a user-specific pseudo-random scrambling sequence. The purpose of scrambling is to suppress inter-cell interference (ICI). Since the scrambling sequence is pseudo-random and user-specific, signals from interfering cells can not be descramble correctly. The result is an uncorrelated, noise-like sequence.

Modulation Mapping: The scrambled codewords are modulated to complex valued symbols with quadrature phase shift keying (QPSK), 16-quadrature amplitude modu-

lation (QAM) or 64-QAM. The modulation scheme is chosen to adapt to the channel condition.

Layer Mapping and Precoding: Since MIMO transmission is adopted in LTE, the complex symbols are mapped onto 1, 2 or 4 spatial layers and multiplied with the precoding matrix, depending on the number of Tx antennas. For single antenna transmission, layer mapping and precoding is a dummy process with the output equal to the input. For multiple Tx antennas, the mapping and precoding scheme depends on the number of antennas as well as the MIMO transmission mode, which can be either transmit diversity or spatial multiplexing.

Resource Element Mapping: A Resource Element (RE) is the smallest defined unit which consists of one OFDM sub-carrier during one OFDM symbol interval. For each antenna port, the resource elements which are not occupied by other control channels can be used for PDSCH. The symbols are mapped sequentially to the available resource elements from the first to the last subcarrier in the first OFDM symbol, and this process goes on in the remaining OFDM symbols until there is no symbol left.

OFDM Signal Generation: With the resource elements filled with data symbols, OFDM signal can be generated with inverse fast Fourier transform (IFFT).

The whole procedure is summarized in Figure 2.7 and more details can be found in [6].

3 Link Level Modeling

This chapter introduces link level modeling, especially for MIMO transmission. As the fundamental part of characterizing wireless communication systems, channel models can be categorized into analytical models and geometry-based models. Analytical models emphasize correlation properties, whereas the geometry-based models try to describe the influence of the spatial environment on the radio wave.

Furthermore, geometry-based models can be divided into deterministic models and stochastic models. Moreover, a semi-stochastic model, which is a hybrid of the deterministic and stochastic model, is also presented in this chapter.

Parts of this chapter have been published in [97],[93], [101], [98], [102] and [19].

3.1 Analytical models

Analytical MIMO channel models specify channel matrices which have correct correlation properties, generated from basic random number generators. Since the correlation functions of the CFR can be decoupled, the procedure of generating channel matrices for MIMO-OFDM systems can be divided into three steps [90]. The first step is to generate independent Rayleigh processes with temporal correlation. The second step is to apply power delay profile (PDP). And the last step is to create a channel matrix with spatial correlation.

3.1.1 Rayleigh fading process

In the ideal case, the CIRs for different Tx-Rx antenna pairs of a MIMO system are independent and identically distributed (i.i.d.). Each channel between antenna pairs can be regarded as a single-input single-output (SISO) channel. This model is also referred to as the i.i.d. model. The generation of i.i.d. channels is rather straight forward. A Rayleigh flat fading CIR with unit variance ζ_l is generated for each of the L taps, and then scaled with the variance σ_l^2 specified in the PDP.

Many different techniques have been proposed to model and simulate mobile radio channels with Rayleigh fading. The most representative models from early years are from Clarke and Gans based on sum of sinusoids [21] [33]. In Clarke's reference model, the electro-magnetic field of the received signal is assumed to be comprised of a number of sinusoidal plane waves with equal average amplitude and different Doppler frequency shifts. The angle of arrivals (AoAs) and phases of these waves are arbitrary [70].

Accordingly, the normalized complex envelope of an arbitrary propagation path l can be written as

$$\zeta_l(t) = \frac{1}{\sqrt{N_{\text{sin}}}} \sum_{n_{\text{sin}}=1}^{N_{\text{sin}}} \exp\left\{\jmath(2\pi f_{\text{D}} t \cos\psi_{l,n_{\text{sin}}} + \Phi_{l,n_{\text{sin}}})\right\}, \tag{3.1}$$

where N_{sin} is the number of sinusoids, n_{sin} is the index of sinusoidal wave, ψ is the random AoA and Φ is the random initial phase. Both ψ and Φ are uniformly distributed over $[-\pi, \pi)$ for all n_{sin}, and they are mutually independent. From the Euler's formula, (3.1) can be expressed with the in-phase and quadrature components

$$\zeta_l(t) = \zeta_{\text{I},l}(t) + \jmath\zeta_{\text{Q},l}(t), \tag{3.2}$$

where the in-phase and quadrature components are given by

$$\zeta_{\text{I},l}(t) = \frac{1}{\sqrt{N_{\text{sin}}}} \sum_{n_{\text{sin}}=1}^{N_{\text{sin}}} \cos\left(2\pi f_{\text{D}} t \cos\psi_{l,n_{\text{sin}}} + \Phi_{l,n_{\text{sin}}}\right) \tag{3.3}$$

$$\zeta_{\text{Q},l}(t) = \frac{1}{\sqrt{N_{\text{sin}}}} \sum_{n_{\text{sin}}=1}^{N_{\text{sin}}} \sin\left(2\pi f_{\text{D}} t \cos\psi_{l,n_{\text{sin}}} + \Phi_{l,n_{\text{sin}}}\right). \tag{3.4}$$

For large N_{sin}, the central limit theorem justifies that $\zeta_{\text{I},l}(t)$ and $\zeta_{\text{Q},l}(t)$ can be treated as Gaussian random processes. When N_{sin} approaches infinity, the autocorrelation of ζ_l is [81]

$$\begin{aligned} R_{\zeta_l\zeta_l}(\Delta t) &= \text{E}\{\zeta_l(t_1)\zeta_l^*(t_2)\} \\ &= \text{E}\{(\zeta_{\text{I},l}(t_1) + \jmath\zeta_{\text{Q},l}(t_1))(\zeta_{\text{I},l}(t_2) - \jmath\zeta_{\text{Q},l}(t_2))\} \\ &= R_{\zeta_\text{I}\zeta_\text{I}}(\Delta t) + R_{\zeta_\text{Q}\zeta_\text{Q}}(\Delta t) + \jmath(R_{\zeta_\text{Q}\zeta_\text{I}}(\Delta t) - R_{\zeta_\text{I}\zeta_\text{Q}}(\Delta t)), \end{aligned} \tag{3.5}$$

where

$$R_{\zeta_\text{I}\zeta_\text{I}}(\Delta t) = R_{\zeta_\text{Q}\zeta_\text{Q}}(\Delta t) = \frac{1}{2} J_0(2\pi f_{\text{D}} \Delta t) \tag{3.6}$$

$$R_{\zeta_\text{Q}\zeta_\text{I}}(\Delta t) = R_{\zeta_\text{I}\zeta_\text{Q}}(\Delta t) = 0. \tag{3.7}$$

The first part of (3.6) can be proved as follows:

$$\begin{aligned}
R_{\zeta_\mathrm{I}\zeta_\mathrm{I}}(\Delta t) &= \mathrm{E}\{\zeta_\mathrm{I}(t_1)\zeta_\mathrm{I}(t_2)\} \\
&= \frac{1}{N_\mathrm{sin}} \sum_{n_\mathrm{sin}=1}^{N_\mathrm{sin}} \sum_{m_\mathrm{sin}=1}^{N_\mathrm{sin}} \mathrm{E}_{\psi,\Phi}\{\cos\left(2\pi f_\mathrm{D} t_1 \cos\psi_{l,n_\mathrm{sin}} + \Phi_{l,n_\mathrm{sin}}\right) \\
&\quad \cdot \cos\left(2\pi f_\mathrm{D} t_2 \cos\psi_{l,m_\mathrm{sin}} + \Phi_{l,m_\mathrm{sin}}\right)\} \\
&= \frac{1}{2N_\mathrm{sin}} \sum_{n_\mathrm{sin}=1}^{N_\mathrm{sin}} \{\mathrm{E}_\psi\{\cos(2\pi f_\mathrm{D}(t_1 - t_2)\cos\psi_{l,n_\mathrm{sin}})\} \\
&\quad + \mathrm{E}_\psi\{\cos(2\pi f_\mathrm{D}(t_1 + t_2)\cos\psi_{l,n_\mathrm{sin}})\}\mathrm{E}_\Phi\{\cos 2\Phi_{l,n_\mathrm{sin}}\} \\
&\quad + \mathrm{E}_\psi\{\sin(2\pi f_\mathrm{D}(t_1 + t_2)\cos\psi_{l,n_\mathrm{sin}})\}\mathrm{E}_\Phi\{\sin 2\Phi_{l,n_\mathrm{sin}}\}\} \\
&= \frac{1}{2N_\mathrm{sin}} \sum_{n_\mathrm{sin}=1}^{N_\mathrm{sin}} \mathrm{E}_\psi\{\cos(2\pi f_\mathrm{D}\Delta t\cos\psi_{l,n_\mathrm{sin}})\} \\
&= \frac{1}{2N_\mathrm{sin}} \sum_{n_\mathrm{sin}=1}^{N_\mathrm{sin}} \int_{-\pi}^{\pi} \cos(2\pi f_\mathrm{D}\Delta t\cos\psi_{l,n_\mathrm{sin}}) \frac{\mathrm{d}\psi_{l,n_\mathrm{sin}}}{2\pi} \\
&= \frac{1}{2N_\mathrm{sin}} \sum_{n_\mathrm{sin}=1}^{N_\mathrm{sin}} J_0(2\pi f_\mathrm{D}\Delta t) \\
&= \frac{1}{2} J_0(2\pi f_\mathrm{D}\Delta t). \qquad (3.8)
\end{aligned}$$

Similarly, the second part of (3.6) and (3.7) can be proved.

Based on Clarke's reference model, Jakes proposed a simplified simulation model, which has been widely used for decades [45]. In the Jakes' model, the AoA and initial phase are set to

$$\psi_{\mathrm{Jakes},l,n_\mathrm{sin}} = \frac{2\pi n_\mathrm{sin}}{N_\mathrm{sin}}, \qquad (3.9)$$

$$\Phi_{\mathrm{Jakes},l,n_\mathrm{sin}} = 0, \qquad (3.10)$$

and N_sin is taken from

$$N_\mathrm{sin} = 4M_\mathrm{sin} + 2. \qquad (3.11)$$

where M_sin is an integer. The value of M_sin determines the number of summed sinusoids, and thus the statistical property of the model.

Jake's model reduces the number of distinct Doppler frequency shifts from N_sin to $M_\mathrm{sin} + 1$. However, the deterministic nature of the Jakes' simulation model makes it difficult to create multiple uncorrelated fading waveforms for frequency selective channels.

A randomized simulator, which can solve this problem, is proposed by Pop and Beaulieu [69]. Pop and Beaulieu's simulation model also solves the stationarity problem of Jakes' model, but higher-order statistics of this model do not match the desired

ones [104]. This deficiency can be overcome by introducing randomness in path gain, initial phase and Doppler frequency for all individual sinusoids. In [91]. Xiao et al. introduced a simulation model following the principles of Clarke's reference model

$$\zeta_{\mathrm{Xiao},l}(t) = \zeta_{\mathrm{Xiao,I},l}(t) + \jmath\zeta_{\mathrm{Xiao,Q},l}(t) \tag{3.12}$$

$$\zeta_{\mathrm{Xiao,I},l}(t) = \frac{1}{\sqrt{N_{\mathrm{sin}}}} \sum_{n_{\mathrm{sin}}=1}^{N_{\mathrm{sin}}} \cos\left(2\pi f_{\mathrm{D}} t \cos\psi_{\mathrm{Xiao},l,n_{\mathrm{sin}}} + \Phi_{\mathrm{Xiao},l,n_{\mathrm{sin}}}\right) \tag{3.13}$$

$$\zeta_{\mathrm{Xiao,Q},l}(t) = \frac{1}{\sqrt{N_{\mathrm{sin}}}} \sum_{n_{\mathrm{sin}}=1}^{N_{\mathrm{sin}}} \sin\left(2\pi f_{\mathrm{D}} t \cos\psi_{\mathrm{Xiao},l,n_{\mathrm{sin}}} + \Phi_{\mathrm{Xiao},l,n_{\mathrm{sin}}}\right), \tag{3.14}$$

with the AoA generated by

$$\psi_{\mathrm{Xiao},l,n_{\mathrm{sin}}} = \frac{2\pi n_{\mathrm{sin}} + \theta_{l,n_{\mathrm{sin}}}}{N_{\mathrm{sin}}}, \tag{3.15}$$

where $\theta_{l,n_{\mathrm{sin}}}$ and $\Phi_{\mathrm{Xiao},l,n_{\mathrm{sin}}}$ are statistically independent and uniformly distributed over $[-\pi, \pi)$ for all l and n_{sin}.

For systems with L delay taps, N_{Tx} Tx antennas and N_{Rx} Rx antennas, in total $LN_{\mathrm{Tx}}N_{\mathrm{Rx}}$ Rayleigh processes must be independently generated, with the underlying assumption that the normalized temporal correlation function is identical for all resolvable physical multipaths.

Other than sum of sinusoids, IDFT and autoregressive (AR) models are also proposed to create Rayleigh processes [103] [13]. IDFT and AR models have the advantage in computational complexity, however, both of them have limitations on applications. The IDFT method can only work with a relatively large Doppler frequency and FFT size. Whereas AR models have severe numerical problems when the Doppler frequency is small.

Assuming the PDP is identical for all Tx and Rx indices [59], σ_l^2 can be applied to each delay tap l

$$h_{\mathrm{i.i.d.}}(t,\tau) = \sum_{l=1}^{L} \sigma_l \zeta_l(t) \delta(\tau - \tau_l), \tag{3.16}$$

where the relation between σ_l and τ_l is generally given in tables from the PDP. For various wireless networks, specific PDP can be found in many standards [30] [40] [3]. The channel matrix $\mathbf{H}_{\mathrm{iid}}(t,\tau) \in \mathbb{C}^{N_{\mathrm{Rx}} \times N_{\mathrm{Tx}}}$ simply collects the CIRs, and arrange them in an appropriate order.

3.1.2 Kronecker model

The i.i.d. model is mostly favored by theoreticians, due to its mathematical tractability. However, spatial correlation of MIMO channels should not be ignored in the general case, since it has a large impact on the channel capacity [79].

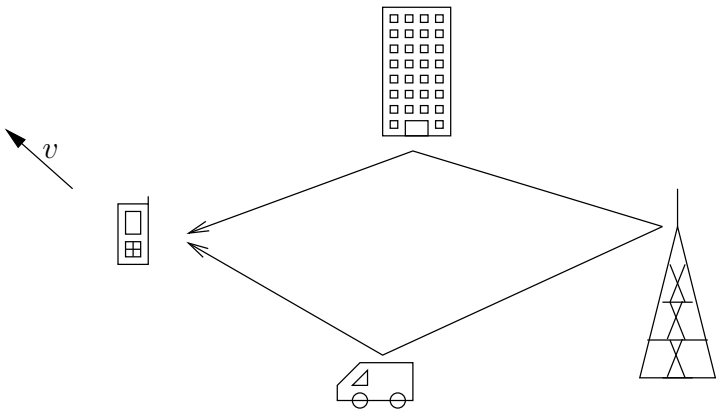

Figure 3.1: Multi-path propagation and movements of mobile station cause frequency selective time varying fading.

Assuming the spatial correlations are identical for all resolvable physical multipaths, and static over time, the time and delay indices can be dropped. For arbitrary time and delay, the spatial correlation matrix $\mathbf{R}_{\mathrm{H}} \in \mathbb{C}^{N_{\mathrm{Rx}}N_{\mathrm{Tx}} \times N_{\mathrm{Rx}}N_{\mathrm{Tx}}}$ is defined by

$$\mathbf{R}_{\mathrm{H}} \triangleq \mathrm{E}\{\mathrm{vec}(\mathbf{H}_{\mathrm{t}})\mathrm{vec}(\mathbf{H}_{\mathrm{t}})^{\mathrm{H}}\}, \tag{3.17}$$

where $\mathrm{vec}(\mathbf{H}_{\mathrm{t}}) = [h_{1,1}, h_{2,1}, \cdots, h_{N_{\mathrm{Rx}},1}, h_{1,2}, \cdots, h_{N_{\mathrm{Rx}},2}, \cdots, h_{N_{\mathrm{Rx}},NTx}]^{\mathrm{T}}$ and $\mathbf{H}_{\mathrm{t}}$ is defined in (2.14). The operators $(\cdot)^{\mathrm{T}}$ and $(\cdot)^{\mathrm{H}}$ are the matrix transpose and Hermitian transpose, respectively. The correlation matrix is symmetric and real valued on its diagonal.

If the correlation matrix is known, a spatially correlated channel matrix $\mathbf{H}_{\mathrm{corr}}$ can be generated from the i.i.d. channel matrix in a rather straight forward way.

$$\mathbf{H}_{\mathrm{corr}} = \mathrm{unvec}(\mathbf{R}_{\mathrm{H}}^{1/2}\mathrm{vec}(\mathbf{H}_{\mathrm{iid}})) \tag{3.18}$$

where $\mathbf{R}_{\mathrm{H}}^{1/2}$ is the square root of $\mathbf{R}_{\mathrm{H}}$, $\mathrm{unvec}(\cdot)$ is the inverse operation of vec. $\mathbf{R}_{\mathrm{H}}^{1/2}$ has to be computed by solving the equation

$$\mathbf{R}_{\mathrm{H}}^{1/2}(\mathbf{R}_{\mathrm{H}}^{1/2})^{\mathrm{H}} = \mathbf{R}_{\mathrm{H}}. \tag{3.19}$$

In general $\mathbf{R}_{\mathrm{H}}$ is positive definite, thus, $\mathbf{R}_{\mathrm{H}}^{1/2}$ can be computed by its Cholesky decomposition [78].

One of the drawbacks of the full correlation matrix is its big size. It needs $(N_{\mathrm{Rx}}N_{\mathrm{Tx}})^2$ parameters to be fully specified. Furthermore, a direct interpretation of $\mathbf{R}_{\mathrm{H}}$ with respect to the physical propagation of radio channel is difficult.

A simplification of the full correlation matrix approach is proposed in [50], where all antenna elements in both antenna arrays are assumed to have the same polarization and radiation pattern. In addition, all elements on the transmitter and receiver side obtain the same power azimuth spectrum (PAS) from each element on the opposite side. The full channel spatial correlation matrix $\mathbf{R}_{\mathrm{H}}$ can be written as

$$\mathbf{R}_{\mathrm{H}} = \frac{1}{\mathrm{tr}\{\mathbf{R}_{\mathrm{Rx}}\}}\mathbf{R}_{\mathrm{Rx}} \otimes \mathbf{R}_{\mathrm{Tx}}^{\mathrm{T}}, \tag{3.20}$$

where $\otimes$ denotes the Kronecker product and $\mathrm{tr}(\cdot)$ is the matrix trace. The one side Tx and Rx correlation matrices are defined as

$$\mathbf{R}_{\mathrm{Rx}} = \mathrm{E}\{\mathbf{H}_{\mathrm{t}}\mathbf{H}_{\mathrm{t}}^{\mathrm{H}}\} \quad (3.21)$$

$$\mathbf{R}_{\mathrm{Tx}} = \mathrm{E}\{\mathbf{H}_{\mathrm{t}}^{\mathrm{H}}\mathbf{H}_{\mathrm{t}}\}, \quad (3.22)$$

respectively. And the spatially correlated channel matrix can be generated using

$$\mathbf{H}_{\mathrm{kron}} = \frac{1}{\sqrt{\mathrm{tr}\{\mathbf{R}_{\mathrm{Rx}}\}}}\mathbf{R}_{\mathrm{Rx}}^{1/2}\mathbf{H}_{\mathrm{iid}}(\mathbf{R}_{\mathrm{Tx}}^{1/2})^{\mathrm{T}}, \quad (3.23)$$

where $\mathbf{R}_{\mathrm{Rx}}^{1/2}$ and $\mathbf{R}_{\mathrm{Tx}}^{1/2}$ can be calculated using Denman-Beavers square root iteration [79]. The number of parameters required to fully characterize the MIMO channel by the Kronecker model is $N_{\mathrm{Tx}}^2 + N_{\mathrm{Rx}}^2$, which is significantly smaller than by the full correlation model.

Generally, the modeling parameters $\mathbf{R}_{\mathrm{Rx}}$ and $\mathbf{R}_{\mathrm{Tx}}$ should be estimated using measurement data. Moreover, a further simplification of the Kronecker model is proposed in [86], where only one coefficient is required to represent the Tx or Rx correlation matrix. The single coefficient Kronecker model is idealistic, however very easy to apply, thus, quite often used in scientific researches.

3.1.3 Weichselberger model

By assuming the separability of both link ends, the Kronecker model decomposes the full correlation matrix into Tx and Rx correlation matrices, and thus offers simplicity for theoretical analysis. However, the ignored joint correlation properties at the transmitter and receiver lead to an underestimation of channel capacity with Kronecker model [68].

Consider the case that both link ends are not independent, the one-sided correlation matrices have to be parameterized by the statistical properties of the other link end

$$\mathbf{R}_{\mathrm{Rx},\mathbf{Q}_{\mathrm{Tx}}} = \mathrm{E}\{\mathbf{H}_{\mathrm{t}}\mathbf{Q}_{\mathrm{Tx}}\mathbf{H}_{\mathrm{t}}^{\mathrm{H}}\} \quad (3.24)$$

$$\mathbf{R}_{\mathrm{Tx},\mathbf{Q}_{\mathrm{Rx}}} = \mathrm{E}\{\mathbf{H}_{\mathrm{t}}^{\mathrm{H}}\mathbf{Q}_{\mathrm{Rx}}\mathbf{H}_{\mathrm{t}}\} \quad (3.25)$$

where $\mathbf{Q}_{\mathrm{Tx}}$ and $\mathbf{Q}_{\mathrm{Rx}}$ are the spatial signal covariance matrices of the Tx and Rx sides, respectively [87]. The Kronecker model is a special case where $\mathbf{Q}_{\mathrm{Tx}}$ and $\mathbf{Q}_{\mathrm{Rx}}$ are identity matrices.

It is easy to prove that both $\mathbf{R}_{\mathrm{Rx},\mathbf{Q}_{\mathrm{Tx}}}$ and$\mathbf{R}_{\mathrm{Tx},\mathbf{Q}_{\mathrm{Rx}}}$ are normal matrices. They can be factorized using the eigenvalue decomposition as

$$\mathbf{R}_{\mathrm{Rx},\mathbf{Q}_{\mathrm{Tx}}} = \mathbf{U}_{\mathrm{Rx}}\mathbf{\Lambda}_{\mathrm{Rx},\mathbf{Q}_{\mathrm{Tx}}}\mathbf{U}_{\mathrm{Rx}}^{\mathrm{H}} \quad (3.26)$$

$$\mathbf{R}_{\mathrm{Tx},\mathbf{Q}_{\mathrm{Rx}}} = \mathbf{U}_{\mathrm{Tx}}\mathbf{\Lambda}_{\mathrm{Tx},\mathbf{Q}_{\mathrm{Rx}}}\mathbf{U}_{\mathrm{Tx}}^{\mathrm{H}}, \quad (3.27)$$

where $\mathbf{\Lambda}$ are real-valued diagonal matrices with nonnegative entries. The eigenbases $\mathbf{U}_{\mathrm{Rx}}$ and $\mathbf{U}_{\mathrm{Tx}}$ do not have dependencies on the correlation of the other link end.

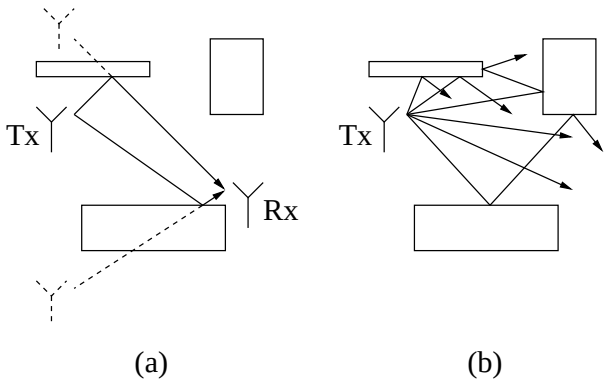

Figure 3.2: Deterministic channel models: (a) Ray-tracing; (b)Ray-launching.

The channel matrix of Weichselberger model can be written as

$$\mathbf{H}_{\text{weich}} = \mathbf{U}_{\text{Rx}} \left(\widetilde{\mathbf{\Omega}} \odot \mathbf{H}_{\text{iid}} \right) \mathbf{U}_{\text{Tx}}^{\text{T}}, \tag{3.28}$$

where $\tilde{\mathbf{\Omega}}$ is the element-wise square root of the power coupling matrix $\mathbf{\Omega}$, $\odot$ is the element-wise matrix product.

The modeling parameters $\mathbf{R}_{\text{Rx},\mathbf{Q}_{\text{Tx}}}$, $\mathbf{R}_{\text{Tx},\mathbf{Q}_{\text{Rx}}}$ and $\mathbf{\Omega}$ must be extracted from measurement data, in order to recreate a certain channel condition. Detailed information is given in [87]. By considering the joint correlation on both link ends, the average mutual information of the channels generated by the Weichselberger model matches the measurements quite well, while the Kronecker model tends to underestimate the channel capacity [67]. However, since the model parameters can only be estimated from measurement data, the Weichselberger model is not applicable for a given environment without a measurement campaign.

3.2 Deterministic models

Unlike the analytical models, the starting point of geometry-based models is the physical wave propagation. According to the modeling methodology, geometry-based models can be categorized into deterministic models and stochastic models.

Deterministic models, such as ray-tracing and ray launching, characterize the physical propagation parameters in a completely deterministic manner by following or launching deflected rays from transmitters to receivers [89] [54]. In deterministic models, electromagnetic characteristics of radio links are explicitly calculated by means of a detailed description of the propagation environment. Deterministic models capture the nature of radio wave propagation, thus are intuitive and potentially accurate. However, they are site specific, i.e., geometric information about the propagation environment must be known.

In deterministic models, all possible paths from the Tx to the Rx are determined by considering propagation phenomena like reflections at walls and diffractions at

building edges. Usually, the propagation environment is described by polyhedrons. A visibility tree is build to capture the radio propagation paths. The visibility tree consists of nodes and branches, representing objects (walls, wedges, Rx, etc.) and LoS connections between objects, respectively. The layered structure of the visibility tree represents the depth of interactions.

For ray-tracing, the images of Tx relative to the reflecting planes are computed, as depicted in Figure 3.2 (a). Each reflected or diffracted ray from the Tx to the Rx is exactly determined. This calculation leads to a very high accuracy, because all the relevant objects are always considered for the selection of interactions. However, as the number of interactions increases, the computational complexity grows exponentially.

With ray-launching, the rays are launched from the transmitter homogeneously with a discrete angle increment [89]. After each interaction, the reflected or diffracted rays are computed and traced further as illustrated in Figure 3.2 (b). The tracing can be terminated, when the power of a ray drops under a predetermined threshold. The disadvantage is that the constant increment between two rays leads to the problem that it is hard to determine whether a wedge is hit or not.

Despite the high accuracy, the computational burden makes ray-tracing incapable of handling large wireless communication scenarios [85]. Thus, it is mostly used for indoor or microcell environment. The ray-launching method has many advantages in predicting field strength for a large area [61]. In urban scenarios, a cube oriented 3D ray launching algorithm (CORLA) proposed in [58] offers both fast and accurate field strength prediction. As an enhancement of CORLA, the ray-launching tool parallel implemented ray optical prediction algorithm (PIROPA) benefits from parallel computing peripherals, and thus provides an even faster solution [74].

However, since CORLA, PIROPA and other ray-tracing/launching algorithms are totally deterministic, they are generally used to predict field strength but not to generate channel matrices.

3.3 Geometry-based stochastic channel models

During radio wave propagation, a transmitted signal can be reflected or diffracted by various scatterers. In geometry-based stochastic channel model (GSCM), with geometrical description of the propagation environment (e.g. urban, suburban, etc.), locations of the scatterers are chosen randomly. After that, statistical information about the radio wave is generated and superimposed to create channel matrices. Moreover, for the purpose of creating an easy-to-use solution to conduct simulations, a few standardized GSCMs have been proposed.

3.3.1 Double directional channel model

To generate the statistical information, the influence of various elements on the radio channel should be studied separately. Consider the Rx side, the Rx antennas coher-

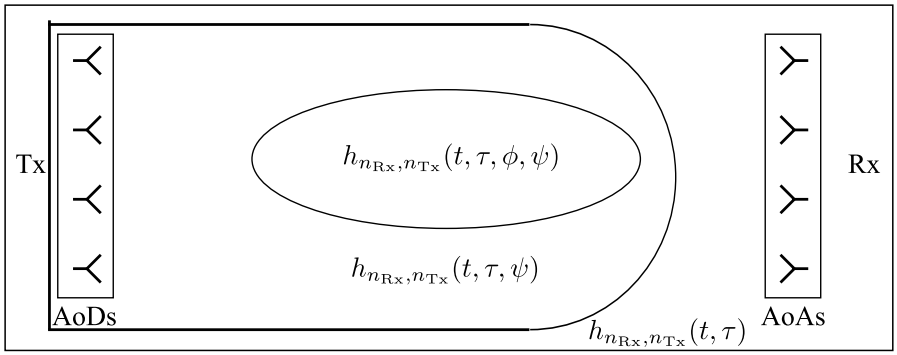

Figure 3.3: The relationship among the radio channel, the single directional channel and the double directional channel.

ently collect the components from all directions, and weight them with the directional antenna gain

$$h_{n_{\mathrm{Rx}},n_{\mathrm{Tx}}}(t,\tau) = \int_{\psi} \sqrt{G_{n_{\mathrm{Rx}}}(\psi)} h_{n_{\mathrm{Rx}},n_{\mathrm{Tx}}}(t,\tau,\psi)\mathrm{d}\psi, \tag{3.29}$$

where the single directional channel impulse response (CIR) $h_{n_{\mathrm{Rx}},n_{\mathrm{Tx}}}(t,\tau,\psi)$ is parameterized by the angle of arrival (AoA). The directional Rx antenna gain $G_{n_{\mathrm{Rx}}}$ depends on the antenna geometry and orientation.

Moreover, the Tx antennas distribute the signal energy into the desired angle of departure (AoD), the single directional CIR is the integration over all angles of departure AoDs

$$h_{n_{\mathrm{Rx}},n_{\mathrm{Tx}}}(t,\tau,\psi) = \int_{\phi} \sqrt{G_{n_{\mathrm{Tx}}}(\phi)} h_{n_{\mathrm{Rx}},n_{\mathrm{Tx}}}(t,\tau,\phi,\psi)\mathrm{d}\phi, \tag{3.30}$$

where $G_{n_{\mathrm{Tx}}}$ is the Tx antenna gain.

To summarize, the CIR is a function of the double directional CIR:

$$h_{n_{\mathrm{Rx}},n_{\mathrm{Tx}}}(t,\tau) = \int_{\phi}\int_{\psi} \sqrt{G_{n_{\mathrm{Tx}}}(\phi)}\sqrt{G_{n_{\mathrm{Rx}}}(\psi)} h_{n_{\mathrm{Rx}},n_{\mathrm{Tx}}}(t,\tau,\phi,\psi)\mathrm{d}\phi\mathrm{d}\psi. \tag{3.31}$$

The relationship of the CIR, the single directional CIR and the double directional CIR is shown in Figure 3.3. Clearly, the double directional channel model divides the radio channel into three parts: Tx antennas, Rx antennas and the double directional channel in between. In [80], the double directional channel model is validated with measurement data, laying the foundation of standardized GSCMs.

3.3.2 Multi-path component clusterization

In principle, the double directional channel model is an integral of multi-path components (MPCs), which has a distinct set of propagation parameters, such as AoD, AoA and delay. However, measurements show that these MPCs are often observed in clusters, where a cluster is a group of MPCs with similar propagation parameters as

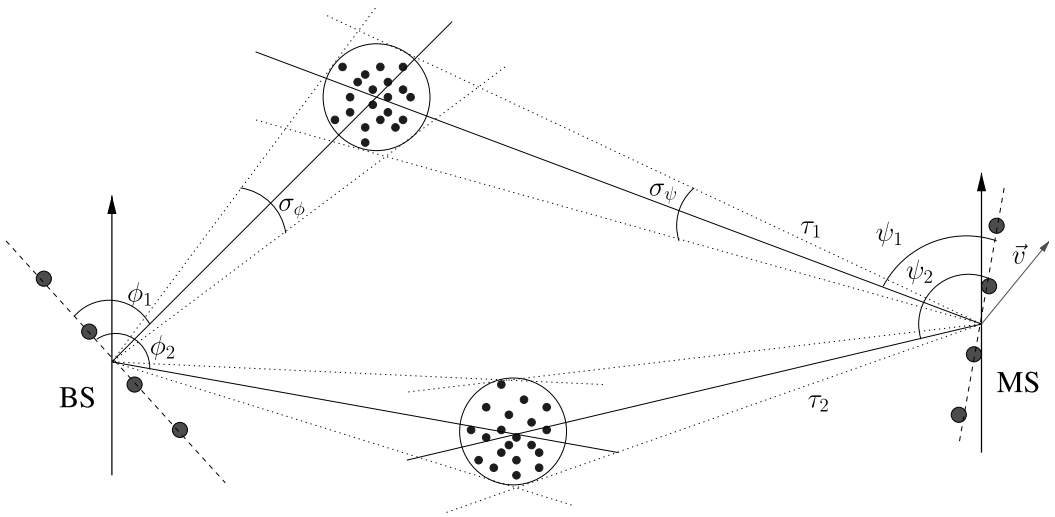

Figure 3.4: Clusterized multi-path MIMO channel model

shown in Figure 3.4 [71]. Ignoring the clustering effects results in overestimation of the channel capacity [52].

To engage computer-based simulation, the double directional channel model must be discretized. Therefore, the CIR of a cluster can be represented by the summation of a discrete number of MPCs.

The MIMO CIR can be written as

$$h_{n_{\mathrm{Rx}},n_{\mathrm{Tx}}}(t,\tau) = \sum_{n_{\mathrm{c}}=1}^{N_{\mathrm{c}}} \sum_{n_{\mathrm{M}}=1}^{N_{\mathrm{M}}} \sqrt{G_{n_{\mathrm{Tx}}}(\phi_{n_{\mathrm{c}},n_{\mathrm{M}}})} \sqrt{G_{n_{\mathrm{Rx}}}(\psi_{n_{\mathrm{c}},n_{\mathrm{M}}})} \cdot h_{n_{\mathrm{Rx}},n_{\mathrm{Tx}},n_{\mathrm{c}},n_{\mathrm{M}}}(t,\tau_{n_{\mathrm{c}},n_{\mathrm{M}}},\phi_{n_{\mathrm{c}},n_{\mathrm{M}}},\psi_{n_{\mathrm{c}},n_{\mathrm{M}}}) \tag{3.32}$$

where n_{c} and n_{M} are the index of cluster and index of MPC within a cluster, respectively. And N_{c} and N_{M} are the number of clusters and number of MPCs within a cluster, respectively.

Due to the similarity of the AoDs, AoAs within a cluster, they can be modeled as the cluster parameters with a small offset value [26]:

$$\phi_{n_{\mathrm{c}},n_{\mathrm{M}}} = \phi_{n_{\mathrm{c}}} + \epsilon_{\mathrm{AoD},n_{\mathrm{M}}} \tag{3.33}$$

$$\psi_{n_{\mathrm{c}},n_{\mathrm{M}}} = \psi_{n_{\mathrm{c}}} + \epsilon_{\mathrm{AoA},n_{\mathrm{M}}}, \tag{3.34}$$

where $\epsilon_{\mathrm{AoD},n_{\mathrm{M}}}$ and $\epsilon_{\mathrm{AoD},n_{\mathrm{M}}}$ are the offset values of AoD and AoA, respectively.

3.3.3 Standardized models

In the double directional channel model, the antenna geometry can be designed to produce desirable antenna patterns. The angularly resolved double directional CIRs can be generated, if their statistical properties are known. Following this concept,

standardized simulation models, such as 3GPP spatial channel model (SCM) [4], 3GPP spatial channel model extension (SCME) [15] and wireless world initiative new radio (WINNER) model [44], have been developed. Standardized models enable their users to generate channel matrices without performing measurement campaigns.

To develop standardized models, the standardization entities first have to conduct a large amount of channel measurements. The measured data are then analyzed and the statistical parameters are extracted. Supposedly, these models are able to recreate wireless channels with the same statistical behavior.

To use a standardized model, people have to choose a scenario (Urban, suburban, rural area, etc.) and set up the network layout as well as antenna parameters. With these settings given, the model first generates large scale parameters (LSPs), e.g., AoD spread, AoA spread and delay spread. Basically, the LSPs specify statistical properties of the small scale parameters including AoD, AoA, delay, etc. With the specified statistical properties, small scale parameters can be randomly generated and the channel coefficients can be calculated accordingly.

The generation of channel coefficients follows a generic model. Taking the scenario described in Figure 3.4 as an example, where both the Tx and Rx antenna arrays are uniform linear arrays (ULAs). Assuming that in each cluster, the power is uniformly distributed for every MPC, the CIR can be written as

$$\begin{aligned} h_{n_{\mathrm{Rx}},n_{\mathrm{Tx}}}(t,\tau) = \sum_{n_{\mathrm{c}}=1}^{N_{\mathrm{c}}} \sqrt{U_{n_{\mathrm{c}},n_{\mathrm{M}}}} \sum_{n_{\mathrm{M}}=1}^{N_{\mathrm{M}}} \sqrt{G_{n_{\mathrm{Tx}}}(\phi_{n_{\mathrm{c}},n_{\mathrm{M}}})} \sqrt{G_{n_{\mathrm{Rx}}}(\psi_{n_{\mathrm{c}},n_{\mathrm{M}}})} \\ \cdot \exp\left(\jmath \left(\frac{2\pi}{\lambda} \mathbf{k}_{\mathrm{Tx},n_{\mathrm{c}},n_{\mathrm{M}}}^{\mathrm{T}} \mathbf{d}_{\mathrm{Tx},n_{\mathrm{Tx}}} \right) + \Phi_{n_{\mathrm{c}},n_{\mathrm{M}}} \right) \\ \cdot \exp\left(\jmath \frac{2\pi}{\lambda} \mathbf{k}_{\mathrm{Rx},n_{\mathrm{c}},n_{\mathrm{M}}}^{\mathrm{T}} \mathbf{d}_{\mathrm{Rx},n_{\mathrm{Rx}}} \right) \\ \cdot \exp\left(\jmath \frac{2\pi}{\lambda} v_{n_{\mathrm{c}},n_{\mathrm{M}}} t \right) \delta(\tau - \tau_{n_{\mathrm{c}},n_{\mathrm{M}}}), \end{aligned} \tag{3.35}$$

where $U_{n_{\mathrm{c}},N_{\mathrm{M}}}$ is the MPC power. It is common to assume the cluster power is uniformly distributed in each MPC:

$$U_{n_{\mathrm{c}},n_{\mathrm{M}}} = \frac{U_{n_{\mathrm{c}}}}{N_{\mathrm{M}}}. \tag{3.36}$$

The wavelength of the carrier wave is denoted by λ. $\Phi_{n_{\mathrm{c}},n_{\mathrm{M}}}$ is a random initial phase and $\tau_{n_{\mathrm{c}},n_{\mathrm{M}}}$ is the path delay. The directional vectors are defined as [92]

$$\mathbf{k}_{\mathrm{Tx},n_{\mathrm{c}},n_{\mathrm{M}}} = \begin{bmatrix} \cos\phi_{n_{\mathrm{c}},n_{\mathrm{M}}} \\ \sin\phi_{n_{\mathrm{c}},n_{\mathrm{M}}} \end{bmatrix}, \quad \mathbf{k}_{\mathrm{Rx},n_{\mathrm{c}},n_{\mathrm{M}}} = \begin{bmatrix} \cos\psi_{n_{\mathrm{c}},n_{\mathrm{M}}} \\ \sin\psi_{n_{\mathrm{c}},n_{\mathrm{M}}} \end{bmatrix}, \tag{3.37}$$

where $\phi_{n_{\mathrm{c}},n_{\mathrm{M}}}$ and $\psi_{n_{\mathrm{c}},n_{\mathrm{M}}}$ are generated with a cluster AoD $\phi_{n_{\mathrm{c}}}$ and AoA $\psi_{n_{\mathrm{c}}}$ plus path specific offset angles. Furthermore, the AoDs and AoAs are randomly coupled. The position vectors are defined as

$$\mathbf{d}_{\mathrm{Tx},n_{\mathrm{Tx}}} = \begin{bmatrix} x_{\mathrm{Tx},n_{\mathrm{Tx}}} \\ y_{\mathrm{Tx},n_{\mathrm{Tx}}} \end{bmatrix}, \quad \mathbf{d}_{\mathrm{Rx},n_{\mathrm{Rx}}} = \begin{bmatrix} x_{\mathrm{Rx},n_{\mathrm{Rx}}} \\ y_{\mathrm{Rx},n_{\mathrm{Rx}}} \end{bmatrix}, \tag{3.38}$$

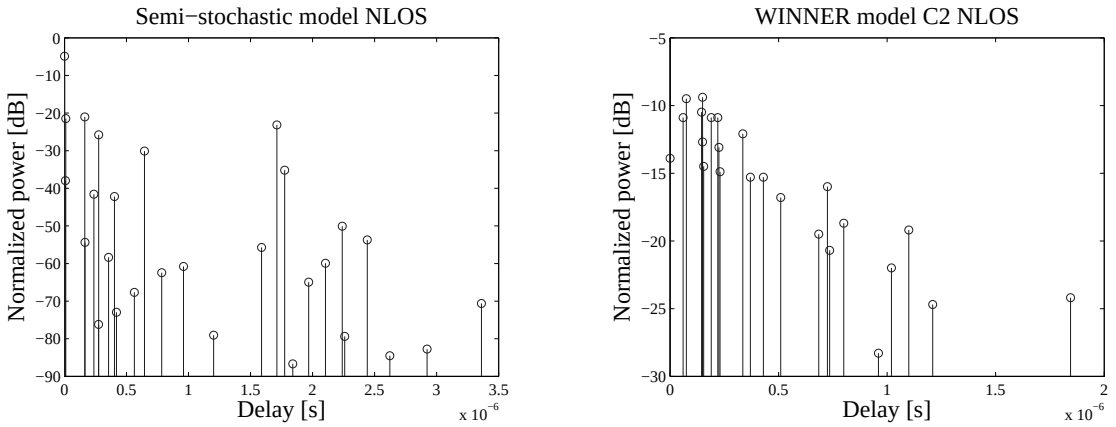

Figure 3.5: Power-delay profiles for a NLoS environment in (a) Semi-stochastic channel model (b) WINNER model C2 scenario (typical urban macrocell)

where $x_{\mathrm{Tx},n_{\mathrm{Tx}}}, y_{\mathrm{Tx},n_{\mathrm{Tx}}}, x_{\mathrm{Rx},n_{\mathrm{Rx}}}, y_{\mathrm{Rx},n_{\mathrm{Rx}}}$ are X and Y coordinates of the n_{Tx}th Tx antenna element and n_{Rx}th Rx antenna element, respectively. And the Doppler frequency component is defined as

$$v_{n_{\mathrm{c}},n_{\mathrm{M}}} = v\cos(\psi_{n_{\mathrm{c}},n_{\mathrm{M}}} - \vartheta) \tag{3.39}$$

where v and ϑ are speed and angle of the movement of the user, respectively.

There are some further extensions of this generic model including LoS support, polarized antenna, elevation angles, etc.

Among these three standardized models, the WINNER model provides the widest range of carrier frequency and bandwidth, the largest set of scenarios, and cross-correlation among LSPs. The WINNER model also allows a discrete time evolution of simulation parameters. Therefore, the WINNER model can be regarded as the leading MIMO channel model among existing standardized models [62].

3.4 Semi-stochastic channel model

In the WINNER model, the total number of different scenarios is 17, which is significantly larger than the 3 scenarios specified in SCM and SCME. However, there are still limitations for the standardized GSCM. Although some stochastic characteristics of the wireless channel are preserved, location specific geographical data can not be utilized to improve modeling accuracy. For example, the terrain of the city Budapest is flat on the side of Pest and uneven on the side of Buda. However, with GSCM, one can only choose "Urban" scenario to simulate both areas, and neglect the definite differences between the propagation environments.

In contrastt, geographical information can be effectively utilized in the deterministic models. However, the conventional deterministic models only focused on predicting

field strength, taking neither the frequency selectivity caused by multi-path propagation nor spatial diversity caused by multiple antennas into consideration. In [74], the ray-launching tool PIROPA provides not only field strength but also multi-path information, e.g., AoA, AoD and the delay of each path. With the multi-path information, a semi-stochastic channel model (SSCM) can be applied to generate the channel coefficients [101].

3.4.1 Combining deterministic model and stochastic model

The central idea of SSCM is to replace the randomly generated cluster parameters with explicitly calculated ones. Thus, the advantages of deterministic model and GSCM can be combined. Figure 3.5 shows two power delay profiles used in SSCM and WINNER, respectively. Be aware that unlike in WINNER model, in SSCM, the PDP is calculated with the environment data and thus location based. Therefore, even in a single scenario setup, two different locations close to each other can have significantly different PDPs due to radio wave propagation.

The basic assumption of SSCM is the equivalence of propagation paths in PIROPA and clusters in GSCM. With this assumption, ϕ_{n_c} and ψ_{n_c} can be obtained from the output of PIROPA, and $\phi_{n_\mathrm{c},n_\mathrm{M}}$ and $\psi_{n_\mathrm{c},n_\mathrm{M}}$ can be generated in the same way as in the standardized GSCMs.

The modeling procedure of SSCM can be summarized into two stages. The first stage is the deterministic stage, where PIROPA is performed on a certain city map. With the location of the BS and propagation environment given, PIROPA calculates propagation paths for every possible location of the MS on the map. The output information of this stage is totally deterministic. Therefore, for a given map, the deterministic stage is only needed to be performed once. The result can be saved into a file for the second stage. The second stage is the stochastic stage, where randomness is generated. In this stage, antenna patterns are applied according to antenna orientations; MPC parameters are generated following the same rules as described in the GSCMs and the Doppler frequency components are calculated for given moving speeds of the MSs. And finally (3.35) is used to calculate the CIR. In Table 3.1, the parameters generated in both stages are summarized.

3.4.2 Model validation

To validate the SSCM, MIMO data from a measurement campaign in Ilmenau is used for comparison.

Ilmenau measurements

The measurement campaign was done in July, 2008, in Ilmenau, a town in Thuringia, Germany. Ilmenau has a typical landscape of an European small to mid-sized town.

Deterministic stage	Stochastic stage
N_{c}	N_{M}
$U_{n_{\mathrm{c}}}$	$U_{n_{\mathrm{c}},n_{\mathrm{M}}}$
$\phi_{n_{\mathrm{c}}}$	$\phi_{n_{\mathrm{c}},n_{\mathrm{M}}}$
$\psi_{n_{\mathrm{c}}}$	$\psi_{n_{\mathrm{c}},n_{\mathrm{M}}}$
$\tau_{n_{\mathrm{c}}}$	$\tau_{n_{\mathrm{c}},n_{\mathrm{M}}}$
	$\mathbf{d}_{\mathrm{Tx},n_{\mathrm{Tx}}}, \mathbf{d}_{\mathrm{Rx},n_{\mathrm{Rx}}}$
	$v_{n_{\mathrm{c}},n_{\mathrm{M}}}$
	$\mathbf{\Phi}_{n_{\mathrm{c}},n_{\mathrm{M}}}$

Table 3.1: Parameters for deterministic stage and stochastic stage

The terrain is not totally flat but without steep slopes. Most of the buildings have similar heights. These facts make Ilmenau an ideal place to test for the urban macro cell reference scenario.

In the measurement campaign, three transmitters were placed on cranes and lifted to 25 meters above the ground to simulate BSs. Channel sounding equipments are carried by a car and traveled along 22 different trajectories, as shown in Figure 3.6. The campaign setup complies with 3GPP LTE standards. A pair of 40 MHz band at 2.53 GHz were measured [73]. On the BS side, a 8×1 polarized uniform linear patch array (PULPA) with beam width of 100° azimuth and 24° elevation is deployed. On the MS side, a 12×2 stacked polarimetric uniform circular patch array (SPUCPA) with omnidirectional azimuth pattern and 80° elevation beam width is adopted. The MS travels with a walking speed. The channel response is collected in frequency domain, as shown in Figure 3.7. Some of the measurement parameters are summarized in Table 3.2.

Inter-site distance	BS1-BS2 = 680m, BS2-BS3 = 580m, BS1-BS3 = 640m
Tx power	46 dBm
Center frequency	2.53 GHz
Bandwidth	2×40 MHz
CIR length	6.4 μs
CIR sampling	641 samples
Snapshot rate	>75 Hz
Positioning	Odometer and GPS

Table 3.2: Measurement setup of Ilmenau campaign

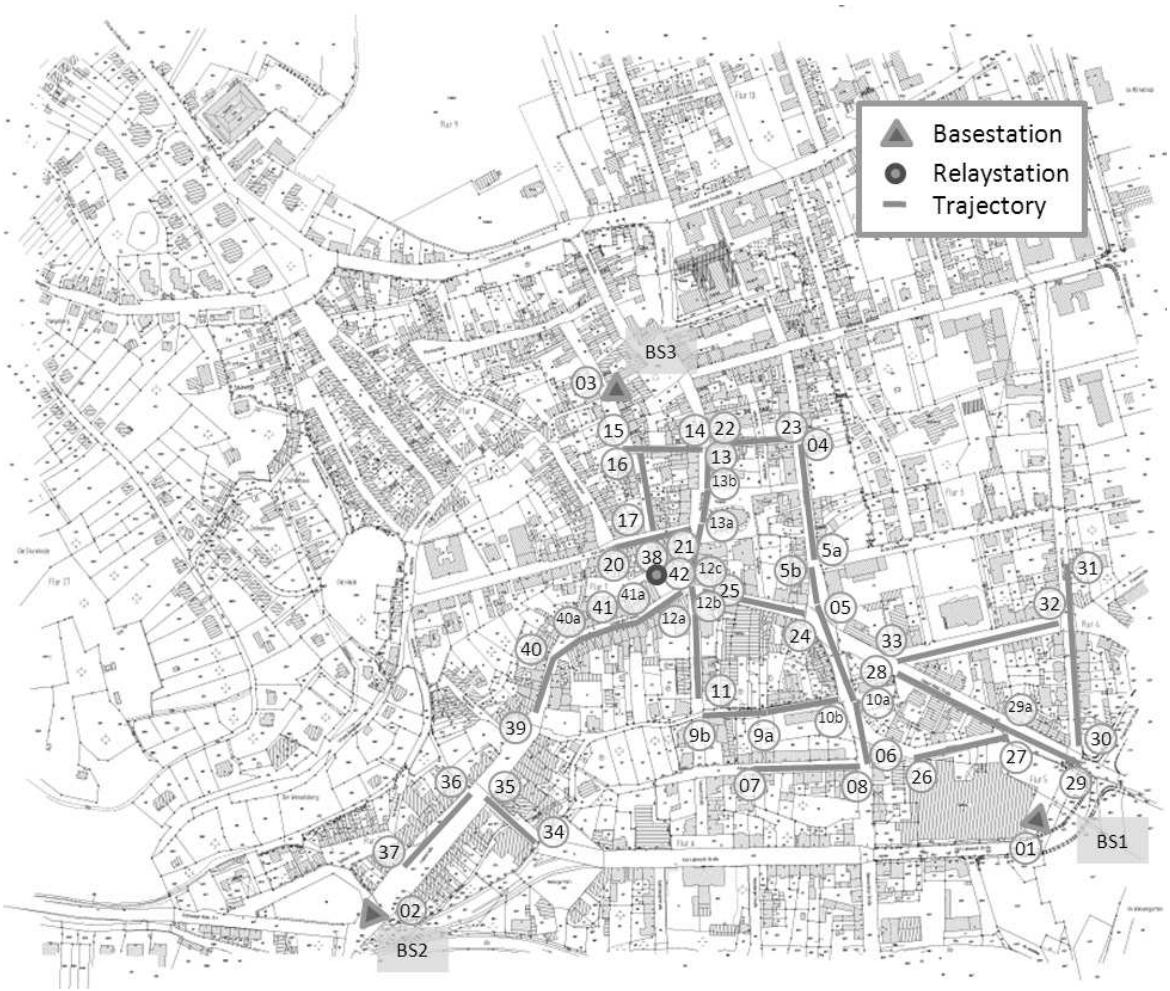

Figure 3.6: Overview of Ilmenau measurement campaign

Metric

For a wireless communication channel, the most important metric is the channel capacity. For simplicity, consider the frequency domain model in (2.17). For a channel realization $\mathbf{H}_\mathrm{f}$, the mutual information is given by

$$I = \log_2 \det \left(\mathbf{I}_{N_\mathrm{Rx}} + \mathbf{H}_\mathrm{f} \mathbf{Q} \mathbf{H}_\mathrm{f}^\mathrm{H} \right), \tag{3.40}$$

where $\mathbf{Q}$ is the frequency domain spatial signal covariance matrix, defined as

$$\mathbf{Q} = \mathrm{E} \left\{ (\mathbf{x}_\mathrm{f} - \mathrm{E}\{\mathbf{x}_\mathrm{f}\})(\mathbf{x}_\mathrm{f} - \mathrm{E}\{\mathbf{x}_\mathrm{f}\})^\mathrm{H} \right\}. \tag{3.41}$$

For fading channel with perfect CSI available at both the Tx and Rx ends, the ergodic channel capacity can be written as [36]

$$C_\mathrm{perfect} = \mathrm{E} \left\{ \max_{\mathbf{Q}} \log_2 \det \left(\mathbf{I}_{N_\mathrm{Rx}} + \rho_\mathrm{Tx} \mathbf{H}_\mathrm{f} \mathbf{Q} \mathbf{H}_\mathrm{f}^\mathrm{H} \right) \right\}, \tag{3.42}$$

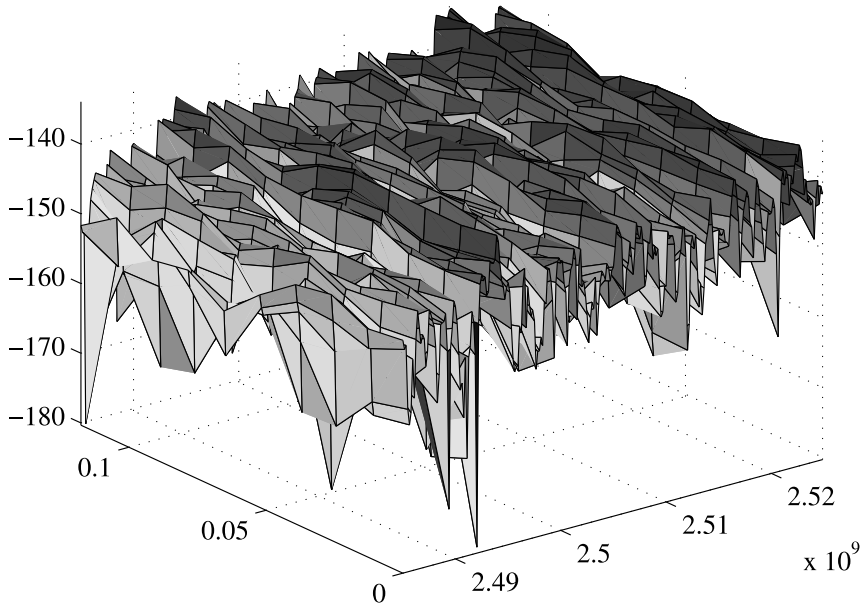

Figure 3.7: Measured CFR of path 9a-9b from Ilmenau data

where ρ_{Tx} is the transmit signal to noise ratio (SNR). In this case, the channel capacity can be achieved if the transmit power is optimized with water filling.

If CSI is not available, the optimal covariance matrix $\mathbf{Q}$ is given by [83]

$$\mathbf{Q} = \frac{1}{N_{\mathrm{Tx}}} \mathbf{I}_{N_{\mathrm{Tx}}} \tag{3.43}$$

and the ergodic capacity becomes

$$C_{\mathrm{no}} = \mathrm{E}\left\{ \log_2 \det\left(\mathbf{I}_{N_{\mathrm{Rx}}} + \frac{\rho_{\mathrm{Tx}}}{N_{\mathrm{Tx}}} \mathbf{H}_{\mathrm{f}} \mathbf{H}_{\mathrm{f}}^{\mathrm{H}} \right) \right\}. \tag{3.44}$$

Numerical results

In the numerical evaluation, C_{no} calculated for the SSCM and WINNER model is compared with the ergodic capacity obtained from measurements. For WINNER model, the same relative locations of the basestations and mobile stations are used. However, due to the limitation of GSCM, the location information of the buildings can not be given as input to improve the performance.

As shown in Figure 3.8, the ergodic capacity calculated by SSCM is very close to the measurements, whereas the WINNER model gives a more fluctuated result with much less accuracy. Therefore, the extra geographic information provided to the ray

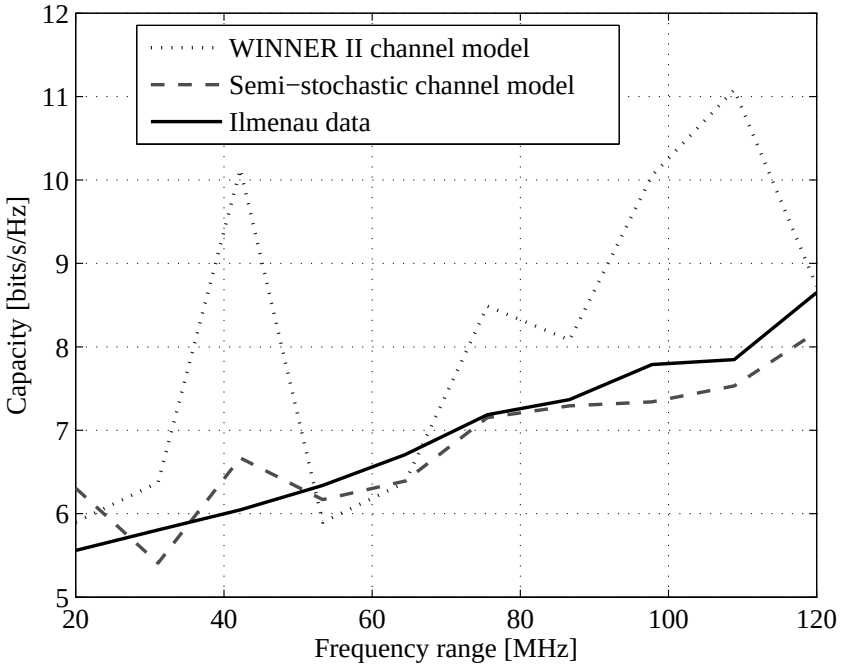

Figure 3.8: Ergodic channel capacity for path 9a-9b

launcher indeed improves the modeling accuracy. Moreover, since the ray launcher is only needed once, the SSCM can actually have a smaller computational complexity than WINNER model [19] for multiple simulations in the same environment.

3.4.3 Adaptation to OFDM systems

In OFDM systems, the signals are sampled with a sampling interval T_s. However, in the SSCM, the delay taps are not necessarily aligned with the sampling grids. Therefore, direct time domain sampling results in false output. This problem can be solved by using the frequency domain representation.

Consider the wide-band channel described by (2.2) and its frequency domain representation in (2.9), the effective time domain response can be written as

$$h(t, mT_\mathrm{s}) = \sum_{k=0}^{K-1} H(t,k) \exp\left\{\jmath 2\pi \frac{kmT_\mathrm{s}}{T}\right\} \tag{3.45}$$

$$= \sum_{k=0}^{K-1} \sum_{l=1}^{L} \xi_l(t) \exp\left\{-\jmath 2\pi \frac{k\tau_l}{T}\right\} \exp\left\{\jmath 2\pi \frac{km}{K}\right\} \tag{3.46}$$

$$= \sum_{l=1}^{L} \xi_l(t) \sum_{k=0}^{K-1} \exp\left\{\jmath 2\pi k \left(\frac{m}{K} - \frac{\tau_l}{T}\right)\right\}. \tag{3.47}$$

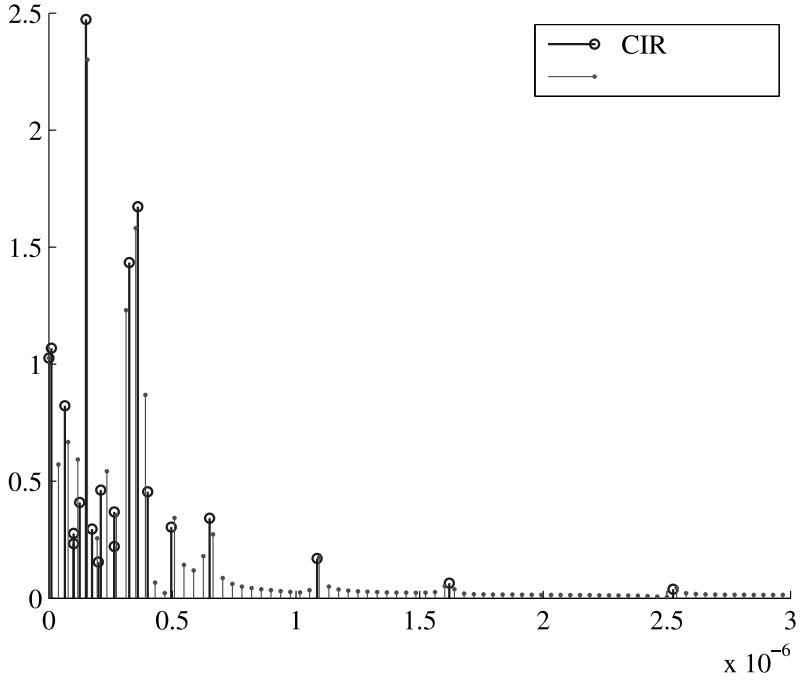

Figure 3.9: Equivalent baseband CIR for an OFDM system with 128 subcarriers

As a geometry sequence, the summation over k can be calculated as

$$\sum_{k=0}^{K-1} \exp\left\{\jmath 2\pi k \left(\frac{m}{K} - \frac{\tau_l}{T}\right)\right\} = \frac{1 - \exp\left\{\jmath 2\pi K \left(\frac{m}{K} - \frac{\tau_l}{T}\right)\right\}}{1 - \exp\left\{\jmath 2\pi \left(\frac{m}{K} - \frac{\tau_l}{T}\right)\right\}}. \tag{3.48}$$

From Euler's formula, it is easy to get

$$1 - \exp\{\jmath a\} = -2\jmath \exp\left\{\jmath \frac{a}{2}\right\} \sin\left(\frac{a}{2}\right). \tag{3.49}$$

Applying (3.49) to (3.47) yields the equivalent baseband CIR for OFDM systems as

$$h(t, mT_\mathrm{s}) = \sum_{l=1}^{L} \xi_l(t) \exp\left\{\jmath\pi(K-1)\left(\frac{m}{K} - \frac{\tau_l}{T}\right)\right\} \frac{\sin\left(\pi K \left(\frac{m}{K} - \frac{\tau_l}{T}\right)\right)}{\sin\left(\pi \left(\frac{m}{K} - \frac{\tau_l}{T}\right)\right)}. \tag{3.50}$$

An example of the CIR produced by SSCM and the equivalent CIR for OFDM systems is shown in Figure 3.9.

3.4.4 Obtaining geographical information

To use the SSCM, precise geographical data is a prerequisite, however usually unavailable. The open source database open street map (OSM) provides free information

about the accurate building shapes [1]. The coverage of OSM includes the majority of populated area in Europe. Figure 3.10 (a) shows a part of the city Munich. Since the purpose of OSM is map usage, there is only little of height information, which has to be obtained from other sources.

As a feature of most European cities, neighboring buildings generally have similar heights. Thus, a uniform height can be assigned to the buildings to achieve a good estimation. Figure 3.10 (b) is constructed from the OSM data with an uniform height information from estimation. Some previous works show that ray-tracing can still deliver good results with a 2.5D map with uniform height information [38].

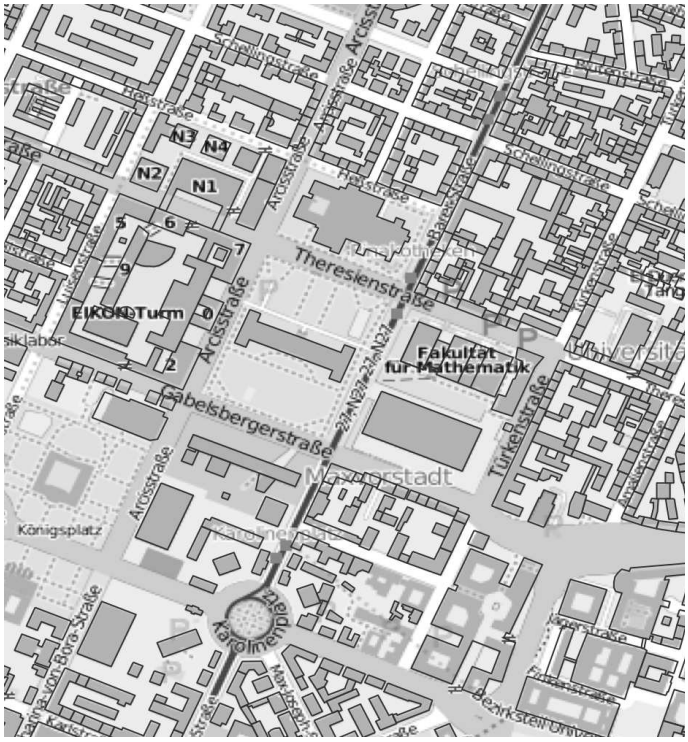

(a)

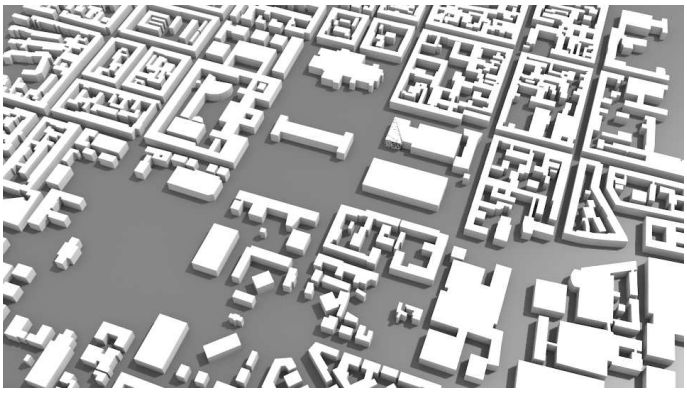

(b)

Figure 3.10: (a) Building information of a part of Munich. Building edges are marked with solid lines. (b) Reconstructed 2.5 D geographical data using uniform building height

4 Feedback Strategies for Link level Information

In cellular systems, to facilitate radio resource management, the downlink channel state information (CSI) is measured by the MS and it is send back to the BS via uplink transmission. The feedback operation must be done periodically, since the mobile radio channel is always changing. Therefore, to improve the uplink data throughput, the signaling overhead caused by this feedback information should be minimized. In LTE systems, a 4-bit channel quality indicator (CQI) is specified to carry the CSI [8].

The highly quantized CQI results in several problems. Firstly, in frequency selective channels, different subcarriers have a different frequency response. However, the LTE CQI feedback is not specified on subcarrier level, but on subband level. And each subband consists a number of subcarriers. Hence, the different CSI on different subcarriers must be properly mapped into one single CQI. The mapping from CSI to CQI is discussed in Section 4.1. Secondly, after the CQI is transmitted from the MS, there is always a delay, before it is used in the BS to determine the resource allocation. If this period is longer than the channel coherence time, the CQI used at the BS could be already outdated. As a result, the temporal variation of the channel should be compensated with channel prediction. The compensation of temporal variation is addressed in Section 4.3. Moreover, channel prediction schemes behave differently in systems with HARQ, which is explained in Section 4.4. In addition, the CQI has a strong relation to the resource allocation algorithm in multi-user systems. This issue is investigated in 4.5.

Parts of this chapter have been published in [64], [99], [102] and [100].

4.1 Information feedback in cellular networks

In LTE, depending on the periodicity of the CQI reporting modes, the feedback information is sent via the physical uplink control channel (PUCCH) or the physical uplink shared channel (PUSCH). And the down link data is transmitted via the PDSCH, where the modulation and coding schemes depend on the feedback information [5].

4.1.1 LTE resource structure and CQI basics

The LTE frame structure in physical downlink shared channel (PDSCH) is shown in Figure 4.1. As the smallest unit in the LTE transmission structure, the resource ele-

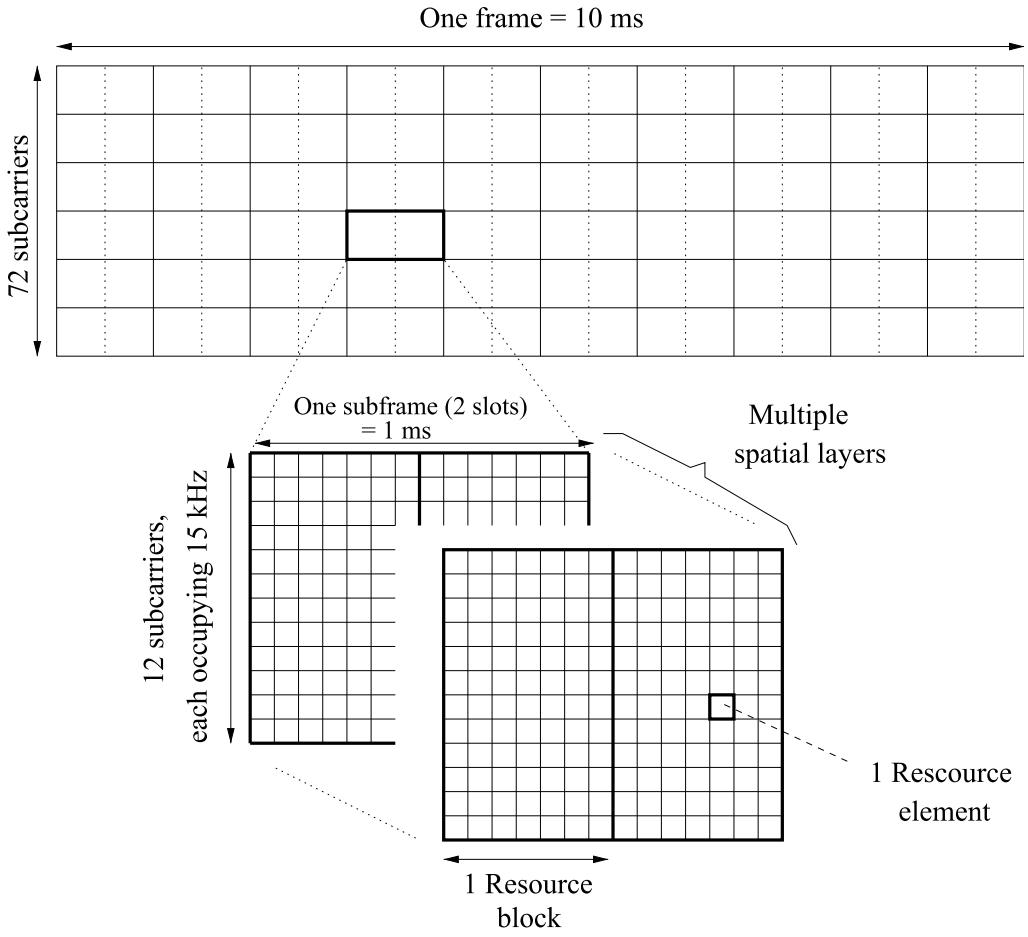

Figure 4.1: Resource structure of LTE

ment (RE) is defined as 1 subcarrier times 1 OFDMA symbol. A slot, which is made up by 7 OFDMA symbols with normal cyclic prefix or 6 OFDMA symbols with extended cyclic prefix, has a length of 0.5 ms in time domain. The basic unit for resource allocation is the physical resource block (PRB), which consists of 12 consecutive subcarriers in 1 slot [8]. In spatial multiplexing mode, a few spatial layers can be transmitted at the same time. A frame of a duration of 10 ms consists of 10 subframes, and each subframe consists of 2 slots.

As a feature of OFDMA, a different modulation and coding scheme (MCS) can be applied to different PRB. Moreover, the MCS is adaptive to channel conditions, where the base stations can choose either higher data rate or better error protection, according to the channel quality [6]. To facilitate adaptive modulation and coding (AMC), UEs must measure the channel quality and send the information to base stations. To reduce the signaling overhead, the channel quality information is compressed into a 4 bit CQI in LTE standards [8].

The CQI works as an index of the MCS. The correspondence between the CQI and the MCS is shown in Table 4.1. Smaller CQI values correspond to lower modulation orders

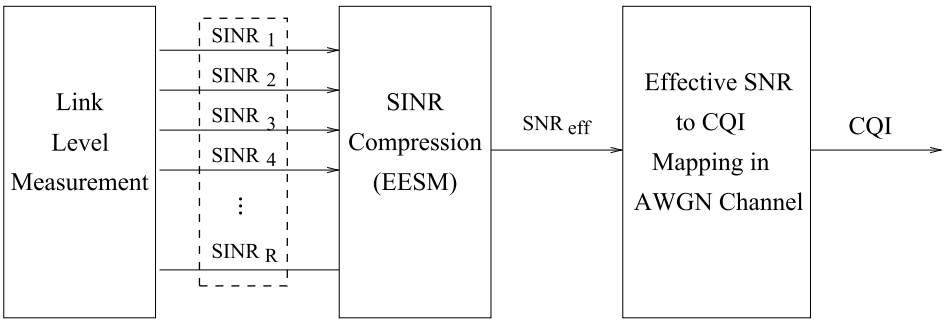

Figure 4.2: SINR to CQI mapping for SISO transmission

CQI index	Modulation	Code rate × 1024	Efficiency [bit/s/Hz]
0	out of range		
1	QPSK	78	0.1523
2	QPSK	120	0.2344
3	QPSK	193	0.3770
4	QPSK	308	0.6016
5	QPSK	449	0.8770
6	QPSK	602	1.1758
7	16QAM	378	1.4766
8	16QAM	490	1.9141
9	16QAM	616	2.4063
10	64QAM	466	2.7305
11	64QAM	567	3.3223
12	64QAM	666	3.9023
13	64QAM	772	4.5234
14	64QAM	873	5.1152
15	64QAM	948	5.5547

Table 4.1: The 4-bit CQI table in LTE [8]

and smaller code rates. Therefore, the data is better protected against distortion. And larger CQI values correspond to higher order modulation and higher code rates, such that higher data rate can be achieved. Accordingly, the CQI can be defined as

Definition 1. *The CQI is the highest index in Table 4.1, whose MCS leads to a block error rate (BLER) not higher than 0.1 in the current channel condition.*

Moreover, to further reduce the usage of uplink bandwidth, the feedback information is generated on subband level. A subband is defined as a group of consecutive PRBs. The CSI of all the PRBs within a subband is compressed into only one CQI message. Therefore, the CSI, namely, the SINR, of each PRB must be properly mapped into a single value. In fact, the SINR to CQI mapping consists of two steps, as illustrated in Figure 4.2. The measured SINRs are first compressed into a real valued effective SNR. The effective SNR is then mapped into an integer CQI.

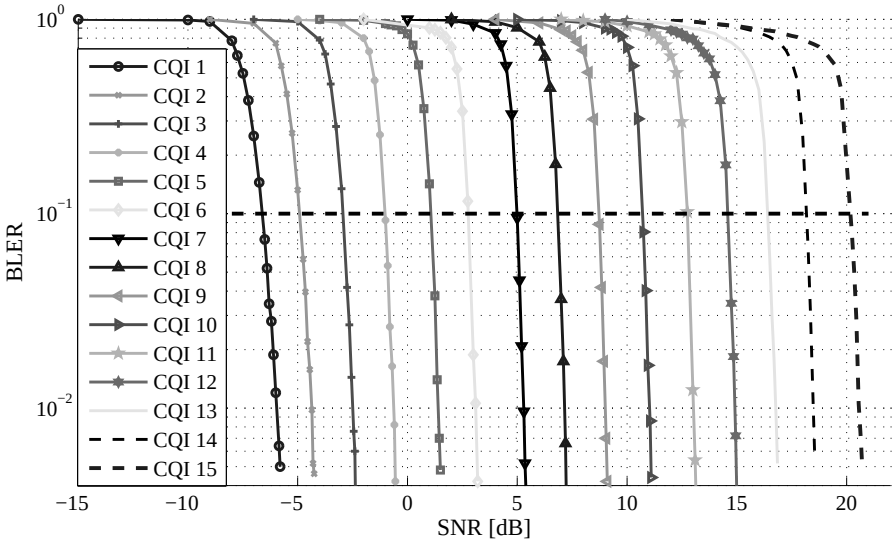

Figure 4.3: BLER for CQI 1-15 in AWGN channel

4.1.2 SINR to CQI mapping

To improve network capacity, the frequency reuse factor in LTE is 1. Therefore, strong co-channel interference (CCI) is to be expected. Consider a downlink system with S cells, where an arbitrary UE i is served by the cell s. The Tx power is uniformly distributed among subcarriers and the OFDMA signals are perfectly synchronized. The frequency domain SINR of user i on subcarrier k is given as

$$\gamma(t,k) = \frac{\frac{|H_{i,s}(t,k)|^2 G_s(t,k) U_s(t,k)}{L_{i,s}(t,k)}}{\sum\limits_{j \in \mathcal{S} \setminus s} \frac{|H_{i,j}(t,k)|^2 G_j(t,k) U_j(t,k)}{L_{i,j}(t,k)} + \sigma_w^2}, \tag{4.1}$$

where U is the Tx power, G is the antenna gain of the BS, L is the pathloss, H is the normalized CFR for fast fading process, $\mathcal{S}$ is the set of cells and σ_w^2 is the noise power.

Due to frequency selectivity, different PRBs generally have different SINRs. To find a proper value for the CQI, SINRs on different PRBs must first be mapped into an effective SNR. The BLER is the most popular criterion for the SINR to effective SNR mapping.

Since the CQI feedback is done on subband level, all the PRBs in the same subband would have the same MCS. With perfect channel knowledge, the CQI $Q(t,\kappa)$ is the index of MCS for an arbitrary PRB κ in subband b, as given in Table 4.1. The BLER of the transmission is jointly determined by the MCS and effective SNR of the wireless channel as $P_{\mathrm{e}}(Q(t,\kappa), \gamma_{\mathrm{e}}(t,b))$.

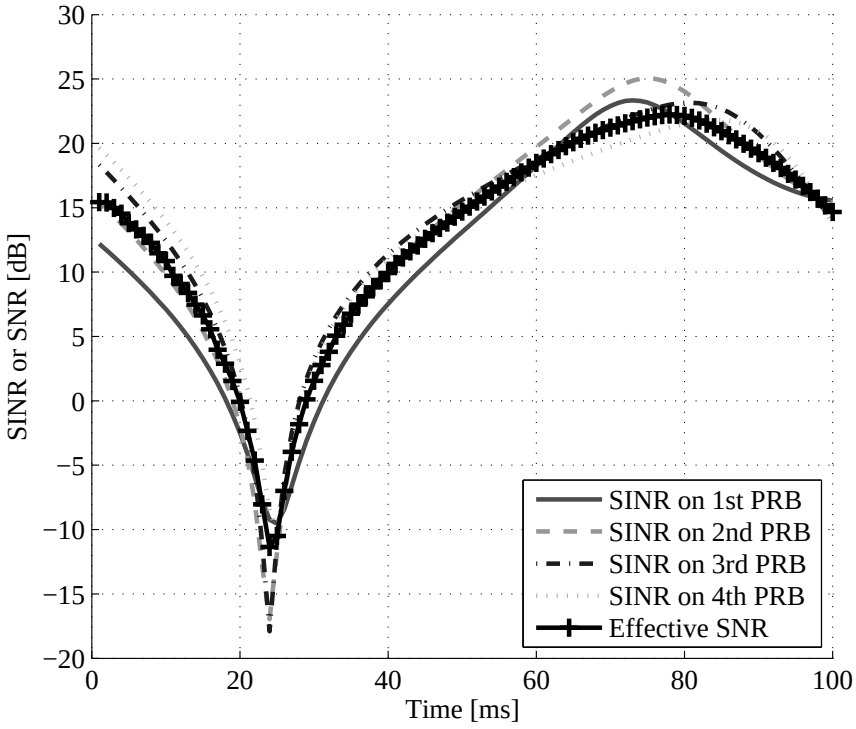

Figure 4.4: SINR to effective SNR mapping for 4 PRBs, using EESM

The BLER of transmission with different SINR in a frequency selective fading channel should match the BLER of transmission with the effective SNR in an AWGN channel. It can be written as:

$$P_{\mathrm{e}}(Q(t,\kappa),\gamma_{\mathrm{e}}(t,b)) = P_{\mathrm{e}}(Q(t,\kappa),\gamma(t,k),\kappa\in\mathcal{K}_i,k\in\mathcal{B}_i(b)), \tag{4.2}$$

where P_{e} is the BLER, γ_{e} is the effective SNR, $\mathcal{K}$ is the set of PRBs, and $\mathcal{B}_i(b)$ is the set of subcarriers in subband b. The BLER performance using the modulation and coding scheme specified in Table 4.1 in AWGN channel is shown in Figure 4.3.

One commonly used SINR to effective SNR mapping scheme is the exponential effective SINR mapping (EESM) [28]. Using EESM, the effective SNR can be written as

$$\gamma_{\mathrm{e}}(t,b) = -\beta\ln\left(\frac{1}{N_b}\sum_{k\in\mathcal{B}_i(b)}\exp\left\{-\frac{\gamma(t,k)}{\beta}\right\}\right), \tag{4.3}$$

where N_b is the number of subcarriers in set $\mathcal{B}_i(b)$, the calibration parameter β needs to be empirically fine-tuned as a function of MCS and packet length. The fine-tuning can be done by minimizing the SINR compression error with extensive simulations [63]. Following the 3GPP specification of transmission blocks [6] and implementation of the Turbo decoder described in [82], the optimal values of β are summarized in

CQI	0	1	2	3	4	5	6	7
β	n/a	4.40	4.07	4.22	3.87	4.57	4.68	5.85
CQI	8	9	10	11	12	13	14	15
β	3.77	3.97	3.71	3.06	3.20	3.04	2.41	1.88

Table 4.2: Optimal value for β in LTE

CQI	0	1	2	3	4	5	6	7
SNR[dB]	$-\infty$	-6.59	-4.94	-2.90	-1.04	1.08	2.78	5.02
CQI	8	9	10	11	12	13	14	15
SNR[dB]	6.89	8.70	10.74	12.78	14.64	16.42	18.20	20.19

Table 4.3: Minimum effective SNR for CQI feedback

Table 4.2. An example of SINR to effective SNR mapping using EESM is given in Figure 4.4.

According to Definition 1, the effective SNR to CQI mapping function can be easily derived by applying a horizontal line for $P_\mathrm{e} = 0.1$ in Figure 4.3. Each intersection point indicates the minimal SNR for the corresponding CQI, as shown in Table 4.3. Consequently, a step mapping function can be obtained, as illustrated in Figure 4.5.

4.1.3 Throughput and CQI feedback

The most important QoS metric in LTE is data throughput. Consider a single user case. Suppose perfect CSI is available and the MCS is always matched to the channel condition as described in Table 4.1. The probability of a successful transmission is

$$P_0(Q(t,\kappa),\gamma_\mathrm{e}(t,b)) = 1 - P_\mathrm{e}(Q(t,\kappa),\gamma_\mathrm{e}(t,b)). \tag{4.4}$$

Thus, the bandwidth efficiency of a certain PRB can be written as

$$E(t,\kappa) = \eta\left(Q(t,\kappa)\right) P_0(Q(t,\kappa),\gamma_\mathrm{e}(t,b)), \tag{4.5}$$

where η is the spectral efficiency as a function of the MCS, which can be found in Table 4.1. And the average throughput of this user is given by

$$F(t) = \sum_{\kappa\in\mathcal{K}} B \cdot E(t,\kappa), \tag{4.6}$$

where B is the bandwidth of a PRB.

The relationship of bandwidth efficiency and effective SNR is shown in Figure 4.6. Since the MCS is directly associated with CQI, a noisy CQI feedback leads to an reduced throughput.

The CQI feedback consists of the following components as noise:

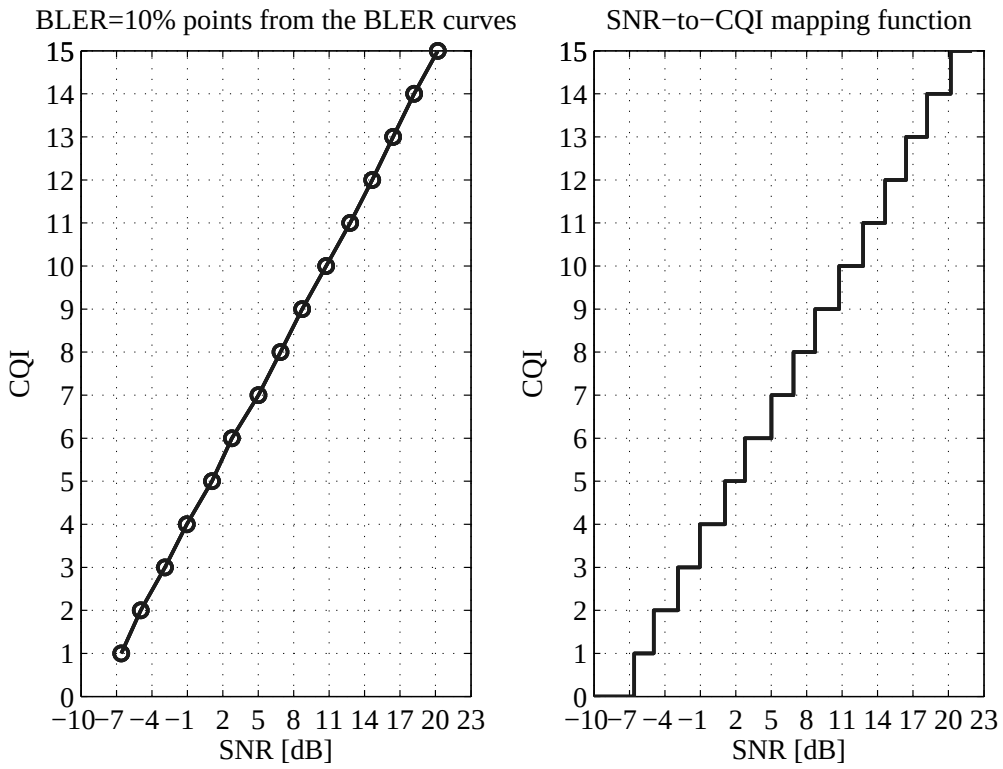

Figure 4.5: Effective SNR to CQI mapping function, extracted from the BLER curves

- *Estimation noise:* On UE side, due to imperfect SINR estimation, the estimated SINR is deviated from the true SINR [42].
- *Compression noise:* The SINR to effective SNR mapping, is a lossy compression.
- *Calibration noise:* In the SINR to effective SNR mapping, the parameter β is empirically calibrated. Different implementations of the turbo decoder could result in a calibration mismatch.
- *Quantization noise:* The real valued effective SNR is mapped to a 4-bit CQI index, with a lot of information loss.

In the presence of such noise components, the CSI available at the eNB side is far from perfect. However, the radio resource management in LTE systems must be performed using only this imperfect information. The result is that solutions depending on perfect CSI are either inapplicable or that performance is degraded severely in real systems.

Other than the aforementioned noises, CQI feedback also suffers from temporal variation caused by delay. Figure 4.7 shows the time sequence for CQI feedback in LTE systems, where the total feedback delay is composed of the measurement delay on the UE side, the propagation delay in the wireless channel and the processing delay on the eNB side. Due to the movement of UE, the mobile channel is always changing. The CQI used for the resource management can be already outdated. Thus, the temporal variation of CSI must be compensated.

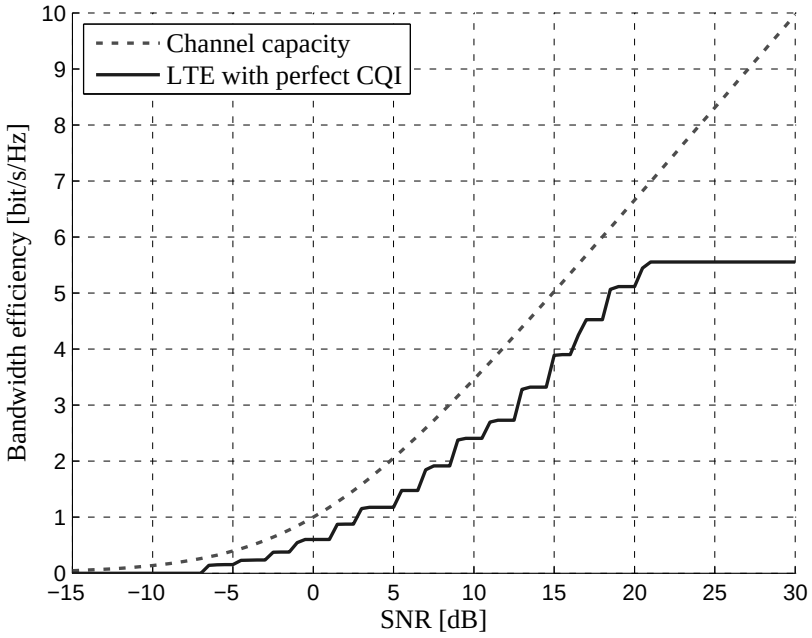

Figure 4.6: Bandwidth efficiency of LTE with perfect CQI feedback, comparing to channel capacity

4.2 Channel statistics

To compensate temporal variation, statistics of the SINR are first investigated. Due to the orthogonality of OFDM, every subcarrier can be treated in the same way independently. Therefore, an arbitrary subcarrier is chosen to represent the problem and the subcarrier index k is omitted here, for the reason of simplicity.

Define the power of the signal received by UE i from cell j as

$$P_{i,j}(t) \triangleq \frac{|H_{i,j}(t)|^2 G_j(t) U_j(t)}{L_{i,j}(t)}, \quad \text{for} \quad j \in \mathcal{S}. \tag{4.7}$$

To derive the second order statistics, the following assumptions are made [100]:

1. Assume the network is overloaded, which means $U_j(t) > 0, \forall j, t$.
2. Assume the Tx power is time invariant and the same for all eNBs. Therefore, $U_j(t)$ becomes a constant.
3. Assume the orientation of antennas does not change, and thus $G_j(t)$ becomes constant.
4. Assume Δt is small enough, so that the relative location of the UE to the eNB does not change significantly. Accordingly, in the log distance pathloss models, $L_{i,j}(t)$ can also be regarded as a constant.

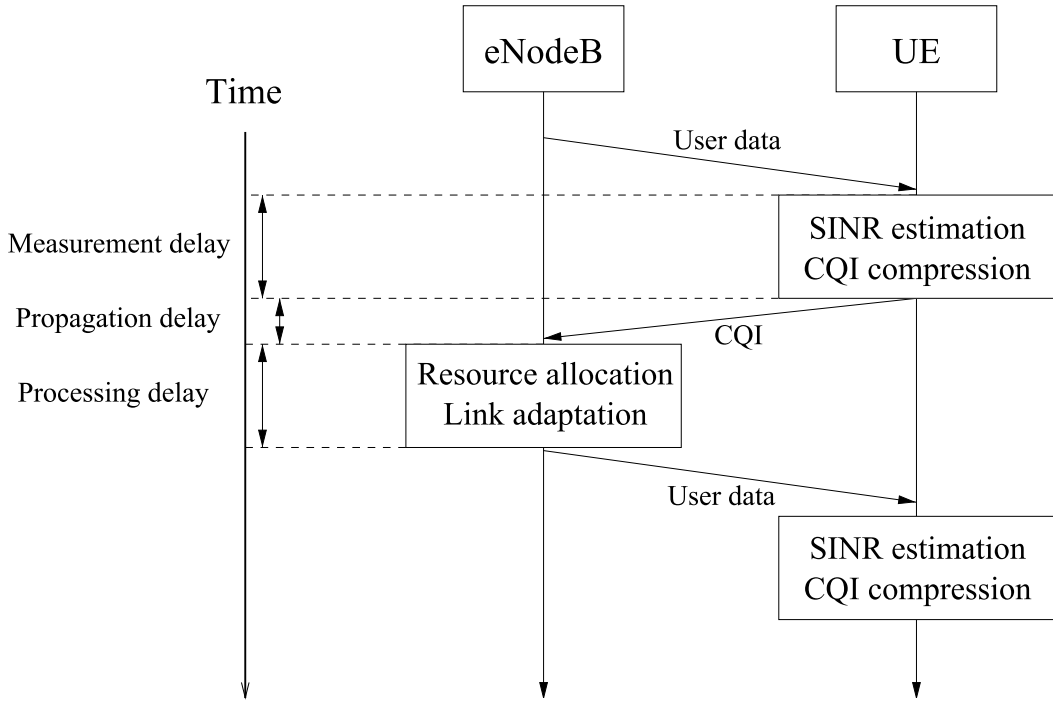

Figure 4.7: Time sequence for CQI feedback in LTE systems

5. Assume the CFR is normalized, i.e., $\mathrm{E}\{|H_{i,j}(t)|\} = 1$. The average Rx power can be defined as

$$\overline{P}_{i,j} \triangleq \frac{U_j(t)G_j(t)}{L_{i,j}(t)}. \tag{4.8}$$

6. Assume all the cells are using the same wireless communication standard. That means all the interfering signals have the same symbol duration and carrier frequency as the useful signal. Thus, the CFRs for all different eNB-UE pairs are i.i.d. processes. Consequently, the statistics of $H_{i,j}(t), j \in \mathcal{S}$ are independent of j.

7. Furthermore, $|H_{i,j}(t)|^2$ is assumed to be a Rayleigh fading process with autocorrelation function of $J_0(2\pi f_{\mathrm{D}}\Delta t)$

Applying these assumptions, (4.7) becomes

$$P_{i,j}(t) = \overline{P}_{i,j}\,|H_{i,j}(t)|^2, \quad \text{for} \quad j \in \mathcal{S}. \tag{4.9}$$

Statistical properties of SINR can be derived from this simplified expression.

4.2.1 Expectation of SINR

The expectation of the SINR is given by

$$\mathrm{E}\{\gamma(t)\} = \mathrm{E}\left\{\frac{P_{i,s}(t)}{\sum\limits_{j\in\mathcal{S}\setminus s} P_{i,j}(t) + \sigma_w^2}\right\} \tag{4.10}$$

Since $P_{i,s}$ and $P_{i,j}$ are independent, the numerator and denominator in (4.10) are considered separately as the product:

$$\mathrm{E}\{\gamma(t)\} = \mathrm{E}\left\{P_{i,s}(t)\right\}\mathrm{E}\left\{\frac{1}{\sum\limits_{j\in\mathcal{S}\setminus s} P_{i,j}(t) + \sigma_w^2}\right\} \tag{4.11}$$

The starting point of the calculation is the following equation:

$$\int_0^\infty z^{a-1}e^{-qz}\mathrm{d}z = \frac{\Gamma(a)}{q^a}, \tag{4.12}$$

where the Gamma function is defined as

$$\Gamma(a) = \int_0^\infty x^{a-1}e^{-x}\mathrm{d}x. \tag{4.13}$$

Equation (4.12) can be proved by defining a variable

$$x = qz, \tag{4.14}$$

and thus the differential becomes:

$$\mathrm{d}x = q\mathrm{d}z. \tag{4.15}$$

After substituting z with x, (4.12) becomes

$$\int_0^\infty z^{a-1}e^{-qz}\mathrm{d}z = \frac{1}{q}\int_0^\infty \left(\frac{x}{q}\right)^{a-1} e^{-x}\mathrm{d}x \tag{4.16}$$

$$= \frac{1}{q^a}\int_0^\infty x^{a-1}e^{-x}\mathrm{d}x \tag{4.17}$$

$$= \frac{\Gamma(a)}{q^a}, \tag{4.18}$$

and thus

$$\frac{1}{q^a} = \frac{1}{\Gamma(a)} \int_0^\infty z^{a-1} e^{-qz} \mathrm{d}z. \tag{4.19}$$

Since

$$\Gamma(1) = 0! = 1, \tag{4.20}$$

taking the special case of (4.19) with $a = 1$, the following equation can be obtained:

$$\frac{1}{q} = \int_0^\infty e^{-qz} \mathrm{d}z. \tag{4.21}$$

And (4.11) can be written as

$$\mathrm{E}\{\gamma(t)\} = \mathrm{E}\left\{P_{i,s}(t)\right\} \mathrm{E}\left\{ \int_0^\infty \exp\left\{ -z \left(\sum_{j \in \mathcal{S} \setminus s} P_{i,j}(t) + \sigma_w^2 \right) \right\} \mathrm{d}z \right\}, \tag{4.22}$$

where parameter z holds no physical meaning. Further assume that the Rx power from different cells are mutually independent, (4.11) becomes

$$\mathrm{E}\{\gamma(t)\} = \mathrm{E}\left\{P_{i,s}(t)\right\} \int_0^\infty \exp\left\{-z\sigma_w^2\right\} \prod_{j \in \mathcal{S} \setminus s} \mathrm{E}\left\{\exp\left\{-zP_{i,j}(t)\right\}\right\} \mathrm{d}z. \tag{4.23}$$

The first expectation term in (4.23) can be calculated according to (4.9). Since $\overline{P}_{i,s}$ and $H_{i,s}(t)$ are independent, and $H(t)$ is normalized to

$$\mathrm{E}\left\{|H(t)|^2\right\} = 1, \tag{4.24}$$

it is easy to obtain

$$\mathrm{E}\left\{P_{i,s}(t)\right\} = \overline{P}_{i,s}. \tag{4.25}$$

The calculation of the second expectation term in (4.23) is based on the Gaussian distribution of $H_{\mathrm{I}}(t)$ and $H_{\mathrm{Q}}(t)$. For complex valued CFR

$$H(t) = H_{\mathrm{I}}(t) + \jmath H_{\mathrm{Q}}(t), \tag{4.26}$$

where $H_{\mathrm{I}}(t)$ and $H_{\mathrm{Q}}(t)$ are the in-phase and quadrature components of $H(t)$, respectively. $|H(t)|^2$ can be written as

$$|H(t)|^2 = H_{\mathrm{I}}^2(t) + H_{\mathrm{Q}}^2(t). \tag{4.27}$$

Since the normalized CFR has unit variance, the variances of $H_{\mathrm{I}}(t)$ and $H_{\mathrm{Q}}(t)$ are

$$\mathrm{var}\{H_{\mathrm{I}}(t)\} = \mathrm{var}\{H_{\mathrm{Q}}(t)\} = \frac{1}{2}. \tag{4.28}$$

The second expectation term in (4.23) can be written as

$$\mathrm{E}\left\{\exp\left\{-zP_{i,j}(t)\right\}\right\} = \mathrm{E}\left\{\exp\left\{-z\overline{P}_{i,j}(H^2_{\mathrm{I},i,j}(t) + H^2_{\mathrm{Q},i,j}(t))\right\}\right\}. \tag{4.29}$$

Due to the independence between $H_{\mathrm{I},i,j}(t)$ and $H_{\mathrm{Q},i,j}(t)$, (4.29) can be factored into

$$\mathrm{E}\left\{\exp\left\{-zP_{i,j}(t)\right\}\right\} = \mathrm{E}\left\{\exp\left\{-z\overline{P}_{i,j}H^2_{\mathrm{I},i,j}(t)\right\}\right\}\mathrm{E}\left\{\exp\left\{-z\overline{P}_{i,j}H^2_{\mathrm{Q},i,j}(t)\right\}\right\}. \tag{4.30}$$

Both $H_{\mathrm{I},i,j}(t)$ and $H_{\mathrm{Q},i,j}(t)$ follow a Gaussian distribution $\mathcal{N}(0, \frac{1}{2})$. Therefore, taking the in-phase component as example, the first expectation term on the right side of (4.30) can be calculated as

$$\mathrm{E}\left\{\exp\left\{-z\overline{P}_{i,j}H^2_{\mathrm{I},i,j}(t)\right\}\right\} = \int_{-\infty}^{\infty} \exp\left\{-z\overline{P}_{i,j}H^2_{\mathrm{I},i,j}(t)\right\} \cdot \frac{1}{\sqrt{\pi}} \exp\left\{-H^2_{\mathrm{I},i,j}(t)\right\} \mathrm{d}H_{\mathrm{I},i,j}(t) \tag{4.31}$$

$$= \frac{1}{\sqrt{\pi}} \int_{-\infty}^{\infty} \exp\left\{-(z\overline{P}_{i,j}+1)H^2_{\mathrm{I},i,j}(t)\right\} \mathrm{d}H_{\mathrm{I},i,j}(t). \tag{4.32}$$

Using the Gaussian integral

$$\int_{-\infty}^{\infty} \exp\{-x^2\}\mathrm{d}x = \sqrt{\pi}, \tag{4.33}$$

(4.32) can be simplified to

$$\mathrm{E}\left\{\exp\left\{-z\overline{P}_{i,j}H^2_{\mathrm{I},i,j}(t)\right\}\right\} = \frac{1}{\sqrt{z\overline{P}_{i,j}+1}}, \tag{4.34}$$

and thus,

$$\mathrm{E}\left\{\exp\left\{-zP_{i,j}(t)\right\}\right\} = \frac{1}{z\overline{P}_{i,j}+1}. \tag{4.35}$$

Finally, (4.23) is simplified to

$$\mathrm{E}\{\gamma(t)\} = \overline{P}_{i,s} \int_{0}^{\infty} \exp\left\{-z\sigma_w^2\right\} \prod_{j\in\mathcal{S}\setminus s} \frac{1}{z\overline{P}_{i,j}+1} \mathrm{d}z. \tag{4.36}$$

4.2.2 Higher-order moments of SINR

The order ν ($\nu \geq 2$) moment of SINR is given by

$$\mathrm{E}\{(\gamma(t))^{\nu}\} = \mathrm{E}\left\{\left(\frac{P_{i,s}(t)}{\sum\limits_{j\in\mathcal{S}\setminus s} P_{i,j}(t) + \sigma_w^2}\right)^{\nu}\right\}. \tag{4.37}$$

By applying (4.19), (4.37) becomes

$$\mathrm{E}\{(\gamma(t))^{\nu}\} = \mathrm{E}\left\{P_{i,s}^{\nu}(t)\right\} \mathrm{E}\left\{\left(\frac{1}{\sum\limits_{j\in\mathcal{S}\setminus s} P_{i,j}(t) + \sigma_w^2}\right)^{\nu}\right\} \tag{4.38}$$

$$= \mathrm{E}\left\{P_{i,s}^{\nu}(t)\right\} \frac{1}{\Gamma(\nu)} \int_0^{\infty} z^{\nu-1} \exp\left\{-z\sigma_w^2\right\} \prod_{j\in\mathcal{S}\setminus s} \mathrm{E}\left\{-zP_{i,j}(t)\right\} \mathrm{d}z. \tag{4.39}$$

Using (4.35), (4.39) can be written as

$$\mathrm{E}\{(\gamma(t))^{\nu}\} = \frac{\mathrm{E}\left\{P_{i,s}^{\nu}(t)\right\}}{\Gamma(\nu)} \int_0^{\infty} z^{\nu-1} \exp\left\{-z\sigma_w^2\right\} \prod_{j\in\mathcal{S}\setminus s} \frac{1}{z\overline{P}_{i,j}+1} \mathrm{d}z. \tag{4.40}$$

Although it is difficult to give an universal expression for $\mathrm{E}\left\{P_{i,s}^{\nu}(t)\right\}$, some special cases can be calculated. One example is the second order moment, which can be used for calculating the variance of SINR.

4.2.3 Variance of SINR

The variance of SINR can be calculated with

$$\mathrm{var}\{\gamma(t)\} = \mathrm{E}\{\gamma^2(t)\} - \mathrm{E}^2\{\gamma(t)\} \tag{4.41}$$

Using (4.40) with $\nu = 2$, $\mathrm{E}\{\gamma_{i,s}^2(t)\}$ becomes

$$\mathrm{E}\{(\gamma(t))^2\} = \frac{\mathrm{E}\left\{P_{i,s}^2(t)\right\}}{\Gamma(2)} \int_0^{\infty} z \exp\left\{-z\sigma_w^2\right\} \prod_{j\in\mathcal{S}\setminus s} \frac{1}{z\overline{P}_{i,j}+1} \mathrm{d}z, \tag{4.42}$$

where the Gamma function,

$$\Gamma(2) = 1! = 1. \tag{4.43}$$

$\mathrm{E}\left\{P_{i,s}^2(t)\right\}$ can be written as

$$\mathrm{E}\{P_{i,s}^2(t)\} = \overline{P}_{i,s}^2 \mathrm{E}\{|H_{i,j}(t)|^4\} \tag{4.44}$$

$$= \overline{P}_{i,s}^2 \left(\mathrm{E}\left\{H_{\mathrm{I},i,j}^4(t)\right\} + \mathrm{E}\left\{H_{\mathrm{Q},i,j}^4(t)\right\} + 2\mathrm{E}\left\{H_{\mathrm{I},i,j}^2(t)\right\} \mathrm{E}\left\{H_{\mathrm{Q},i,j}^2(t)\right\}\right). \tag{4.45}$$

The even order moments of a Gaussian distributed variable can be calculated with its variance and moment order [88]

$$\mathrm{E}\{H_{\mathrm{I}}^p\} = \left(\sqrt{\mathrm{var}\{H_{\mathrm{I}}\}}\right)^p (p-1)!!, \tag{4.46}$$

where p is an even number, !! denotes double factorial. Using (4.28), the expression in (4.45) is simplified to

$$\mathrm{E}\{P_{i,s}^2(t)\} = \overline{P}_{i,s}^2 \left(\frac{3}{4} + \frac{3}{4} + 2 \cdot \frac{1}{2} \cdot \frac{1}{2}\right) = 2\overline{P}_{i,s}^2. \tag{4.47}$$

Therefore, the expectation of the squared SINR is

$$\mathrm{E}\{\gamma^2(t)\} = 2\overline{P}_{i,s}^2 \int_0^\infty z \cdot \exp\left\{-\sigma_w^2 z\right\} \prod_{j \in \mathcal{S}\setminus s} \frac{1}{z\overline{P}_{i,j} + 1} \mathrm{d}z. \tag{4.48}$$

And thus, the variance of the SINR can be calculated accordingly.

4.2.4 Autocorrelation function of SINR

The autocorrelation function of SINR can be written as

$$\begin{aligned} R_{\gamma\gamma}(\Delta t) &= \mathrm{E}\left\{\gamma(t_1)\gamma(t_2)\right\} && (4.49) \\ &= \mathrm{E}\left\{\frac{P_{i,s}(t_1)}{\sum\limits_{j \in \mathcal{S}\setminus s} P_{i,j}(t_1) + \sigma_w^2} \cdot \frac{P_{i,s}(t_2)}{\sum\limits_{j \in \mathcal{S}\setminus s} P_{i,j}(t_2) + \sigma_w^2}\right\}. && (4.50) \end{aligned}$$

Since $P_{i,s}$ and $P_{i,j}$ are independent, the numerator and denominator in (4.50) can be considered separately.

Using (4.21), the SINR is written as

$$\begin{aligned} \gamma(t) &= P_{i,s}(t) \cdot \frac{1}{\sum\limits_{j \in \mathcal{S}\setminus s} P_{i,j}(t) + \sigma_w^2} \\ &= P_{i,s}(t) \int_0^\infty \exp\left\{-z\left(\sum_{j \in \mathcal{S}\setminus s} P_{i,j}(t) + \sigma_w^2\right)\right\} \mathrm{d}z. && (4.51) \end{aligned}$$

Applying (4.51) to (4.50) results in

$$\begin{aligned} R_{\gamma\gamma}(\Delta t) = \mathrm{E}\Bigg\{ & P_{i,s}(t_1)P_{i,s}(t_2) \cdot \int_0^\infty \int_0^\infty \exp\left\{-z_1\left(\sum_{j \in \mathcal{S}\setminus s} P_{i,j}(t_1) + \sigma_w^2\right)\right. \\ & \left. -z_2\left(\sum_{j \in \mathcal{S}\setminus s} P_{i,j}(t_2) + \sigma_w^2\right)\right\} \mathrm{d}z_1 \mathrm{d}z_2 \Bigg\}. \end{aligned} \tag{4.52}$$

Assuming the received powers from different cells $P_{i,j}(t), j \in \{1, 2, \cdots, S\}$ are independent to each other, (4.52) becomes

$$\begin{aligned} R_{\gamma\gamma}(\Delta t) &= \mathrm{E}\left\{P_{i,s}(t_1)P_{i,s}(t_2)\right\} \int_0^\infty \int_0^\infty \exp\{-\sigma_w^2(z_1+z_2)\} \\ &\quad \cdot \prod_{j\in\mathcal{S}\setminus s} \mathrm{E}\{\exp\{-z_1 P_{i,j}(t_1) - z_2 P_{i,j}(t_2)\}\}\mathrm{d}z_1\mathrm{d}z_2. \end{aligned} \tag{4.53}$$

The first expectation term in (4.53) is written as:

$$\mathrm{E}\left\{P_{i,s}(t_1)P_{i,s}(t_2)\right\} = \mathrm{E}\left\{\overline{P}_{i,s}\left|H_{i,s}(t_1)\right|^2 \overline{P}_{i,s}\left|H_{i,s}(t_2)\right|^2\right\} \tag{4.54}$$

$$= \overline{P}_{i,s}^2 \mathrm{E}\left\{\left|H_{i,s}(t_1)\right|^2 \left|H_{i,s}(t_2)\right|^2\right\}. \tag{4.55}$$

Using the in-phase and quadrature components $H_{\mathrm{I}}(t)$ and $H_{\mathrm{Q}}(t)$, $\mathrm{E}\left\{\left|H(t_1)\right|^2\left|H(t_2)\right|^2\right\}$ can be written as

$$\begin{aligned} & \mathrm{E}\left\{\left|H(t_1)\right|^2\left|H(t_2)\right|^2\right\} \\ = \; & \mathrm{E}\left\{(H_{\mathrm{I}}^2(t_1)+H_{\mathrm{Q}}^2(t_1))(H_{\mathrm{I}}^2(t_2)+H_{\mathrm{Q}}^2(t_2))\right\} \\ = \; & \mathrm{E}\left\{H_{\mathrm{I}}^2(t_1)H_{\mathrm{I}}^2(t_2) + H_{\mathrm{I}}^2(t_1)H_{\mathrm{Q}}^2(t_2) + H_{\mathrm{Q}}^2(t_1)H_{\mathrm{I}}^2(t_2) + H_{\mathrm{Q}}^2(t_1)H_{\mathrm{Q}}^2(t_2)\right\} \\ = \; & \mathrm{E}\left\{H_{\mathrm{I}}^2(t_1)H_{\mathrm{I}}^2(t_2)\right\} + \mathrm{E}\left\{H_{\mathrm{I}}^2(t_1)H_{\mathrm{Q}}^2(t_2)\right\} \\ & + \mathrm{E}\left\{H_{\mathrm{Q}}^2(t_1)H_{\mathrm{I}}^2(t_2)\right\} + \mathrm{E}\left\{H_{\mathrm{Q}}^2(t_1)H_{\mathrm{Q}}^2(t_2)\right\}. \end{aligned} \tag{4.56}$$

Since in Rayleigh fading channels, both H_{I} and H_{Q} are Gaussian distributed with zero mean, according to Isserlis' theorem [12], the first term in (4.56) can be calculated as

$$\begin{aligned} & \mathrm{E}\left\{H_{\mathrm{I}}^2(t_1)H_{\mathrm{I}}^2(t_2)\right\} \\ = \; & \mathrm{E}\left\{H_{\mathrm{I}}(t_1)H_{\mathrm{I}}(t_1)\right\}\mathrm{E}\left\{H_{\mathrm{I}}(t_2)H_{\mathrm{I}}(t_2)\right\} + 2\mathrm{E}\left\{H_{\mathrm{I}}(t_1)H_{\mathrm{I}}(t_2)\right\}\mathrm{E}\left\{H_{\mathrm{I}}(t_1)H_{\mathrm{I}}(t_2)\right\} \\ = \; & \mathrm{E}\left\{H_{\mathrm{I}}^2(t_1)\right\}\mathrm{E}\left\{H_{\mathrm{I}}^2(t_2)\right\} + 2\mathrm{E}^2\left\{H_{\mathrm{I}}(t_1)H_{\mathrm{I}}(t_2)\right\}. \end{aligned} \tag{4.57}$$

The same process can be applied to the other terms from (4.56) as

$$\begin{aligned} & \mathrm{E}\left\{H_{\mathrm{I}}^2(t_1)\; H_{\mathrm{Q}}^2(t_2)\right\} \\ & \qquad = \mathrm{E}\left\{H_{\mathrm{I}}^2(t_1)\right\}\mathrm{E}\left\{H_{\mathrm{Q}}^2(t_2)\right\} + 2\mathrm{E}^2\left\{H_{\mathrm{I}}(t_1)H_{\mathrm{Q}}(t_2)\right\} \end{aligned} \tag{4.58}$$

$$\begin{aligned} & \mathrm{E}\left\{H_{\mathrm{Q}}^2(t_1)\; H_{\mathrm{I}}^2(t_2)\right\} \\ & \qquad = \mathrm{E}\left\{H_{\mathrm{Q}}^2(t_1)\right\}\mathrm{E}\left\{H_{\mathrm{I}}^2(t_2)\right\} + 2\mathrm{E}^2\left\{H_{\mathrm{Q}}(t_1)H_{\mathrm{I}}(t_2)\right\} \end{aligned} \tag{4.59}$$

$$\begin{aligned} & \mathrm{E}\left\{H_{\mathrm{Q}}^2(t_1)\; H_{\mathrm{Q}}^2(t_2)\right\} \\ & \qquad = \mathrm{E}\left\{H_{\mathrm{Q}}^2(t_1)\right\}\mathrm{E}\left\{H_{\mathrm{Q}}^2(t_2)\right\} + 2\mathrm{E}^2\left\{H_{\mathrm{Q}}(t_1)H_{\mathrm{Q}}(t_2)\right\}. \end{aligned} \tag{4.60}$$

And (4.56) becomes

$$\begin{aligned}
& \mathrm{E}\left\{|H(t_1)|^2 |H(t_2)|^2\right\} \\
= \; & \mathrm{E}\left\{H_{\mathrm{I}}^2(t_1)\right\}\mathrm{E}\left\{H_{\mathrm{I}}^2(t_2)\right\} + 2\mathrm{E}^2\left\{H_{\mathrm{I}}(t_1)H_{\mathrm{I}}(t_2)\right\} \\
& +\mathrm{E}\left\{H_{\mathrm{I}}^2(t_1)\right\}\mathrm{E}\left\{H_{\mathrm{Q}}^2(t_2)\right\} + 2\mathrm{E}^2\left\{H_{\mathrm{I}}t_1)H_{\mathrm{Q}}(t_2)\right\} \\
& +\mathrm{E}\left\{H_{\mathrm{Q}}^2(t_1)\right\}\mathrm{E}\left\{H_{\mathrm{I}}^2(t_2)\right\} + 2\mathrm{E}^2\left\{H_{\mathrm{Q}}(t_1)H_{\mathrm{I}}(t_2)\right\} \\
& +\mathrm{E}\left\{H_{\mathrm{Q}}^2(t_1)\right\}\mathrm{E}\left\{H_{\mathrm{Q}}^2(t_2)\right\} + 2\mathrm{E}^2\left\{H_{\mathrm{Q}}(t_1)H_{\mathrm{Q}}(t_2)\right\} \qquad (4.61) \\
= \; & \mathrm{E}^2\left\{H_{\mathrm{I}}^2(t)\right\} + \mathrm{E}^2\left\{H_{\mathrm{Q}}^2(t)\right\} + \mathrm{E}\left\{H_{\mathrm{I}}^2(t)\right\}\mathrm{E}\left\{H_{\mathrm{Q}}^2(t)\right\} + \mathrm{E}\left\{H_{\mathrm{Q}}^2(t)\right\}\mathrm{E}\left\{H_{\mathrm{I}}^2(t)\right\} \\
& +2\left(\mathrm{E}^2\left\{H_{\mathrm{I}}(t_1)H_{\mathrm{I}}(t_2)\right\} + \mathrm{E}^2\left\{H_{\mathrm{I}}(t_1)H_{\mathrm{Q}}(t_2)\right\}\right. \\
& \left.+\mathrm{E}^2\left\{H_{\mathrm{Q}}(t_1)H_{\mathrm{I}}(t_2)\right\} + \mathrm{E}^2\left\{H_{\mathrm{Q}}(t_1)H_{\mathrm{Q}}(t_2)\right\}\right) \qquad (4.62) \\
= \; & R_{H_{\mathrm{I}}H_{\mathrm{I}}}^2(0) + R_{H_{\mathrm{Q}}H_{\mathrm{Q}}}^2(0) + R_{H_{\mathrm{I}}H_{\mathrm{I}}}(0)R_{H_{\mathrm{Q}}H_{\mathrm{Q}}}(0) + R_{H_{\mathrm{Q}}H_{\mathrm{Q}}}(0)R_{H_{\mathrm{I}}H_{\mathrm{I}}}(0) \\
& +2\left(R_{H_{\mathrm{I}}H_{\mathrm{I}}}^2(\Delta t) + R_{H_{\mathrm{I}}H_{\mathrm{Q}}}^2(\Delta t) + R_{H_{\mathrm{Q}}H_{\mathrm{I}}}^2(\Delta t) + R_{H_{\mathrm{Q}}H_{\mathrm{Q}}}^2(\Delta t)\right), \qquad (4.63)
\end{aligned}$$

where $R_{H_{\mathrm{I}}H_{\mathrm{I}}}$, $R_{H_{\mathrm{Q}}H_{\mathrm{Q}}}$, $R_{H_{\mathrm{I}}H_{\mathrm{Q}}}$ and $R_{H_{\mathrm{Q}}H_{\mathrm{I}}}$ are autocorrelation and cross-correlation functions of the in-phase and quadrature components. Since all the interfering signals have the same symbol duration and carrier frequency as the useful signal. These autocorrelation and cross-correlation functions are the same for $H_{i,j}, \forall j \in \mathcal{S}$. Furthermore, define

$$r(\Delta t) = J_0(2\pi f_{\mathrm{D}} \Delta t). \qquad (4.64)$$

According to (2.12), similar to (3.6) and (3.7), the following relationship holds true

$$R_{H_{\mathrm{I}}H_{\mathrm{I}}}(\Delta t) = R_{H_{\mathrm{Q}}H_{\mathrm{Q}}}(\Delta t) = \frac{1}{2} r(\Delta t) \qquad (4.65)$$

$$R_{H_{\mathrm{I}}H_{\mathrm{Q}}}(\Delta t) = R_{H_{\mathrm{Q}}H_{\mathrm{I}}}(\Delta t) \; = 0. \qquad (4.66)$$

And (4.55) becomes

$$\begin{aligned}
\mathrm{E}\left\{P_{i,s}(t_1)P_{i,s}(t_2)\right\} &= \overline{P}_{i,s}^2\left(4R_{H_{\mathrm{I}}H_{\mathrm{I}}}^2(0) + 4R_{H_{\mathrm{I}}H_{\mathrm{I}}}^2(\Delta t)\right) \\
&= \overline{P}_{i,s}^2\left(1 + r^2(\Delta t)\right). \qquad (4.67)
\end{aligned}$$

The calculation of the second expectation term in (4.53) is based on the multivariate Gaussian distribution of $H_{\mathrm{I},i,j}(t_1)$, $H_{\mathrm{Q},i,j}(t_1)$, $H_{\mathrm{I},i,j}(t_2)$ and $H_{\mathrm{Q},i,j}(t_2)$.

Define

$$\mathbf{P}_{\mathrm{I},i,j} \triangleq \overline{P}_{i,j}\begin{bmatrix} H_{\mathrm{I},i,j}(t_1) \\ H_{\mathrm{I},i,j}(t_2) \end{bmatrix} \quad \text{and} \quad \mathbf{P}_{\mathrm{Q},i,j} \triangleq \overline{P}_{i,j}\begin{bmatrix} H_{\mathrm{Q},i,j}(t_1) \\ H_{\mathrm{Q},i,j}(t_2) \end{bmatrix}. \qquad (4.68)$$

The second expectation term in (4.53) can be written as

$$\begin{aligned}
& \mathrm{E}\{\exp\{-z_1 P_{i,j}(t_1) - z_2 P_{i,j}(t_2)\}\} \\
= \; & \mathrm{E}\left\{\exp\left\{-[\mathbf{P}_{\mathrm{I},i,j}^{\mathrm{T}} \quad \mathbf{P}_{\mathrm{Q},i,j}^{\mathrm{T}}]\begin{bmatrix} \mathrm{diag}(\mathbf{z}) & 0 \\ 0 & \mathrm{diag}(\mathbf{z}) \end{bmatrix}\begin{bmatrix} \mathbf{P}_{\mathrm{I},i,j} \\ \mathbf{P}_{\mathrm{Q},i,j} \end{bmatrix}\right\}\right\} \qquad (4.69)
\end{aligned}$$

where

$$\mathrm{diag}(\mathbf{z}) = \begin{bmatrix} z_1 & 0 \\ 0 & z_2 \end{bmatrix}. \tag{4.70}$$

The joint probability density function (pdf) of the in-phase and quadrature components of $P_{i,j}(t_1)$ and $P_{i,j}(t_2)$ is given by

$$\begin{aligned} p_{\mathbf{P}_{\mathrm{I},i,j},\mathbf{P}_{\mathrm{Q},i,j}}(\mathbf{p}_{\mathrm{I},i,j}\mathbf{p}_{\mathrm{Q},i,j}) &= \frac{1}{(2\pi)^2(\det(\mathbf{\Sigma}))^{\frac{1}{2}}} \\ &\quad \cdot \exp\left\{-\frac{1}{2}[\mathbf{p}_{\mathrm{I},i,j}^{\mathrm{T}} \quad \mathbf{p}_{\mathrm{Q},i,j}^{\mathrm{T}}]\mathbf{\Sigma}^{-1}\begin{bmatrix} \mathbf{p}_{\mathrm{I},i,j} \\ \mathbf{p}_{\mathrm{Q},i,j} \end{bmatrix}\right\}, \end{aligned} \tag{4.71}$$

where $\mathbf{\Sigma}$ is the covariance matrix defined as

$$\mathbf{\Sigma} \triangleq \overline{P}_{i,j}\begin{bmatrix} R_{H_\mathrm{I}H_\mathrm{I}}(0) & R_{H_\mathrm{I}H_\mathrm{I}}(\Delta t) & R_{H_\mathrm{I}H_\mathrm{Q}}(0) & R_{H_\mathrm{I}H_\mathrm{Q}}(\Delta t) \\ R_{H_\mathrm{I}H_\mathrm{I}}(\Delta t) & R_{H_\mathrm{I}H_\mathrm{I}}(0) & R_{H_\mathrm{I}H_\mathrm{Q}}(\Delta t) & R_{H_\mathrm{I}H_\mathrm{Q}}(0) \\ R_{H_\mathrm{I}H_\mathrm{Q}}(0) & R_{H_\mathrm{I}H_\mathrm{Q}}(\Delta t) & R_{H_\mathrm{Q}H_\mathrm{Q},i}(0) & R_{H_\mathrm{Q}H_\mathrm{Q}}(\Delta t) \\ R_{H_\mathrm{I}H_\mathrm{Q}}(\Delta t) & R_{H_\mathrm{I}H_\mathrm{Q}}(0) & R_{H_\mathrm{Q}H_\mathrm{Q}}(dt) & R_{H_\mathrm{Q}H_\mathrm{Q}}(0) \end{bmatrix}. \tag{4.72}$$

Using (4.65) and (4.66), $\mathbf{\Sigma}$ is written as

$$\mathbf{\Sigma} = \frac{\overline{P}_{i,j}}{2}\begin{bmatrix} 1 & r(\Delta t) & 0 & 0 \\ r(\Delta t) & 1 & 0 & 0 \\ 0 & 0 & 1 & r(\Delta t) \\ 0 & 0 & r(\Delta t) & 1 \end{bmatrix}. \tag{4.73}$$

By definition, the expectation in (4.69) is calculated using the Gaussian pdf as

$$\begin{aligned} &\mathrm{E}\{\exp\{-z_1P_{i,j}(t_1) - z_2P_{i,j}(t_2)\}\} \\ &= \int_{-\infty}^{\infty}\cdots\int_{-\infty}^{\infty}\exp\left\{-[\mathbf{p}_{\mathrm{I},i,j}^{\mathrm{T}} \quad \mathbf{p}_{\mathrm{Q},i,j}^{\mathrm{T}}]\begin{bmatrix} \mathrm{diag}(\mathbf{z}) & 0 \\ 0 & \mathrm{diag}(\mathbf{z}) \end{bmatrix}\begin{bmatrix} \mathbf{p}_{\mathrm{I},i,j} \\ \mathbf{p}_{\mathrm{Q},i,j} \end{bmatrix}\right\} \\ &\quad \cdot\frac{1}{(2\pi)^2(\det(\mathbf{\Sigma}))^{\frac{1}{2}}}\exp\left\{-\frac{1}{2}[\mathbf{p}_{\mathrm{I},i,j}^{\mathrm{T}} \quad \mathbf{p}_{\mathrm{Q},i,j}^{\mathrm{T}}]\mathbf{\Sigma}^{-1}\begin{bmatrix} \mathbf{p}_{\mathrm{I},i,j} \\ \mathbf{p}_{\mathrm{Q},i,j} \end{bmatrix}\right\}\mathrm{d}\mathbf{p}_{\mathrm{I},i,j}\mathrm{d}\mathbf{p}_{\mathrm{Q},i,j} \end{aligned} \tag{4.74}$$

$$\begin{aligned} &= \frac{1}{(2\pi)^2(\det(\mathbf{\Sigma}))^{\frac{1}{2}}}\int_{-\infty}^{\infty}\cdots\int_{-\infty}^{\infty} \\ &\quad \exp\left\{-\frac{1}{2}[\mathbf{p}_{\mathrm{I},i,j}^{\mathrm{T}} \quad \mathbf{p}_{\mathrm{Q},i,j}^{\mathrm{T}}]\left(\mathbf{\Sigma}^{-1} + 2\begin{bmatrix} \mathrm{diag}(\mathbf{z}) & 0 \\ 0 & \mathrm{diag}(\mathbf{z}) \end{bmatrix}\right)\begin{bmatrix} \mathbf{p}_{\mathrm{I},i,j} \\ \mathbf{p}_{\mathrm{Q},i,j} \end{bmatrix}\right\} \\ &\quad \mathrm{d}\mathbf{p}_{\mathrm{I},i,j}\mathrm{d}\mathbf{p}_{\mathrm{Q},i,j}. \end{aligned} \tag{4.75}$$

Using the following identity

$$\frac{1}{(2\pi)^2}\int_{-\infty}^{\infty}\cdots\int_{-\infty}^{\infty}\exp\left\{-\frac{1}{2}\mathbf{x}^{\mathrm{T}}\mathbf{C}\mathbf{x}\right\}\mathrm{d}\mathbf{x} = (\det(\mathbf{C}))^{\frac{1}{2}}, \tag{4.76}$$

which is proven in Appendix A. (4.75) can be written as

$$\begin{aligned}
&\mathrm{E}\{\exp\{-z_1 P_{i,j}(t_1) - z_2 P_{i,j}(t_2)\}\} \\
&\qquad = \frac{1}{(\det(\mathbf{\Sigma}))^{\frac{1}{2}}} \left(\det\left(\mathbf{\Sigma}^{-1} + 2\begin{bmatrix} \mathrm{diag}(\mathbf{z}) & 0 \\ 0 & \mathrm{diag}(\mathbf{z}) \end{bmatrix}\right)\right)^{-\frac{1}{2}} && (4.77)\\
&\qquad = \left(\det\left(\mathbf{I} + 2\begin{bmatrix} \mathrm{diag}(\mathbf{z}) & 0 \\ 0 & \mathrm{diag}(\mathbf{z}) \end{bmatrix}\mathbf{\Sigma}\right)\right)^{-\frac{1}{2}} && (4.78)\\
&\qquad = \begin{vmatrix} 1+z_1\overline{P}_{i,j} & z_1\overline{P}_{i,j}r(\Delta t) & 0 & 0 \\ z_2\overline{P}_{i,j}r(\Delta t) & 1+z_2\overline{P}_{i,j} & 0 & 0 \\ 0 & 0 & 1+z_1\overline{P}_{i,j} & z_1\overline{P}_{i,j}r(\Delta t) \\ 0 & 0 & z_2\overline{P}_{i,j}r(\Delta t) & 1+z_2\overline{P}_{i,j} \end{vmatrix}^{-\frac{1}{2}} && (4.79)\\
&\qquad = \frac{1}{z_1 z_2 \overline{P}_{i,j}^2(1-r^2(\Delta t)) + (z_1+z_2)\overline{P}_{i,j} + 1}. && (4.80)
\end{aligned}$$

The autocorrelation function can be obtained by substituting (4.67) and (4.80) into (4.53)

$$\begin{aligned}
R_{\gamma\gamma}(\Delta t) =& \overline{P}_{i,s}^2\left(1 + r^2(\Delta t)\right) \int_0^\infty \int_0^\infty \exp\{-\sigma_w^2(z_1+z_2)\} \\
&\cdot \prod_{j\in\mathcal{S}\setminus s} \frac{1}{z_1 z_2 \overline{P}_{i,j}^2(1-r^2(\Delta t)) + (z_1+z_2)\overline{P}_{i,j} + 1} \mathrm{d}z_1 \mathrm{d}z_2. && (4.81)
\end{aligned}$$

And this expression can be calculated numerically.

4.2.5 Normalized autocovariance function and its approximation

Finally, the normalized autocovariance function is calculated by

$$C_{\gamma\gamma}(\Delta t) = \frac{R_{\gamma\gamma}(\Delta t) - \mathrm{E}^2\{\gamma(t)\}}{\mathrm{var}\{\gamma(t)\}}. \tag{4.82}$$

Although this autocovariance function depends on the average Rx power from all the cells, further experiments show that this dependency is quite weak. Moreover, a simple squared zero-order Bessel function of the first kind

$$c_{\gamma\gamma}(\Delta t) = J_0^2(2\pi f_\mathrm{D} \Delta t) \tag{4.83}$$

can offer a good approximation of (4.82).

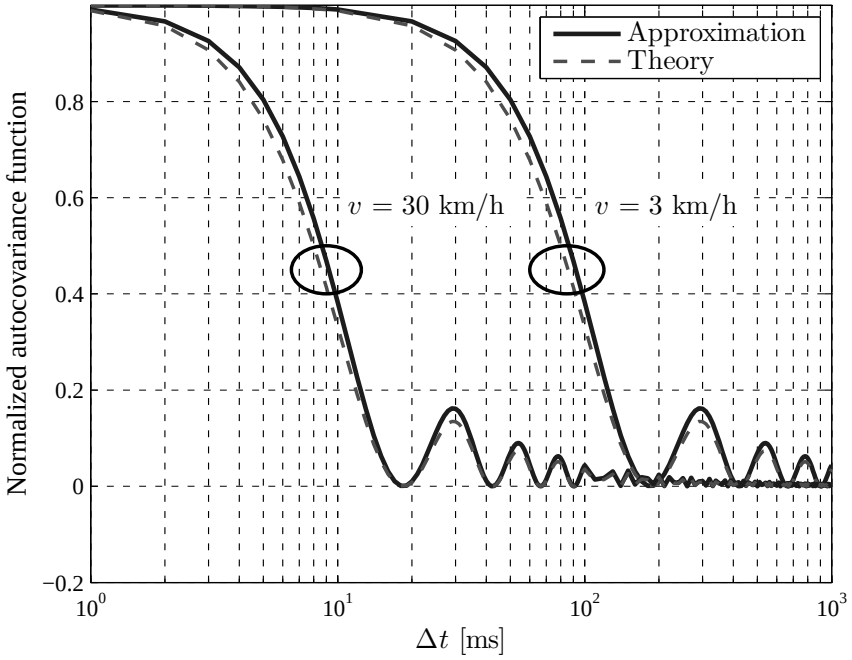

Figure 4.8: Normalized autocovariance function and approximation

4.2.6 Numerical results

Simulation setup

For the simulation, a cellular network with 19 eNBs and 57 cells is considered. The eNBs are equipped with 3-sector antennas. The inter-eNB distance is 500 meters. The network layout is as shown in Figure 5.5. One single UE moves randomly within a central cell in the middle. The pathloss model is

$$L_{i,j}(t) = 15.3 + 18.8 \log_{10} d_{i,j}(t) \tag{4.84}$$

where $d_{i,j}(t)$ is the distance between UE i and the eNB of cell j at time t. Some other parameters are summarized in Table 4.4. Most of the parameters follow 3GPP standards [9]. The channel responses following the Rayleigh fading model are generated using the sum-of-sinusoids method from [104].

Approximation

Figure 4.8 shows the normalized autocovariance function from (4.82) and the approximated one from (4.83) for UE traveling at 3 km/h and 30 km/h, respectively. It can be seen that although the average Rx power $\overline{P}_{i,j}, \forall j \in \mathcal{S}$, is involved in the calculation of the autocovariance function, it actually has minor influence on the final result. Therefore, (4.82) can be quite well approximated by (4.83). Since (4.83) depends on only two variables, it is much easier to calculate.

BS Tx power	46 dBm
Bandwidth	4.32 MHz
Carrier frequency	800 MHz
MS noise figure	9 dB
Mobility model	Random walk
Simulation runs	100,000

Table 4.4: Simulation parameters

Modeling accuracy

Among the assumptions made to derive the autocorrelation function, the strongest one is that with small Δt, the location of UE does not change. There are two major contributors to the variation of SINR, one is the fast fading process, and the other one is the spatial correlation of pathloss due to location change of the UE. When UE moves faster, this assumption becomes less legitimate. Therefore, a mismatch of the theoretic model and the simulation results is expected. To confirm that this mismatch is caused by the strong assumption, simulations considering only Rayleigh fading but not the location change of UE are also performed and compared.

In Figure 4.9, the approximated autocovariance is compared to simulation results. For simulations, which consider only Doppler shift but not the location change, the sample autocovariance matches the approximated autocovariance function quite well, even for larger Δt of higher speed. However, for simulations, which take the location change into account, an apparent mismatch can be observed. Moreover, for faster UE and larger Δt, the correlation of fading process approaches 0, but the correlation of path loss stops the sample covariance from getting to zero.

Estimating moving speed

Since the approximated autocovariance only depends on f_D and Δt, it can be used for a rough estimation of the moving speed of UE. For a fixed value of Δt, the dependency of $c_{\gamma\gamma}$ and f_D can be summarized into a look-up table. The moving UE can measure its sample autocovariance and use a one dimensional interpolation to find out its corresponding Doppler frequency. Thus, the velocity can be calculated by using (2.5). Since the squared Bessel function is not monotonic, this idea is only supposed to work for very small Δt.

The relationship of $c_{\gamma\gamma}$ and f_D is illustrated in Figure 4.10, where for a given sample autocovariance, the Doppler frequency can be directly found. The estimated speeds $\hat{v}$ are compared with actual speeds v for different Δt in Figure 4.11. A simple linear interpolation is used to obtain these results. For $\Delta t = 10$ ms, UE speed up to 40 km/h can be quite accurately estimated. For smaller Δt, the steep slope of the $c_{\gamma\gamma}$ - f_D curve amplifies the mismatch of sample autocovariance and the approximated one, and thus leads to a larger error. Nevertheless, the cost of implementing this algorithm

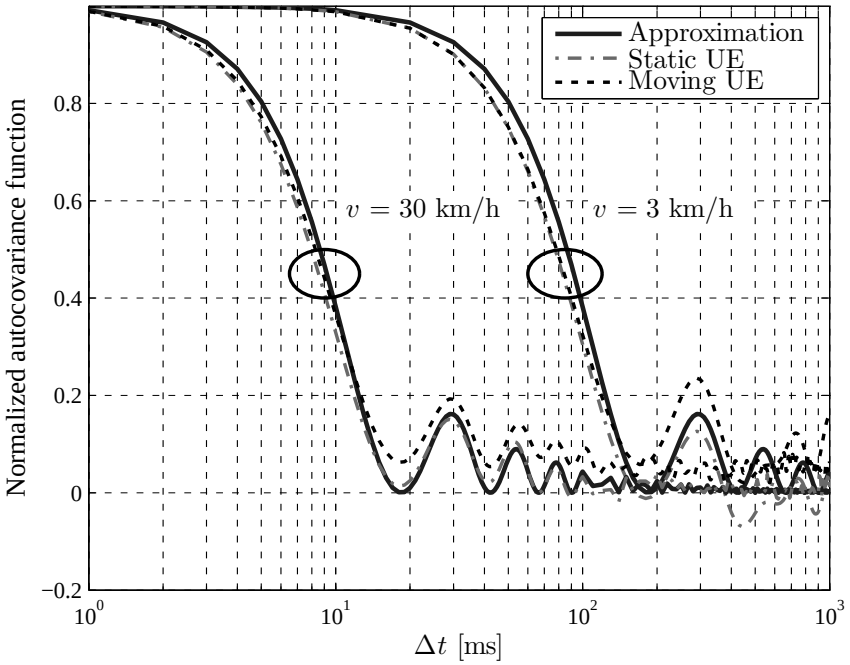

Figure 4.9: Approximated autocovariance function and simulation sample autocovariance with and without considering the location change of the UE

is extremely low due to its simplicity. And this method will be used later in this thesis to enable an adaptive CQI feedback scheme.

4.3 Compensation of temporal variation

With the help of channel statistics, some CQI prediction schemes can be derived. The compensation of temporal variation can be done either on the UE side or on the eNB side. The difference is: On the eNB side, only CQI is available. The prediction $\widehat{Q}$ must be purely based on previous knowledge of Q. The aforementioned noises can be amplified during the prediction process, causing an inaccurate result. On the UE side, the original information of SINR is available. The SINR $\widehat{\gamma}$ can be calculated and the corresponding CQI can be easily obtained with the aforementioned SINR to CQI mapping. Therefore, the prediction can be more accurate. However, mobile handsets generally have very limited battery power, which imposes a constraint on the computational complexity of the algorithms. In this work, only prediction schemes based on the SINR are investigated. The same algorithms can be applied to CQI in a straight forward manner. However, since CQI is a compressed and quantized version of SINR, as shown in Figure 4.12, the performance is expected to be worse than from the prediction algorithms directly working on CQI.

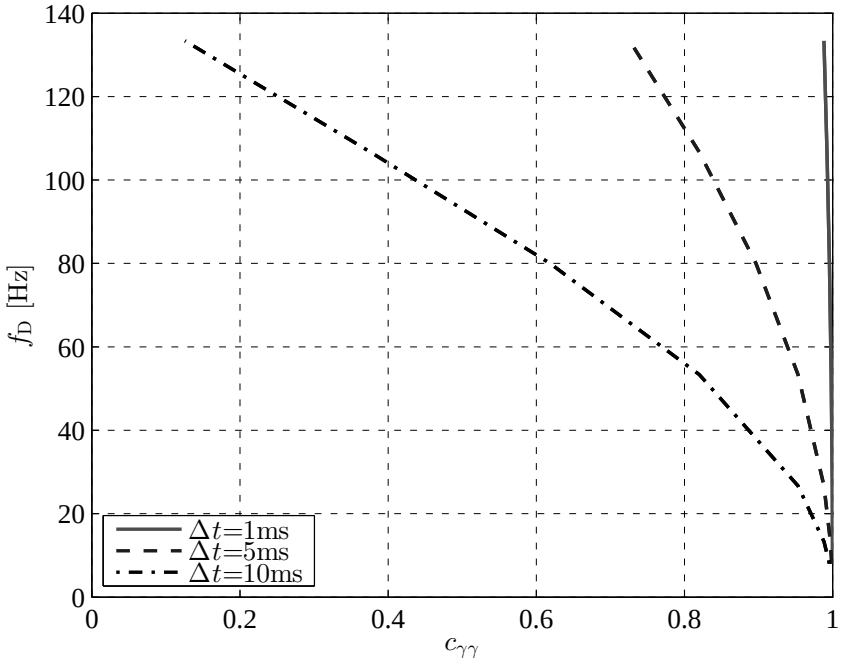

Figure 4.10: Approximated autocovariance and its relationship to f_D

4.3.1 Prediction accuracy and throughput

In the presence of noise, the throughput is reduced. After SINR prediction, the predicted SINR can be mapped to a predicted effective SNR $\widehat{\gamma}_e(t,b)$. For noisy prediction, it can be written as

$$\widehat{\gamma}_e(t,b) = \gamma_e(t,b) + \epsilon(t,b), \tag{4.85}$$

where $\gamma_e(t,b)$ is the effective SNR calculated with the actual SINR, ϵ is the prediction noise. The predicted CQI $\widehat{Q}(t,\kappa)$ can be directly obtained from $\widehat{\gamma}_e(t,b)$ by Table 4.3. For a transmission with MCS corresponding to given $\widehat{Q}(t,\kappa)$, the data rate can be calculated by

$$F(t) = \sum_{\kappa\in\mathcal{K}} B\eta(\widehat{Q}(t,\kappa))P_0(\widehat{Q}(t,\kappa),\gamma_e(t,b)). \tag{4.86}$$

A smaller $\widehat{Q}(t,\kappa)$ leads to a smaller bandwidth efficiency $\eta(\widehat{Q}(t,\kappa))$ and a larger $\widehat{Q}(t,\kappa)$ leads to a dramatic increase of the BLER $P_e(\widehat{Q}(t,\kappa),\gamma_e(t,b))$. Therefore, in both cases, the overall throughput can be reduced.

To maximize the throughput, the prediction error in terms of mean squared error (MSE) should be minimized. However, the situation becomes more complicated when considering retransmissions. A transmission with overestimated CQIs leads to packet loss and thus to retransmissions. But, an occasional retransmission with higher order MCS could have better average throughput than constantly successful transmissions with lower order MCS. Moreover, in multi-user systems, the throughput depends not

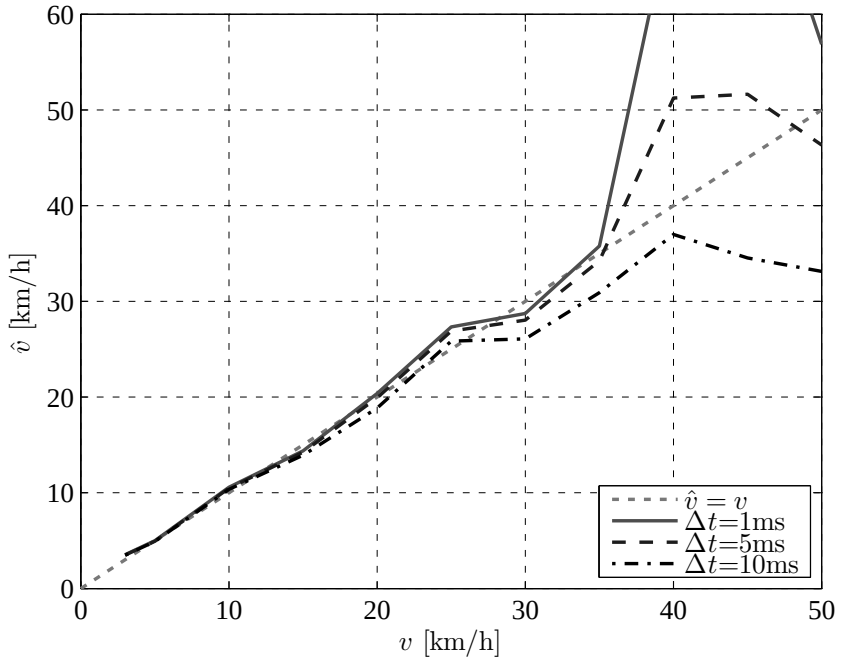

Figure 4.11: Estimated speed comparing to actual speed

only on the CQI feedback, but also on the scheduling algorithm. These issues will be elaborated with more details in Section 4.4.

4.3.2 Average bandwidth efficiency

To simplify the calculation of average bandwidth efficiency, consider a system with constant SINR and thus constant effective SNR. Due to the noisy prediction, the CQI ranges from 0 to 15 with a certain probability distribution. Since all the PRBs within a certain subband have the same CQI, both time and frequency indices are omitted in the calculation.

For an arbitrary PRB, according to Table 4.1, define the upper and lower bound of effective SNR for certain CQI $\widetilde{Q}$ as $\overline{\gamma}_{\mathrm{e}}(\widetilde{Q})$ and $\underline{\gamma}_{\mathrm{e}}(\widetilde{Q})$, respectively. The probability of transmitting with the MCS corresponding to CQI $\widetilde{Q}$ is given as

$$P(\widetilde{Q}) = \int_{\underline{\gamma}_{\mathrm{e}}(\widetilde{Q})}^{\overline{\gamma}_{\mathrm{e}}(\widetilde{Q})} p(\widehat{\gamma}_{\mathrm{e}}) \mathrm{d}\widehat{\gamma}_{\mathrm{e}}, \tag{4.87}$$

where $p(\widehat{\gamma}_{\mathrm{e}})$ is the pdf of the predicted effective SNR. And the bandwidth efficiency is calculated by

$$E = \sum_{\widetilde{Q}=1}^{15} P(\widetilde{Q}) \eta(\widetilde{Q}) P_0(\widetilde{Q}, \gamma_{\mathrm{e}}). \tag{4.88}$$

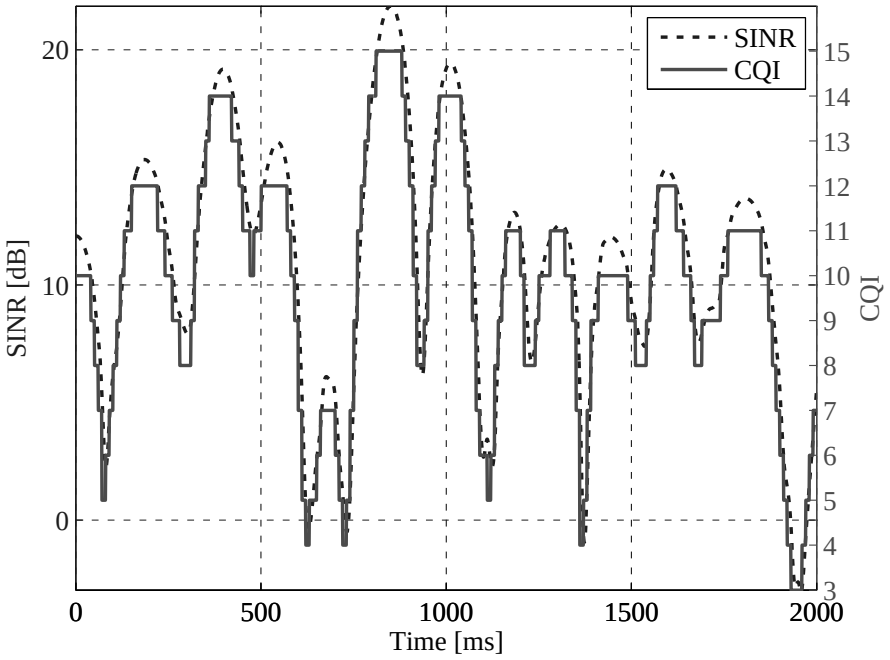

Figure 4.12: Temporal variation of SINR and CQI values

From this expression, it is clear that the bandwidth efficiency also depends on the distribution of the prediction noise.

4.3.3 Prediction schemes for CQI feedback

Since the frequency correlation and temporal correlation can be separated from each other, according to Chapter 2, the frequency domain PRB index κ is dropped here for convenience. The same procedure is done for each PRB.

The prediction of SINR is based on a collection of past observations, which is defined as the prediction window. An AR of prediction algorithms with a finite prediction window ϖ can be written as

$$\widehat{\gamma}(t + t_{\mathrm{d}}) = \sum_{\iota=0}^{\varpi} w_{\iota} \gamma(t - \iota T_{\mathrm{b}}), \tag{4.89}$$

where t_{d} is the feedback delay, ϖ is the prediction window size T_{b} is the duration of a PRB and w is the weighting factor. Without a prediction scheme, the eNB would directly perform AMC at time $t + t_{\mathrm{d}}$ based on the CQI derived from $\gamma(t)$.

Short-term average

The simplest prediction scheme is the short-term average scheme. By simply taking

$$w_{\iota,\mathrm{STA}} = \frac{1}{\varpi}, \tag{4.90}$$

the short-term average scheme is able to average out the fast oscillation and to preserve the trend of SINR variation [27].

The size of the prediction window is quite important for the short-term average. A window size, which is too small, is not enough to compensate for fast fading, whereas a window size, which is too large, ignores spatial variation.

Wiener filtering

Wiener filtering is known as the minimum mean squared error (MMSE) estimator for stationary process with known autocorrelation. The MSE of the predicted SINR is given by

$$\varepsilon = \mathrm{E}\left\{(\widehat{\gamma}(t+t_\mathrm{d}) - \gamma(t+t_\mathrm{d}))^2\right\}. \tag{4.91}$$

Expand this expression and substitute (4.89) in as follows

$$\varepsilon = \mathrm{E}\left\{\left(\sum_{\iota=0}^{\varpi} w_\iota \gamma(t-\iota T_\mathrm{b})\right)^2\right\} + \mathrm{E}\left\{\gamma(t+t_\mathrm{d})^2\right\} - 2\mathrm{E}\left\{\sum_{\iota=0}^{\varpi} w_\iota \gamma(t-\iota T_\mathrm{b})\cdot\gamma(t+t_\mathrm{d})\right\}. \tag{4.92}$$

Take the derivative with respect to the filter coefficient:

$$\frac{\partial\varepsilon}{\partial w_\iota} = 2\mathrm{E}\left\{\sum_{\iota=0}^{\varpi} w_\iota \gamma(t-\iota T_\mathrm{b}) \sum_{\nu=0}^{\varpi} \gamma(t-\nu T_\mathrm{b})\right\} - 2\mathrm{E}\left\{\sum_{\iota=0}^{\varpi} \gamma(t-\iota T_\mathrm{b})\gamma(t+t_\mathrm{d})\right\} \tag{4.93}$$

$$= 2\sum_{\iota=0}^{\varpi}\sum_{\nu=0}^{\varpi} \mathrm{E}\left\{\gamma(t-\iota T_\mathrm{b})\gamma(t-\nu T_\mathrm{b})\right\} w_\iota - 2\mathrm{E}\left\{\sum_{\iota=0}^{\varpi} \gamma(t-\iota T_\mathrm{b})\gamma(t+t_\mathrm{d})\right\}. \tag{4.94}$$

Letting this derivative be equal to 0 leads to

$$\sum_{\iota=0}^{\varpi}\sum_{\nu=0}^{\varpi} \mathrm{E}\left\{\gamma(t-\iota T_\mathrm{b})\gamma(t-\nu T_\mathrm{b})\right\} w_\iota = \sum_{\iota=0}^{\varpi} \mathrm{E}\left\{\gamma(t-\iota T_\mathrm{b})\gamma(t+t_\mathrm{d})\right\}. \tag{4.95}$$

For stationary process, the following holds true:

$$\mathrm{E}\left\{\gamma(t-\iota T_\mathrm{b})\gamma(t-\nu T_\mathrm{b})\right\} = R_{\gamma\gamma}\left((\iota-\nu)T_\mathrm{b}\right) \tag{4.96}$$

$$\mathrm{E}\left\{\gamma(t-\iota T_\mathrm{b})\gamma(t+t_\mathrm{d})\right\} = R_{\gamma\gamma}(\iota T_\mathrm{b} + t_\mathrm{d}). \tag{4.97}$$

Therefore, (4.95) can be written as

$$\sum_{\iota=0}^{\varpi}\sum_{\nu=0}^{\varpi} R_{\gamma\gamma}(\iota-\nu) w_\iota = \sum_{\iota=0}^{\varpi} R_{\gamma\gamma}(\iota T_\mathrm{b} + t_\mathrm{d}). \tag{4.98}$$

This equation written in matrix form yields

$$\mathbf{R}\mathbf{w} = \mathbf{r}, \tag{4.99}$$

where

$$\mathbf{R} = \begin{pmatrix} R_{\gamma\gamma}(0) & R_{\gamma\gamma}(T_\mathrm{b}) & \cdots & R_{\gamma\gamma}(\varpi) \\ R_{\gamma\gamma}(T_\mathrm{b}) & R_{\gamma\gamma}(0) & \cdots & R_{\gamma\gamma}(\varpi - T_\mathrm{b}) \\ \vdots & \vdots & \ddots & \vdots \\ R_{\gamma\gamma}(\varpi) & R_{\gamma\gamma}(\varpi - T_\mathrm{b}) & \cdots & R_{\gamma\gamma}(0) \end{pmatrix} \tag{4.100}$$

$$\mathbf{w} = (w_0, w_1, \cdots, w_\varpi)^\mathrm{T} \tag{4.101}$$

$$\mathbf{r} = (R_{\gamma\gamma}(t_\mathrm{d}), R_{\gamma\gamma}(t_\mathrm{d} + T_\mathrm{b}), \cdots, R_{\gamma\gamma}(t_\mathrm{d} + \varpi T_\mathrm{b}))^\mathrm{T}. \tag{4.102}$$

And the filter coefficients can be found by

$$\mathbf{w}_\mathrm{Wiener} = \mathbf{R}^{-1}\mathbf{r}. \tag{4.103}$$

Wiener filtering is quite often adopted for channel estimation algorithms. Generally speaking, if the autocorrelation is too low, the performance of Wiener filtering can be quite poor. Therefore, for very fast fading channels, Wiener filtering is barely used. However, from the results of last section, the spatial correlation plays an important role in SINR autocorrelation and prevents the autocorrelation function from going to zero. Hence, in SINR prediction, Wiener filter is a good choice. In addition, since the autocorrelation function is unknown, the sample autocorrelation can be used instead.

Extrapolation

Without assuming known statistics, extrapolation is a commonly used tool for forecasting missing values in time-series. Most commonly used extrapolation functions are linear extrapolation and cubic spline extrapolation. In this thesis, cubic spline extrapolation is considered.

Cubic spline functions are piecewise defined polynomials of degree three of the form

$$\widehat{\gamma}(t) = \begin{cases} \widetilde{\gamma}_1(t) & \text{if } t_1 \le t < t_2, \\ \widetilde{\gamma}_2(t) & \text{if } t_2 \le t < t_3, \\ & \vdots \\ \widetilde{\gamma}_N(t) & \text{if } t_N \le t < t_{N+1}, \end{cases} \tag{4.104}$$

where

$$\widetilde{\gamma}_n(t) = c_3(t - t_n)^3 + c_2(t - t_n)^2 + c_1(t - t_n) + c_0. \tag{4.105}$$

Assuming the spline function and its first and second derivatives are continuous in the interval $[t_1, t_{N+1}]$, the unknown coefficients can be solved, with the natural boundary conditions $\widehat{\gamma}''(t_1) = \widehat{\gamma}''(t_{N+1}) = 0$ [14].

Spline extrapolation does not need statistics as a priori information and provides an almost perfect prediction for users with low velocity, as shown in Figure 4.13 (a). However, if the user moves faster, the boundary condition of $\widehat{\gamma}''(t_{N+1}) = 0$ can lead to severe numerical problem, as shown in Figure 4.13 (b) and (c). The numerical errors can be reduced by introducing additional boundary conditions.

Noticing that the probability of having large difference of CQI between two adjacent PRBs

$$\Delta Q(t) = Q(t) - Q(t - T_\mathrm{b}) \tag{4.106}$$

is quite small, as shown in Table 4.5, an artificial restriction

$$\left|\widehat{Q}(t + t_\mathrm{d}) - \widehat{Q}(t + t_\mathrm{d} - T_\mathrm{b})\right| \leq \Delta Q_{\max} \tag{4.107}$$

can be applied to the extrapolation. Using the relationship of SINR and CQI in Figure 4.5, corresponding $\Delta\gamma_{\max}$ can be calculated. As shown in Figure 4.13 (d), using this addition restriction, the numerical problem can be reduced. But, extrapolation still has no advantage over other prediction methods for users with moving speed higher than 30 km/h.

Adaptive prediction scheme

Since extrapolation is very effective for low speed, and Wiener filtering is effective for medium to high speed, an adaptive method can be derived by choosing a proper prediction scheme for certain speed. With the help of the approximated autocovariance function, the adaptive prediction scheme can be easily defined as using extrapolation for users with speed lower than 30 km/h and Wiener filtering for users with speed equal to or higher than 30 km/h.

Speed [km/h]	$p(\Delta Q > 1)$	$p(\Delta Q > 2)$
3	9.97×10^{-5}	8.37×10^{-7}
10	1.37×10^{-4}	2.51×10^{-6}
30	7.82×10^{-3}	3.88×10^{-4}
50	4.52×10^{-2}	4.68×10^{-3}

Table 4.5: Statistics of differences between neighboring CQI

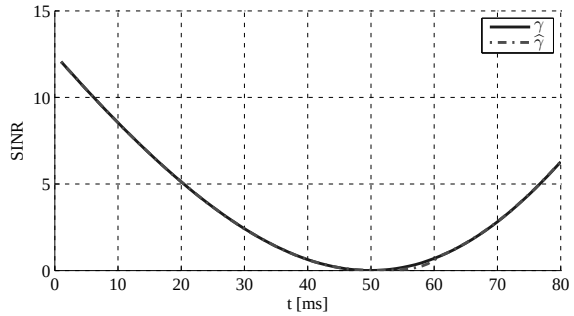

(a)

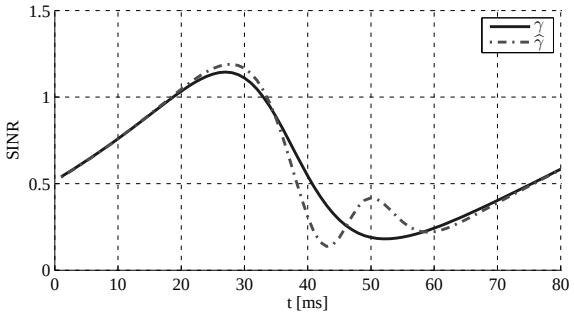

(b)

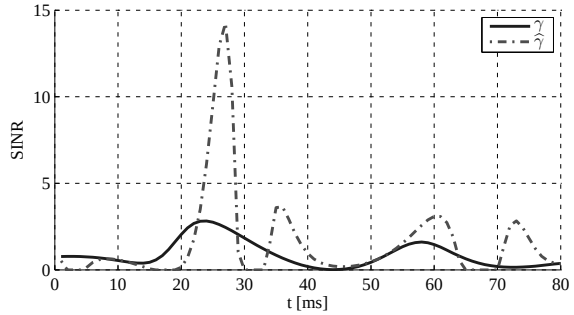

(c)

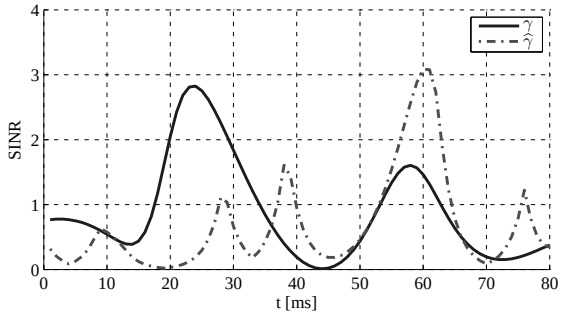

(d)

Figure 4.13: (a) (b) (c): Simulated SINR curves for UE at 3 km/h, 10 km/h, 30 km/h, respectively. (d): at 30 km/h with additional boundary conditions $\Delta Q_{\max} = 1$, feedback delay is $t_{\mathrm{d}} = 10$ ms

Other prediction schemes

Several other CQI prediction schemes have been suggested from a number of publications. For example, a normalized least mean square (NLMS) scheme is proposed in [84], a first order adaptive infinite impulse response (IIR) filter is implemented in [25]. However, during our research, these schemes result in rather poor performance. The main reason is, that mostly a very small feedback delay of 1 ms is considered, and the performance of these algorithms drop significantly if the feedback delay becomes larger. For a real system, the feedback delay can be as high as 10 ms [35]. In this work, a worst case scenario is considered, where the feedback delay is fixed to 10 ms.

4.3.4 Numerical results

The same parameter setting as in Section 4.2 is used for numerical evaluation. A single user system is considered to isolate the influence of CQI prediction to the throughput.

In Figure 4.14, the MSE of CQI prediction is plotted. It can be seen that for very low speed, the extrapolation scheme offers extremely accurate prediction. However, when the speed becomes higher, the accuracy of the extrapolation scheme decreases drastically. In contrast, for very low speed, using short-term average is even worse than not using any prediction at all. But for higher speed, the short-term average scheme provides a significantly better accuracy than using no prediction. The only schemes which have advantage over no prediction in both low speed and high speed are Wiener filtering and the adaptive prediction scheme. Especially for the adaptive prediction scheme, due to the accurate estimation of moving speed using the approximated autocovariance function, the performance is almost perfect matches with extrapolation for low speed and Wiener filtering for higher speed.

An interesting phenomenon is that the MSE is not monotonically increasing as the speed gets higher. A possible explanation is that for users moving with higher speed, spatial correlation plays a more important role in the autocorrelation function. As shown in Figure 4.16, for the same Δ, the correlation of the SINR is not necessarily a monotonic function of speed.

The throughput performance is shown in Figure 4.15. The throughput result is almost consistent with the MSE result. For lower speed users, due to the accurate CQI prediction, the throughput is higher. The extrapolation scheme provides the best throughput for low speed users, whereas Wiener filtering offers the best throughput for high speed users. The adaptive prediction scheme provides the best overall performance. Throughout the whole speed range, using a proper CQI prediction scheme can boost the throughput by a factor of $10\% - 25\%$.

4.3.5 Prediction noise and Gaussian approximation

Although the probability of transmitting with certain MCS is given in (4.87), without a known distribution of the prediction error, the calculation of bandwidth efficiency

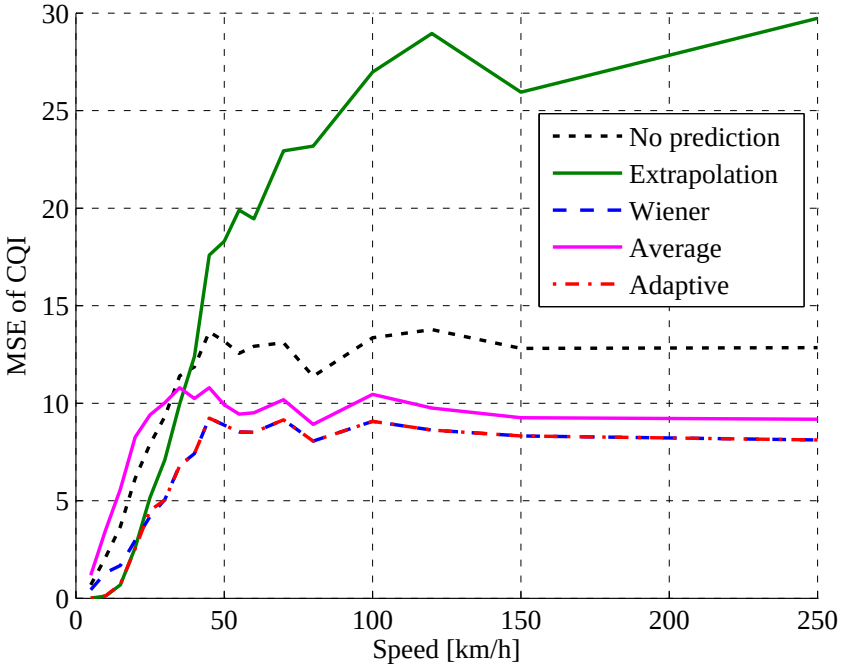

Figure 4.14: MSE of predicted CQI value for single user

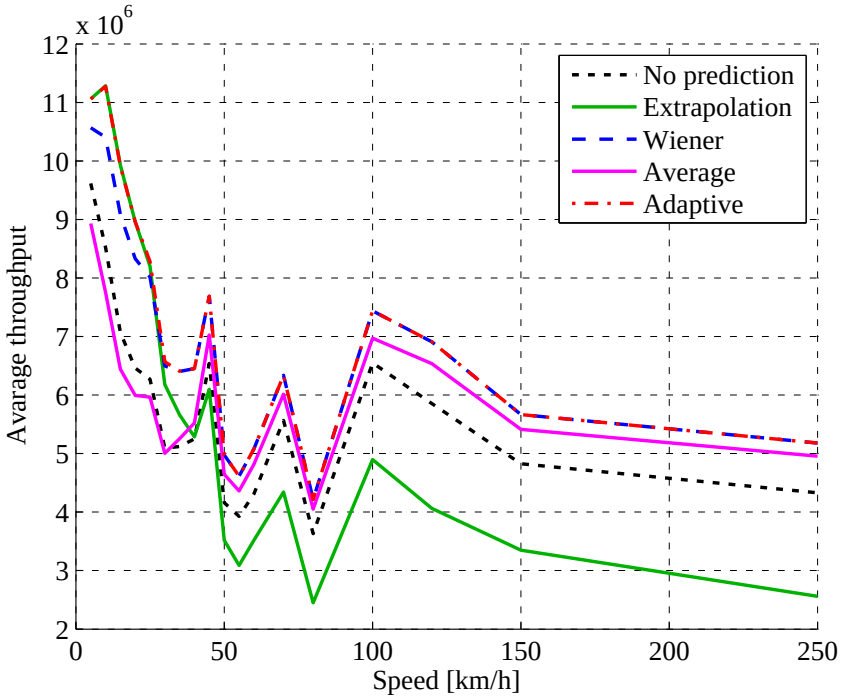

Figure 4.15: Average throughput for single user

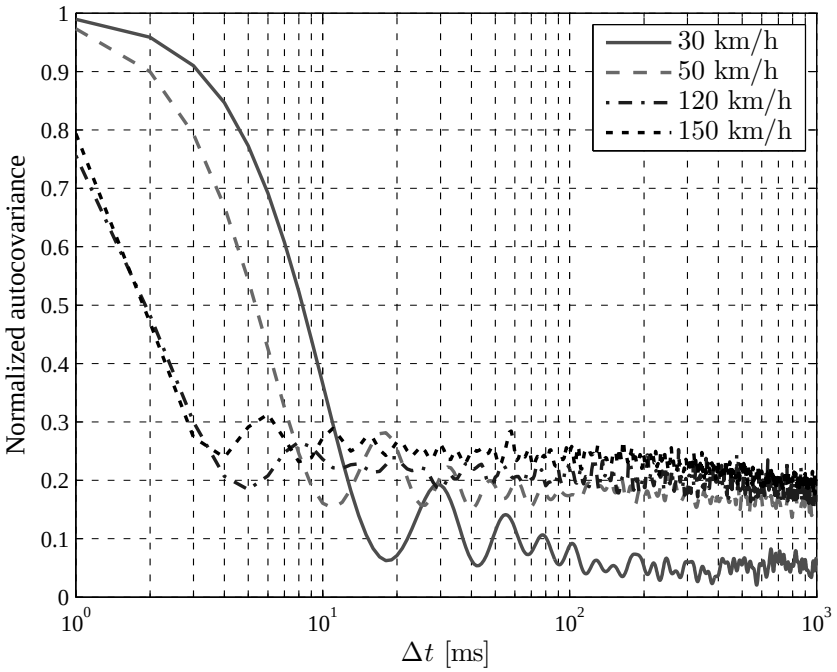

Figure 4.16: Measured autocovariance function for UEs moving of different speeds

cannot be done. As a matter of fact, the distribution of the prediction error in dB scale is quite close to a Gaussian distribution as shown in Figure 4.17, where the Gaussian pdfs have the same mean value and variance as the prediction error obtained from simulation. Therefore, the prediction noise can be approximated by an Gaussian distributed random variable as

$$p(\epsilon) \approx \frac{1}{\sqrt{2\pi\sigma_\epsilon^2}} \exp\left\{-\frac{(\epsilon-\mu_\epsilon)^2}{2\sigma_\epsilon^2}\right\} \tag{4.108}$$

where μ_ϵ and σ_ϵ^2 are the mean value and variance of the prediction error, respectively. Accordingly, the predicted effective SNR can be written as

$$p(\widehat{\gamma}_\mathrm{e}) = \frac{1}{\sqrt{2\pi\sigma_\epsilon^2}} \exp\left\{-\frac{\left(\widehat{\gamma}_\mathrm{e}-\mu_\epsilon-\gamma_\mathrm{e}\right)^2}{2\sigma_\epsilon^2}\right\} \tag{4.109}$$

Using the Gaussian approximation, (4.87) becomes

$$P\left(\widetilde{Q}\right) = \int_{\underline{\gamma}_\mathrm{e}\left(\widetilde{Q}\right)}^{\overline{\gamma}_\mathrm{e}\left(\widetilde{Q}\right)} \frac{1}{\sqrt{2\pi\sigma_\epsilon^2}} \exp\left\{-\frac{(\widehat{\gamma}_\mathrm{e}-\mu_\epsilon-\gamma_\mathrm{e})^2}{2\sigma_\epsilon^2}\right\} \mathrm{d}\widehat{\gamma}_\mathrm{e} \tag{4.110}$$

$$= \frac{1}{2}\left(\mathrm{erf}\left(\frac{\overline{\gamma}_\mathrm{e}\left(\widetilde{Q}\right)-\mu_\epsilon-\gamma_\mathrm{e}}{\sqrt{2\sigma_\epsilon^2}}\right) - \mathrm{erf}\left(\frac{\underline{\gamma}_\mathrm{e}\left(\widetilde{Q}\right)-\mu_\epsilon-\gamma_\mathrm{e}}{\sqrt{2\sigma_\epsilon^2}}\right)\right), \tag{4.111}$$

where $\mathrm{erf}(\cdot)$ is the error function defined as

$$\mathrm{erf}(x) = \frac{2}{\sqrt{\pi}} \int_0^x \exp(-t^2)\mathrm{d}t. \tag{4.112}$$

With (4.111), the bandwidth efficiency can be calculated with (4.88), as shown in Figure 4.19. Clearly, for an unbiased estimator, as the noise variance increases, the bandwidth efficiency decreases.

Moreover, although the calculation of bandwidth efficiency assumes a static channel, the average throughput of a moving user can be easily calculated by multiplying the number of PRBs, the bandwidth of a PRB and the average bandwidth efficiency. The Gaussian approximation is validated with the average throughput for moving users. The average throughput in Figure 4.18 is calculated using the Gaussian approximation, with μ_ϵ and σ_ϵ^2 extracted from the simulation results using the aforementioned prediction schemes. Comparing to Figure 4.15, the difference is smaller than 1 Mbit/s. Therefore, the Gaussian approximation is an accurate approximation.

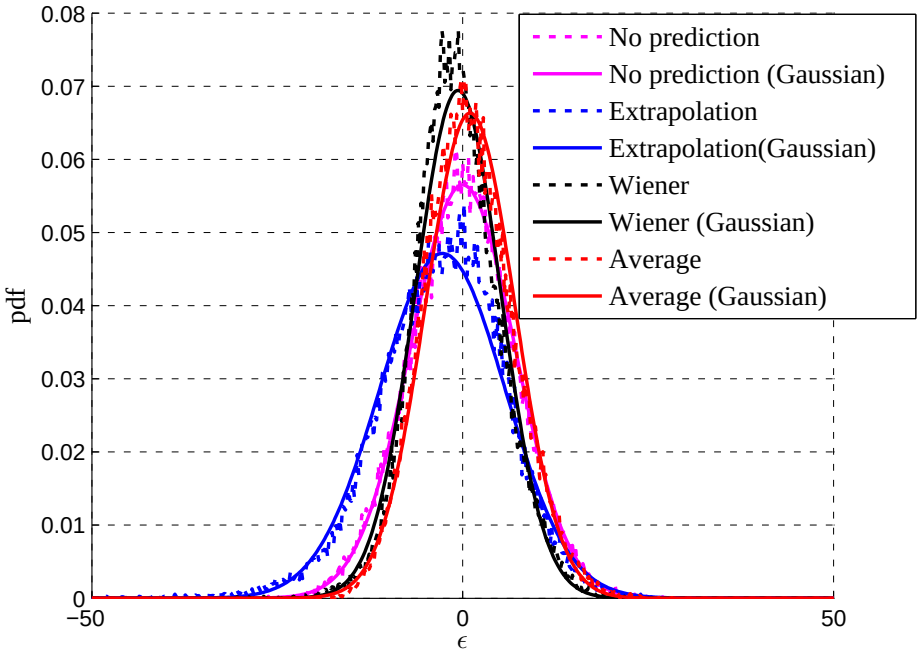

Figure 4.17: Measured error distribution and Gaussian approximation at 50 km/h

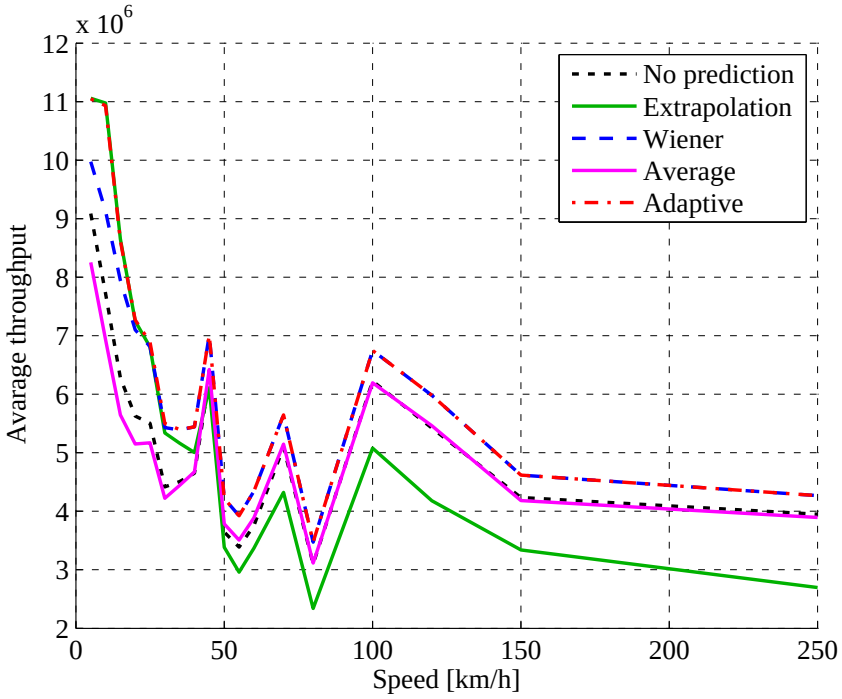

Figure 4.18: Average throughput for single user using Gaussian approximation

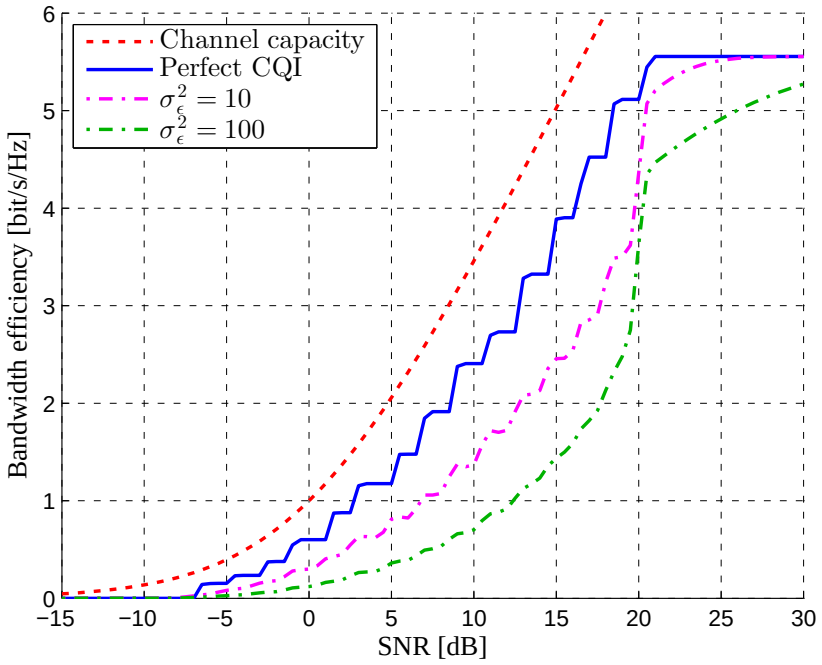

Figure 4.19: Bandwidth efficiency for LTE with Gaussian distributed prediction noise

4.4 Channel prediction in the presence of HARQ

Due to the mismatch of real time channel conditions and the information at the eNB, downlink transmissions are not always successful. In case of a failed transmission, the HARQ mechanism is triggered.

4.4.1 HARQ basics

HARQ is a hybrid combination of forward error correction (FEC) and automatic repeat request (ARQ). In the LTE protocol stack, HARQ works at the physical layer (PHY) layer but is controlled by the MAC layer. If a CRC error is detected at the UE, a negative acknowledgment (NACK) signal is send back to the eNB to evoke the HARQ process.

HARQ types

There are three types of HARQ: Type I, Type II and Type III [37].

Type I HARQ is the simplest HARQ scheme, where both error detection and FEC information are attached to the data. If the channel quality is sufficiently good, the transmission errors can be corrected using parity bits and an acknowledgment (ACK) signal is sent back. Otherwise, the receiver discards this package, sends a NACK signal

and the same package is retransmitted. Comparing to ARQ, which always asks for retransmission whenever there are erroneous bits detected, Type I HARQ can improve the efficiency if the errors are correctable. However, if the channel is very good, the large number of redundancy bits reduce the bandwidth efficiency. On the other hand, if the channel condition is very poor, the FEC may not be powerful enough and thus many retransmissions are needed.

In Type II HARQ, the first transmission may carry only data and error detection bits. In case of erroneous transmission, the original package is not discarded. The parity bits are sent to combine with the data bits and to correct the errors. Consider the fact that FEC bits are generally much more than error detection bits, Type II HARQ can offer better efficiency in a good channel condition [24].

Type III HARQ decreases the coding rate by sending additional redundancy bits in each retransmission. It ensures that each retransmission is self-decodable. The decoder can combine these multiple copies weighted by the SNR of the received signal for each retransmission. Therefore, time domain diversity is exploited.

Soft combining

In Type II and III HARQ, the original and retransmitted packages are combined to improve the decoder performance. There are two main soft combining methods in HARQ, namely, chase combining (CC) and incremental redundancy (IR).

In CC, every retransmission carries the same data and parity bits as the original transmission. Maximum-ratio combining is used to combine different copies of the same bits. Since all the transmission are identical, CC can be treated as an additional repetition coding.

In IR, each retransmission consists of new redundancy bits from the channel encoder. The sets of coded bits are generated by puncturing. The combination effectively gives a lower coding rate and thus provide better error performance. It has been shown that in mobile cellular networks, IR almost always outperforms CC, at the cost of increased complexity [32] [16].

Transmission protocol

The performance of HARQ is limited by buffering capability. Three different transmission protocols are commonly used: stop-and-wait, go-back-N and selective repeat.

The stop-and-wait protocol is the simplest one. After sending a package, the transmitter remains idle, before it receives an ACK or NACK signal from the receiver. The stop-and-wait protocol has a small signaling overhead as well as buffer requirement. However, some radio resources are wasted on waiting for the response signal. This problem becomes more severe, when propagation delay is long.

To improve efficiency, go-back-N protocol is proposed. In go-back-N, the transmitter keeps sending packages until it receives a NACK message. When a NACK signal is

received, the transmitter has to resend the last "N" packages including the erroneous one. Clearly, an index number of the package has to be composed into the ACK/NACK signals. Moreover, more buffer capacity is required on the receiver side.

The selective repeat protocol is similar to go-back-N, except only the erroneous package is retransmitted. Therefore, the bandwidth efficiency can be improved. However, it is difficult to arrange packages in the desired order without a complex buffering scheme.

4.4.2 HARQ in LTE

In LTE, an IR HARQ with a 1/3 turbo encoder is used for FEC. The transport block CRC is used for error detection. The receiver only receives different punctured versions of the same turbo-encoded data, each of these retransmissions are self-decodable. Thus, it a Type III HARQ.

For the transmission protocol, LTE adopts a variant of the stop-and-wait protocol, the N-channel stop-and-wait [51]. There are "N" channels capable of buffering and retransmitting packages. When a channel is waiting for acknowledgement, the next one starts to transmit. Therefore, no bandwidth is wasted on waiting for acknowledgement; the ACK/NACK signal needs only a single bit; and the implementation is still simple.

Since in IR HARQ, different punctured versions of the turbo-encoded data are combined, an improvement of the BLER is expected. Figure 4.20 shows the effective SNR gains of 3 retransmissions, with the same BLER constraint. In [41], the effective SNR gain is approximated by

$$\Delta\gamma_{r_{\mathrm{re}}} = \mu_{\mathrm{mod}}(r_{\mathrm{re}})R_{\mathrm{turbo}} + \varepsilon_{\mathrm{mod}}(r_{\mathrm{re}}) \tag{4.113}$$

where r_{re} is the retransmission index, μ_{mod} and $\varepsilon_{\mathrm{mod}}$ are modulation related parameters. R_{turbo} listed in Table 4.6. The turbo code rate R_{turbo} corresponds to each CQI can be found in Table 4.1.

Modulation	r_{re}	R_{turbo}	$\varepsilon_{\mathrm{mod}}$
4-QAM	1	0.0804	2.89
	2	0.1628	4.57
	3	0.2006	5.62
16-QAM	1	0.0420	1.17
	2	0.8435	0.74
	3	0.9464	1.15
64-QAM	1	0.8996	-1.23
	2	1.2288	-0.71
	3	1.2728	0.15

Table 4.6: HARQ model parameters for LTE

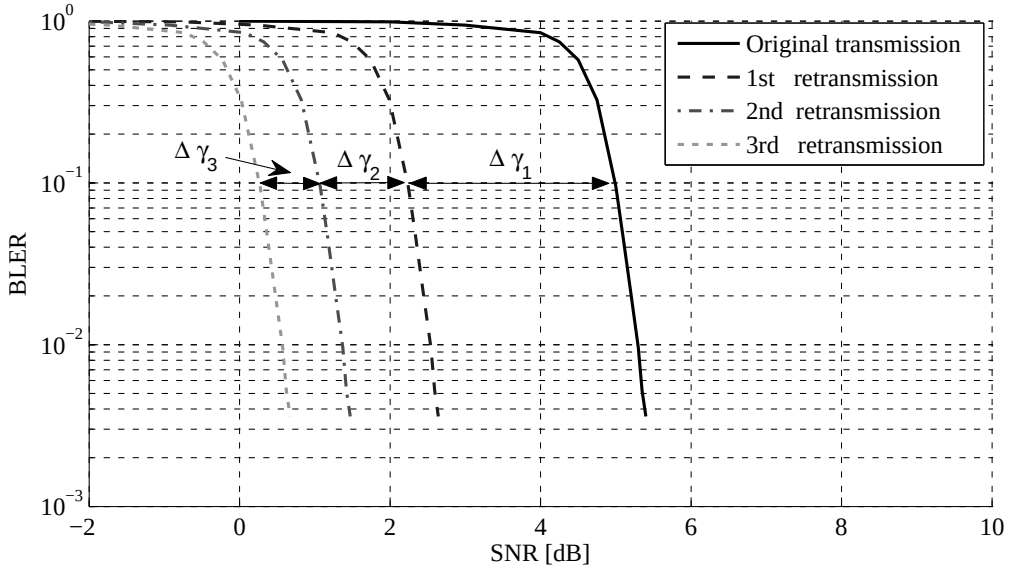

Figure 4.20: SNR gain due to HARQ retransmission at 10% BLER point for CQI 7

4.4.3 CQI feedback with different QoS constraints

With HARQ, another QoS constraint of latency shall be investigated. If the original transmission fails, there is a period before the lost packet can be detected and retransmitted. Therefore, the overall latency is directly associated with the frequency of retransmission.

Buffering

In the retransmission, the MCS of the packet is the same as the original one, to make the decoder work properly. Hence, after receiving an NACK signal, the eNB has to schedule a PRB with sufficiently good channel quality for retransmitting the lost packet. Two different buffering schemes are considered here.

The first scheme is referred as unlimited buffering. In his case, all the lost packets are queued in the buffer in chronological order. Whenever a new PRB is available, the predicted CQI of this PRB is compared with the corresponding CQI of the queueing packet sequentially. The first packet with a CQI smaller than or equal to the predicted CQI will be transmitted using this PRB. Only if all the packets in the buffer require better channel quality, a new packet is transmitted. Unlimited buffering provides the best effort to eventually get all the packets transferred. However, if there are many queued packets, new packets potentially have to wait a long time before a PRB is available. Therefore, unlimited buffering is a proper strategy for delay tolerant applications. In practice, if the buffer is large enough so that no overflow will happen, it can be considered as unlimited buffering.

The other option is limited buffering, where the only difference is the number of packets in the queue is bounded by a buffer size. Older packets are discarded, if the buffer is full. This buffering scheme is more suitable for realtime applications, e.g., voice over Internet protocol (VoIP), where the latency is more critical and the outdated packets are useless.

Throughput and approximated bandwidth efficiency

Consider the first transmission of a certain PRB at time t_0, the probability of a successful transmission is $P_0(Q(t_0,\kappa),\gamma_{\mathrm{e}}(t_0,b))$. Therefore, the probability of the first retransmission is $1-P_0(Q(t_0,\kappa),\gamma_{\mathrm{e}}(t_0,b))$. Moreover, since the MCS used for the retransmission is the same as the original transmission, the probability that the retransmission is successful at $t_{r_{\mathrm{re}}}$, is determined by the channel condition at $t_{r_{\mathrm{re}}}$ and the effective SNR gain.

Define the success rate of retransmission r_{re} as

$$P_{r_{\mathrm{re}}}\left(\widehat{Q}(t_0,\kappa),\gamma_{\mathrm{e}}(t_{r_{\mathrm{re}}},b)\right)=1-P_{\mathrm{e}}\left(\widehat{Q}(t_0,\kappa),\gamma_{\mathrm{e}}(t_{r_{\mathrm{re}}},b)+\Delta\gamma_{r_{\mathrm{re}}}\right), \tag{4.114}$$

for PRB κ with the r_{re}-th retransmission, the average throughput at $t_{r_{\mathrm{re}}}$ is written as

$$F(t_{r_{\mathrm{re}}},\kappa)=B\eta\left(\widehat{Q}(t,\kappa)\right)P_{r_{\mathrm{re}}}\left(\widehat{Q}(t_0,\kappa),\gamma_{\mathrm{e}}(t_{r_{\mathrm{re}}},b)\right). \tag{4.115}$$

Furthermore, in this case, since $r_{\mathrm{re}}+1$ time slots are used for successful delivery of one PRB, one time slot only carries $\frac{1}{r_{\mathrm{re}}+1}$ of a PRB on average. On the one hand, with a fixed MCS, as the number of retransmission grows, the average throughput decreases. On the other hand, the retransmissions also provide an effective SNR gain, and thus enable successful transmission with higher order MCS. If the PRB with higher order MCS can be successfully transmitted, the throughput can be potentially increased.

To find out the impact of HARQ on the average bandwidth efficiency, consider a system with constant SINR. In addition, it is assumed that the maximum number of retransmissions is 3.

For a given prediction of CQI $\widehat{Q}$, the calculation of average bandwidth efficiency requires three building blocks, namely, the probability to have r_{re}-th retransmission, the probability that the original transmission or the r_{re}-th retransmission is successful and the bandwidth efficiency for the successful transmissions. Hence, the average bandwidth efficiency is given by:

$$\begin{aligned}E=&\eta(\widehat{Q})P_0(\widehat{Q},\gamma_{\mathrm{e}})+\frac{1}{2}\eta(\widehat{Q})\left(1-P_0(\widehat{Q},\gamma_{\mathrm{e}})\right)P_1(\widehat{Q},\gamma_{\mathrm{e}})\\&+\frac{1}{3}\eta(\widehat{Q})\left(1-P_0(\widehat{Q},\gamma_{\mathrm{e}})\right)\left(1-P_1(\widehat{Q},\gamma_{\mathrm{e}})\right)P_2(\widehat{Q},\gamma_{\mathrm{e}})\\&+\frac{1}{4}\eta(\widehat{Q})\left(1-P_0(\widehat{Q},\gamma_{\mathrm{e}})\right)\left(1-P_1(\widehat{Q},\gamma_{\mathrm{e}})\right)\left(1-P_2(\widehat{Q},\gamma_{\mathrm{e}})\right)P_3(\widehat{Q}.\gamma_{\mathrm{e}}).\end{aligned} \tag{4.116}$$

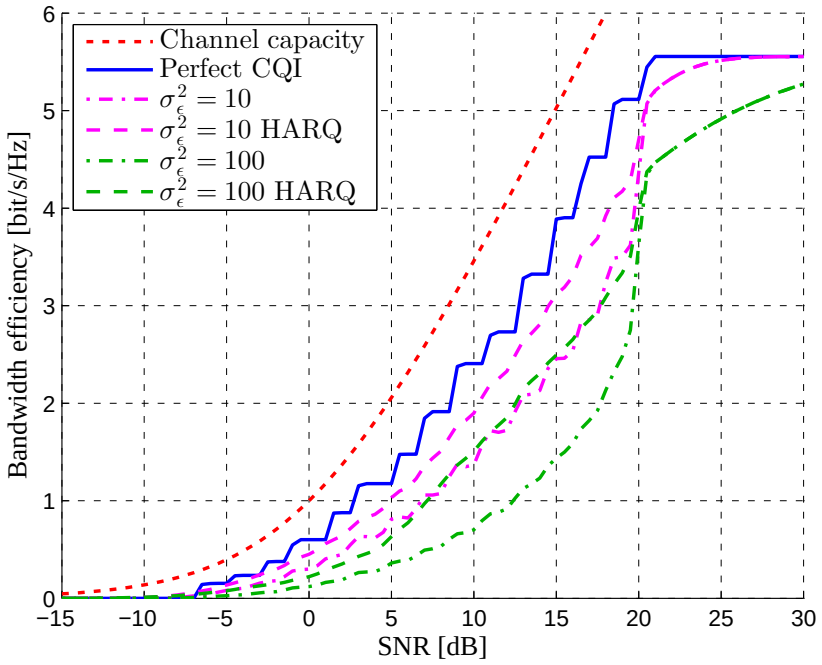

Figure 4.21: Bandwidth efficiency for LTE with Gaussian distributed prediction noise and HARQ

The prediction noise is again modeled as a Gaussian distributed random variable. Since the distribution of prediction noise depends on the moving speed, for user travelling at a constant speed, the noise distribution is assumed to be static. Finally, the average bandwidth efficiency is given as

$$\begin{aligned} E = \sum_{\widetilde{Q}=1}^{15} P(\widetilde{Q}) \Big(& \eta(\widetilde{Q}) P_0(\widetilde{Q}, \gamma_e) + \frac{1}{2}\eta(\widetilde{Q}) \left(1 - P_0(\widetilde{Q}, \gamma_e)\right) P_1(\widetilde{Q}, \gamma_e) \\ & + \frac{1}{3}\eta(\widetilde{Q}) \left(1 - P_0(\widetilde{Q}, \gamma_e)\right) \left(1 - P_1(\widetilde{Q}, \gamma_e)\right) P_2(\widetilde{Q}, \gamma_e) \\ & + \frac{1}{4}\eta(\widetilde{Q}) \left(1 - P_0(\widetilde{Q}, \gamma_e)\right) \left(1 - P_1(\widetilde{Q}, \gamma_e)\right) \left(1 - P_2(\widetilde{Q}, \gamma_e)\right) P_3(\widetilde{Q}.\gamma_e) \Big), \end{aligned} \quad (4.117)$$

where $P(\widetilde{Q})$ can be calculated from (4.111).

Clearly, the calculation above is for the case of unlimited buffering, since a drop of packet without 3 retransmission attempts is not considered.

Comparing (4.117) and (4.88), it is easy to notice that, with the same prediction noise, the average bandwidth efficiency of a system with HARQ is higher than without HARQ.

Overestimation and underestimation

It can be seen from (4.111), that the probability of having a certain predicted CQI value does not only depend on the variance of the prediction noise but also on the mean value. The estimation of future CQI is not always unbiased. During the investigation, several predictors show a biased behavior. That is, the mean value of the prediction noise $\mu_\epsilon \neq 0$. Therefore, μ_ϵ also has an influence on the bandwidth efficiency.

For $\mu_\epsilon > 0$, the predictor tends to overestimate the effective SNR. Therefore, higher order MCS has a bigger chance to be used. In this case, the probability of retransmission is higher. At the same time, for each successful transmission, the data rate is potentially higher.

For $\mu_\epsilon < 0$, the predictor tends to underestimate the effective SNR. In this case, lower order MCS is more probable to be used and the error probability is potentially lower. Therefore, the latency is smaller.

As shown in Figure 4.22, for a biased predictor with $\mu_\epsilon = 1$, the bandwidth efficiency is better than for an unbiased predictor for all SNR value. However, this trick is not universal, if μ_ϵ is increased to 10, the bandwidth efficiency for smaller SNR becomes lower. Because higher order MCSs are almost always used, and thus causing a very high BLER for channels with low SNR values. In contrast, for $\mu_\epsilon < 0$, the bandwidth efficiency is always lower than the unbiased predictor.

The impact μ_ϵ on biased prediction is also associated with σ_ϵ^2. For a small σ_ϵ^2, the prediction is accurate, and the average bandwidth efficiency is close to the limit. In this case, a biased predictor is less effective. As shown in Figure 4.23, with $\sigma_\epsilon^2 = 10$, the predictor with $\mu_\epsilon = 1$ can still provide slight improvement. But $\mu_\epsilon = 10$ is already much worse than the unbiased one.

4.4.4 Numerical results

The throughput of systems with HARQ is shown in Figure 4.26 and Figure 4.27 for unlimited buffering and limited buffering, respectively. For limited buffering, the buffer size is 6 PRBs. The throughput for unlimited buffering is higher than for limited buffering as expected. In addition, the overall success rate of unlimited buffering is close to 100 % for most of the prediction methods, as shown in Figure 4.25.

Although a larger buffer size offers advantages for throughput and overall success rate, the latency is also longer. As shown in Figure 4.24, a smaller buffer size has significantly smaller average latency.

As a conclusion, a smaller buffer size should be applied to latency sensitive applications, whereas a larger buffer size can provide higher throughput.

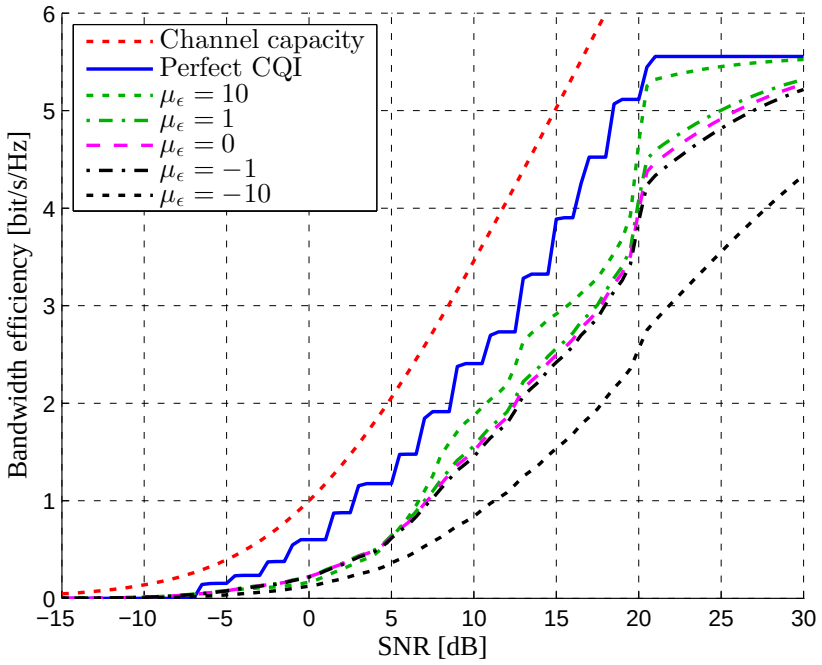

Figure 4.22: Bandwidth efficiency with biased predictor, $\sigma_\epsilon^2 = 100$

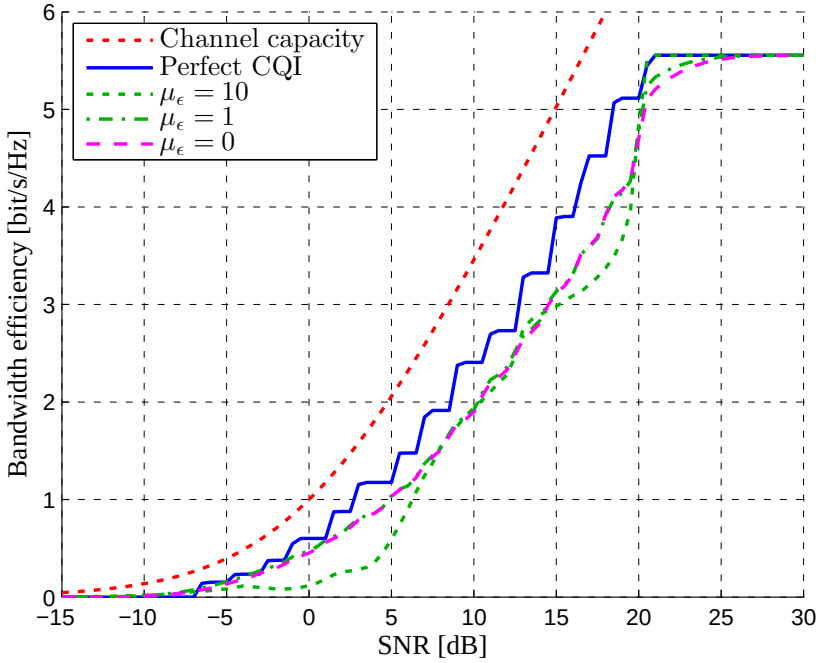

Figure 4.23: Bandwidth efficiency with biased predictor, $\sigma_\epsilon^2 = 10$

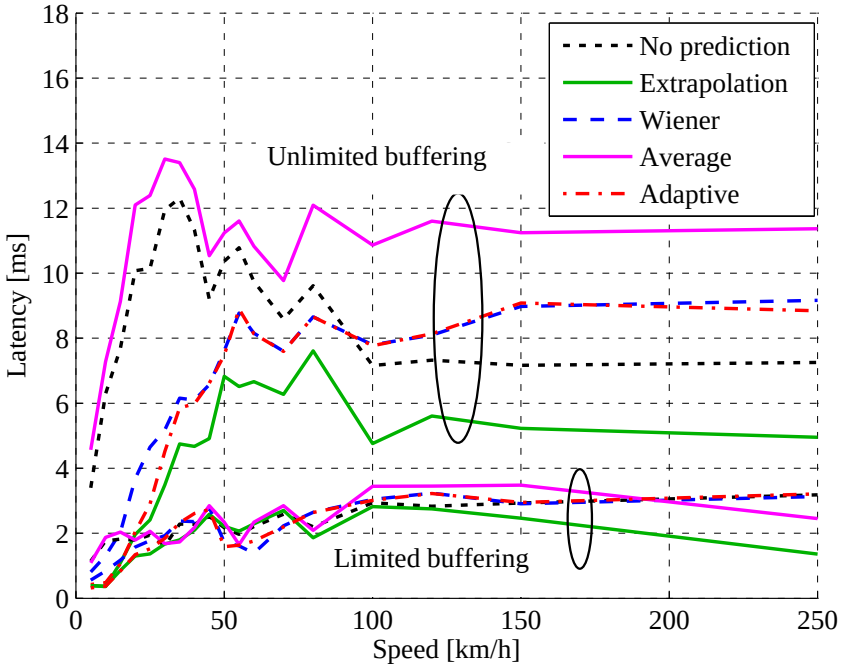

Figure 4.24: Latency for single user with HARQ

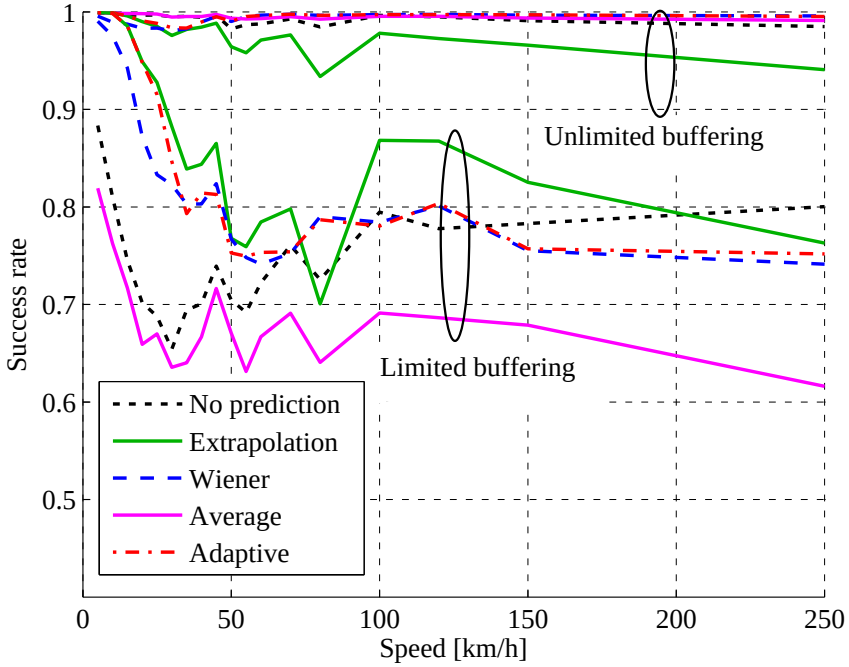

Figure 4.25: Success rate for single user with HARQ

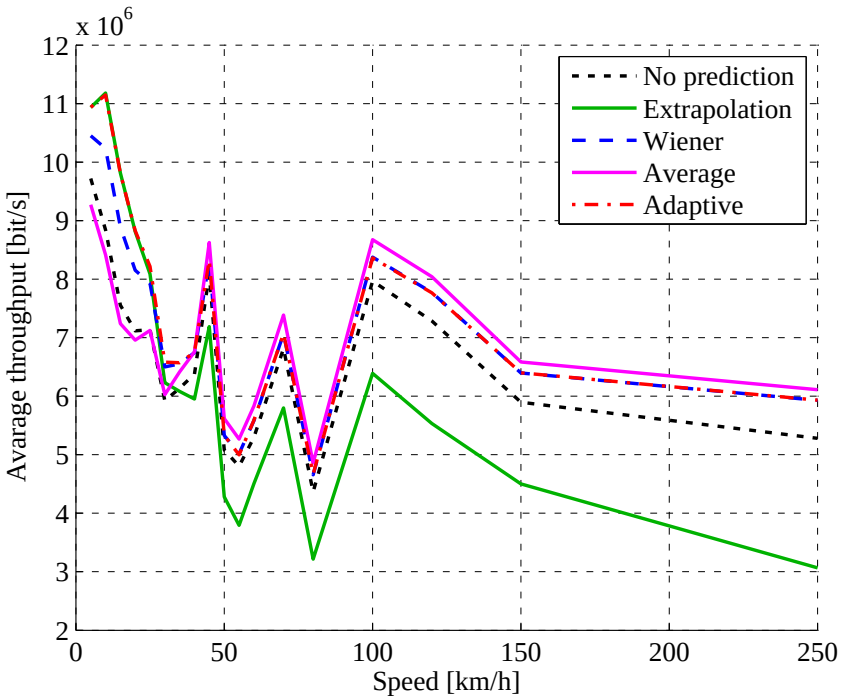

Figure 4.26: Average throughput for single UE with HARQ, unlimited buffer

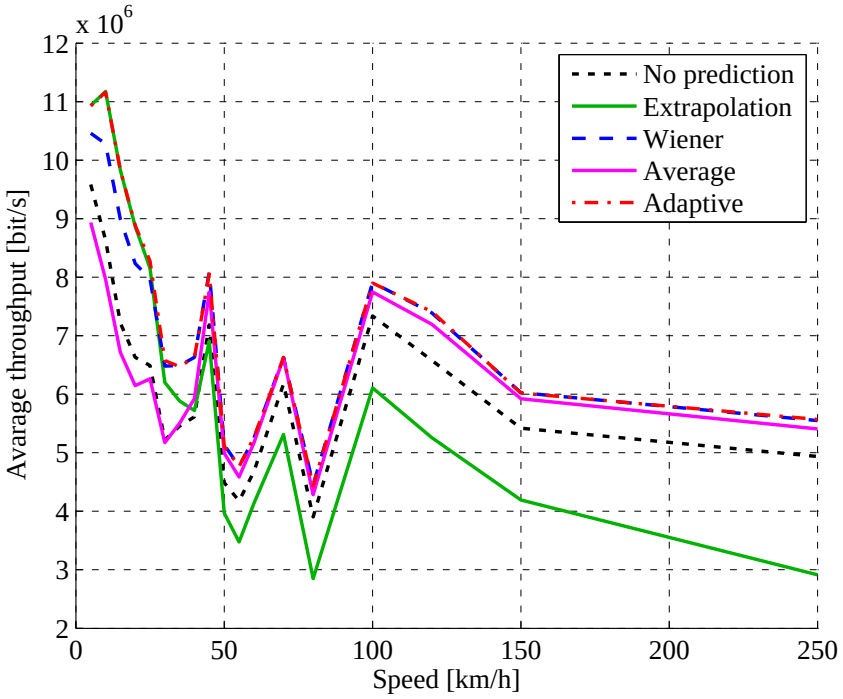

Figure 4.27: Average throughput for single UE with HARQ, limited buffer

4.5 Multi-user system

The main purpose of using multi-user system in this thesis is to evaluate the performance of CQI prediction schemes in such environment. In current LTE standards, subcarrier level power allocation is still unavailable. Therefore, the Tx power on different PRBs are equally distributed. The resource allocation problem is simplified to PRB assignment based on CQI. Due to the extent of this thesis, this part only gives an example of using CQI as the input of scheduling algorithm, without discussing optimality.

4.5.1 Multi-user resource allocation

Apart from providing high total transmission data rates in the downlink, the scheduler also considers the data rate fairness among UEs in order to assure an ideal environment to evaluate the effect of prediction schemes on system throughput. For this purpose, CQI values are derived to a priority metric using proportional fair (PF) scheduling algorithm [49].

In LTE, the physical resources are reassigned for each transmission time interval (TTI). For a system with N_{UE} UEs and N_{PRB} PRBs, during a TTI, a priority metric matrix

$$\mathbf{M}(t) = \begin{pmatrix} M_{1,1}(t) & M_{1,2}(t) & \cdots & M_{1,N_{\mathrm{UE}}}(t) \\ M_{2,1}(t) & M_{2,2}(t) & \cdots & M_{2,N_{\mathrm{UE}}}(t) \\ \vdots & \vdots & \ddots & \vdots \\ M_{N_{\mathrm{PRB}},1}(t) & M_{N_{\mathrm{PRB}},2}(t) & \cdots & M_{N_{\mathrm{PRB}},N_{\mathrm{UE}}}(t) \end{pmatrix} \tag{4.118}$$

is produced at each eNB. Its entry $M_{\kappa,i}(t)$ is given as:

$$M_{\kappa,i}(t) = \frac{\widehat{F}_{\kappa,i}(t)}{\overline{F}_i(t)} \tag{4.119}$$

where κ is the index of PRB, $\widehat{F}_{\kappa,i}(t)$ is the expected throughput, which is the instantaneous supportable data rate at time t and can be derived from the current CQI reported at eNB. $\overline{F}_i(t)$ is the past average throughput of UE i till time t, which is given by [46]:

$$\overline{F}_i(t) = (1-\alpha)\overline{F}_i(t - T_{\mathrm{b}}) + \sum_{\kappa \in \mathcal{K}_i} \alpha F_{\kappa,i}(t - T_{\mathrm{b}}), \tag{4.120}$$

where α is a control parameter of fairness among UEs. With a smaller α, the scheduler tends to allocate more resources to the UEs, which have a low average bit rate in the past.

Based on $\mathbf{M}(t)$, the scheduling procedure is performed, as shown in Algorithm 1 [34]. The set of all available PRBs is defined as $\mathcal{P}$, and the set of all UEs having permission to be scheduled is defined as $\mathcal{M}$. The set of sub-bands assigned to UE i is denoted by $\mathcal{K}_i$. In each iteration, a PRB is assigned to the UE with the largest priority metric to

achieve proportional fairness. And this UE has no permission to be scheduled until the end of this TTI, unless there are still PRBs available after all UEs have been assigned. This procedure is repeated until there is no PRB left in the current TTI.

Algorithm 1 Scheduling algorithm based on priority metric

$\mathcal{P} \leftarrow \{1, 2, ..., N_{\text{PRB}}\}$
$\mathcal{M} \leftarrow \{1, 2, ..., N_{\text{UE}}\}$
$\mathcal{K}_i = \emptyset, \forall i = 1, ..., N_{\text{UE}}$
repeat
  $(\kappa, i) \leftarrow \arg\max_{\tilde{\kappa}\in\mathcal{P}, \tilde{i}\in\mathcal{M}} M_{\tilde{\kappa},\tilde{i}}$
  $\mathcal{K}_i \leftarrow \mathcal{K}_i \cup \{\kappa\}$
  $\mathcal{P} \leftarrow \mathcal{P} \setminus \{\kappa\}$
  $\mathcal{M} \leftarrow \mathcal{M} \setminus \{i\}$
  if $\mathcal{M} = \emptyset$ **then**
    $\mathcal{M} \leftarrow \{1, 2, ..., N_{\text{UE}}\}$
  end if
until $\mathcal{P} = \emptyset$

4.5.2 Numerical results

In the simulations, a network consisting 27 UEs is considered. The UEs are divided into small groups, where each group has 3 UEs moving with a constant speed from the set: {3, 10, 20, 30, 40, 50, 120, 150, 250} km/h. The other parameters are the same as in the previous simulations in this chapter.

The best CQI scheduling algorithm [75] is also presented here as reference. In the best CQI scheduling algorithm, a PRB is always assigned to the UE with largest CQI, to ensure maximum throughput.

Four different values of α are considered, namely, $\alpha = 10^{-1}$, 10^{-2}, 10^{-3} and $\alpha = 10^{-4}$. Mean throughput and fairness are compared, where the fairness index is defined as [77]

$$\varphi = \frac{\left(\sum_{i=1}^{N_{\text{UE}}} F_i\right)^2}{N_{\text{UE}} \sum_{i=1}^{N_{\text{UE}}} F_i^2}. \tag{4.121}$$

The maximum value of $\varphi = 1$ can be achieved, if all the users have the same throughput.

The mean throughput among UEs is shown in Figure 4.28, where the best CQI scheduling shows the best throughput for all the prediction schemes, except for extrapolation. The reason is that as shown in Figure 4.14, for the UEs with higher speed, the prediction accuracy of extrapolation is so bad, that the current predicted CQIs are effectively

random. This is also the reason for the high fairness of extrapolation, as shown in Figure 4.29. But an averaged throughput can still reflect the channel condition. Therefore, with the PF scheduler, the mean throughput for extrapolation is even better than the short-term average scheme.

Furthermore, as the value of α goes up, the throughput goes down, whereas the fairness goes up, as shown in Figure 4.29. The best CQI scheme shows rather poor fairness in most of the cases. It is also shown that the adaptive prediction scheme has slightly worse fairness than the short-term average scheme, however significantly better throughput. Therefore, it can be concluded that the adaptive prediction scheme is overall the best prediction scheme in this comparison.

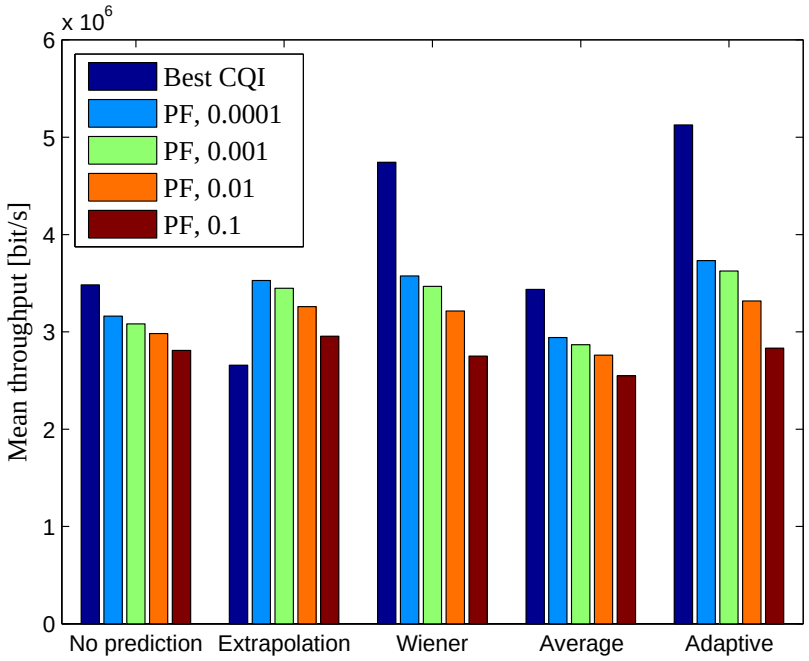

Figure 4.28: Mean value of average throughput for multiple users

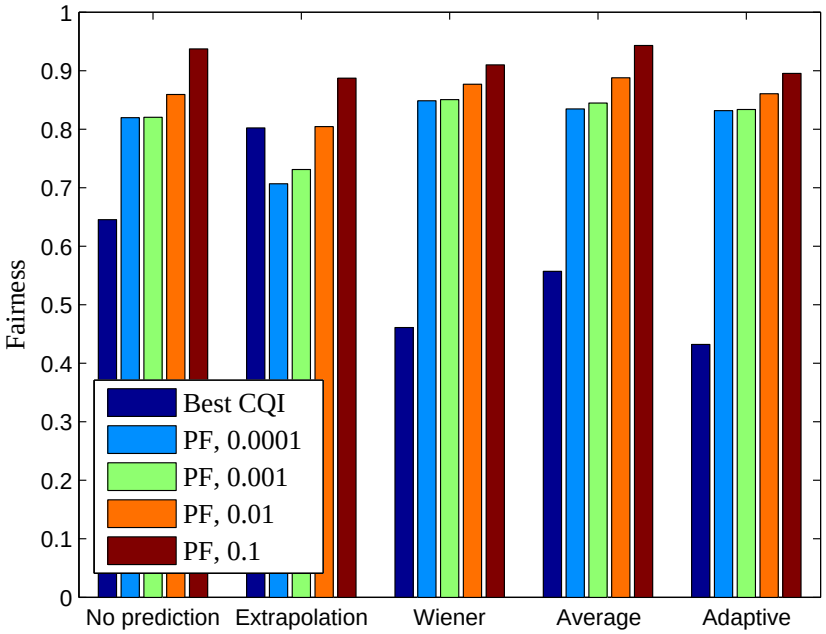

Figure 4.29: Fairness index for multiple users

5 Cellular Network Control

The control and optimization of cellular networks must be based on channel state information (CSI). However, as described in Chapter 4, perfect CSI is not available at the basestation, due to the doubly selective channel and limited feedback. Therefore, network control strategies should be based on the quantized feedback, namely, the CQI. On the one hand, the imperfect channel feedback undermines the performance of the network. On the other hand, the highly quantized nature of CQI makes the designing of very low complexity algorithms possible.

In this chapter, interference management through power control is considered as a case study of cellular network control strategies based on CQI. Heuristic algorithms are developed to optimize different KPIs. The performance of these strategies is evaluated by a network level simulator.

Parts of this chapter have been published in [43], [29], [94], [95] and [96].

5.1 Interference management in heterogeneous network through Tx power control

LTE is aiming at providing ubiquitous connectivity. However, indoor users usually suffer from strong penetration loss due to building walls. As a consequence of the increasing usage of data traffic, a macro-only network is no longer able to solve this problem. Therefore, femtocells are proposed as an economical solution to serve indoor UEs [22]. Femtocells introduce home evolved node B (HeNB) as low-power short range base stations, which are connected to the backhaul network via broadband connections. HeNBs generally have a maximum Tx power of 10-20 dBm, which results in a covered range of 10-30 meters. Due to the shield of electro-magnetic wave caused by building walls, HeNBs are supposed to have limited interference to the outdoor users, while giving the indoor users a seamless mobile connection. Thus, an efficient spatial reuse of the spectrum can be achieved in a heterogeneous network with overlayed macro- and femtocells [76] [18].

The deployment of femtocells can be categorized in different ways. According to access mode, they can be divided into open access and closed subscriber group (CSG), where open access grants every user the right to connect to a femtocell, and CSG gives service only to the users with proper licences [57]. According to spectrum usage, femtocells can either share the frequency band with macrocells to maximize the spectrum utilization or use a dedicated frequency band to avoid interference [66].

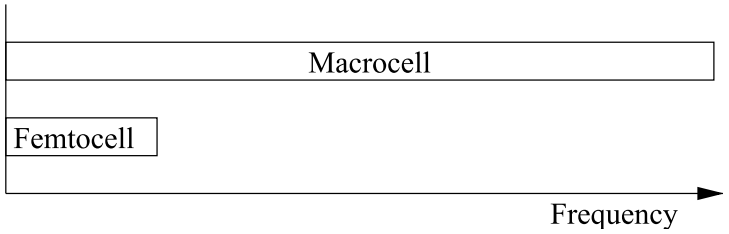

Figure 5.1: Partial frequency sharing

Although the dedicated channel deployment avoids the problem of CCI, both eNBs and HeNBs can only have a part of the available spectrum, thus have smaller bandwidth and possibly lower data throughput [57]. For this reason, partial sharing of the spectrum, as shown in Figure 5.1, is usually preferred, where the eNBs can use the full available frequency band and HeNBs can only use a part of it. The overlapped frequency band leads to CCI, which should be mitigated by using radio resource allocation and Tx power control.

The open access femtocells are usually deployed by the operators or enterprises to boost the service in user-concentrated indoor area, whereas the CSG are usually deployed by end users, who want to improve the signal quality at home. Due to this fact, the CSG HeNBs can be in suboptimal locations, with unknown environment and turned on and off randomly. In contrast to macrocells, which have fixed location and can be optimized with static location related information, CSG femtocells are preferred to be managed in an autonomous manner due to their plug-and-play property.

In a frequency sharing CSG system, the CCI is inevitable. Especially the macrocell user equipment (MUE) close to a femtocell could be severely interfered, if the HeNB is serving the home user equipment (HUE) with maximal Tx power. Therefore, the necessity of interference mitigation must be addressed [10]. Interference mitigation can be achieved in different ways, such as radio resource management, handover optimization and HeNB power control. The Tx power control of HeNB will be elaborated in this section.

In previous works, an adaptive power control based on signal to interference ratio (SIR) at cell edge is described in [57], where full knowledge of network layout is required. A distance based method is proposed in [23], which guaranties that the HUE has at least the same receive power as an MUE in the same location but without building walls. This model also requires a large amount of information, such as cell locations, power levels, antenna orientations and gains, etc. In addition, this model depends heavily on a reliable pathloss model. Another scheme based on the measured received power from eNB is also proposed in [23], where no location information is required. In [60], another adaptive power control scheme is proposed to utilized not only the downlink Rx power from macrocell but also the uplink Rx power from MUE. These methods aim at providing the same signal strength for the HUE as an outdoor MUE in the same location. As a drawback, for the area on cell edges, where the macrocell signal level is already poor, femtocells are not able to deliver good performance for HUEs.

Furthermore, the data rate requirement of different service types are not taken into consideration. The result is, the Tx power is higher than a sufficient level for some service which requires only a small data rate.

In a realistic scenario, the communication between eNB and HeNB is restricted, i.e., although both eNB and HeNB are connected to the back haul network with wired broadband connections, the communication between eNB and HeNB is only at a coarse time scale. That means, HeNB can not be controlled by a single entity in a realtime centralized fashion. Therefore, a decentralized solution is preferred. In this section, a fully decentralized, self-organized heuristic based on CQI is proposed for the downlink power control and interference mitigation in LTE femtocells. The proposed power control schemes dynamically adjust the Tx power to adapt to the UE service types and QoS requirements. The proposed scheme makes no strong assumptions, such as the knowledge of the whole network or location of every UE. Therefore, it is robust to the change of network environment.

5.1.1 System model

Consider a network with partial frequency sharing, CSG femtocells. The interference scenarios is demonstrated in Figure 5.3, where on top of the conventional co-tier interference among macrocells, several new kinds of interference arises, as shown in Table 5.1 [72]. The HeNB to HUE interference cannot be neglected, if the femtocells are densely deployed. The total number of cells in the network can be written as

$$S = S_{\mathrm{MC}} + S_{\mathrm{FC}}, \tag{5.1}$$

where S_{MC} is the number macrocells and S_{FC} is the number of femtocells. The SINR can be calculated with the Rx power of the signal and interferences. Taking a HUE i, which suffers from both co-tier and cross-tier interference, as an example, the SINR is given by

$$\gamma_{i,s}(t) = \frac{P_{i,s}(t)}{\sum\limits_{j=1}^{S_{\mathrm{MC}}} P_{i,j}(t) + \sum\limits_{j=S_{\mathrm{MC}}+1, j\neq s}^{S} P_{i,j}(t) + \sigma_w^2}, \tag{5.2}$$

where the indices of macrocells are smaller than the indices of femtocells. In practice, the femtocells have very small Tx power, thus, some $P_{i,j}, (j > S_{\mathrm{MC}})$ would be close to zero and negligible. The SINR of other UEs can be calculated similarly.

Channel model

The Rx power can be calculated with (4.7), where the pathloss is commonly modeled with the general form of

$$L_{i,j}(t) = A + C \log d_{i,j}(t) \tag{5.3}$$

where parameters A and C must be empirically determined according to the radio wave propagation environment and $d_{i,j}$ is the distance between base station j and user

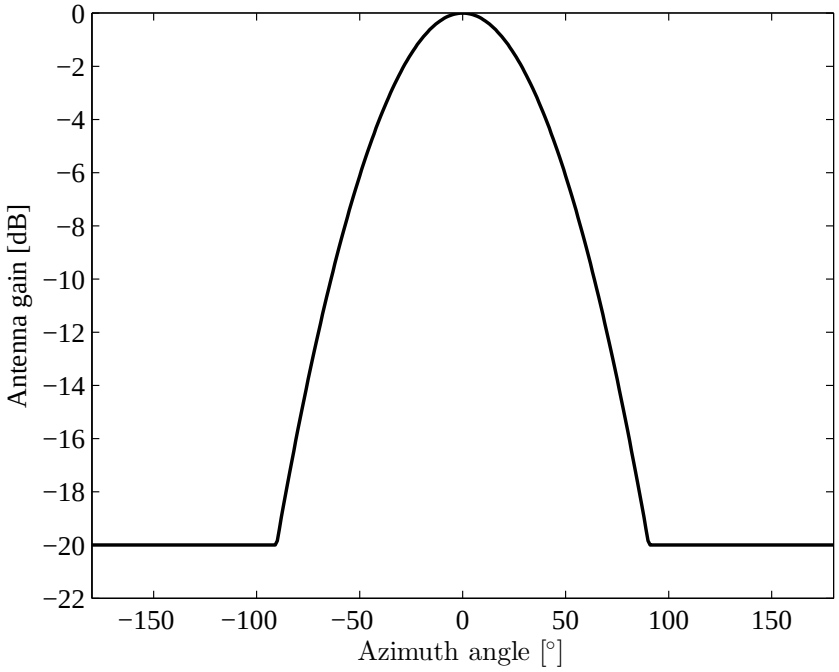

Figure 5.2: 3GPP electrical antenna tilt model

i. In addition, the wall penetration loss should be applied to the pathloss, as shown in Figure 5.4. In this case the pathloss can be written as

$$L_{i,j}(t) = A + C \log d_{i,j}(t) + L_{\mathrm{w}} \tag{5.4}$$

where L_{w} is the wall penetration loss.

Multi-path channel is considered in this thesis, where each path follows the Rayleigh fading model. An exponential power delay profile is also assumed.

Three-sector antennas are used in the eNBs. The standardized 3GPP antenna azimuth pattern is adopted in this work [9]. The azimuth pattern is modelled as a Gaussian-shaped main beam with a constant side lobe floor

$$G(\theta) = -\min\left(12\left(\frac{\theta}{\theta_{3\mathrm{dB}}}\right)^2, A_{\mathrm{m}}\right) \tag{5.5}$$

where θ is the azimuth angle, $\theta_{3\mathrm{dB}}$ is the half power beam width (HPBW) and A_{m} is the constant side lobe floor.

Traffic model

In most of the literatures, the system performance is evaluated with channel capacity, which is directly deduced from the SINR using Shannon's formula [57] [56]. However,

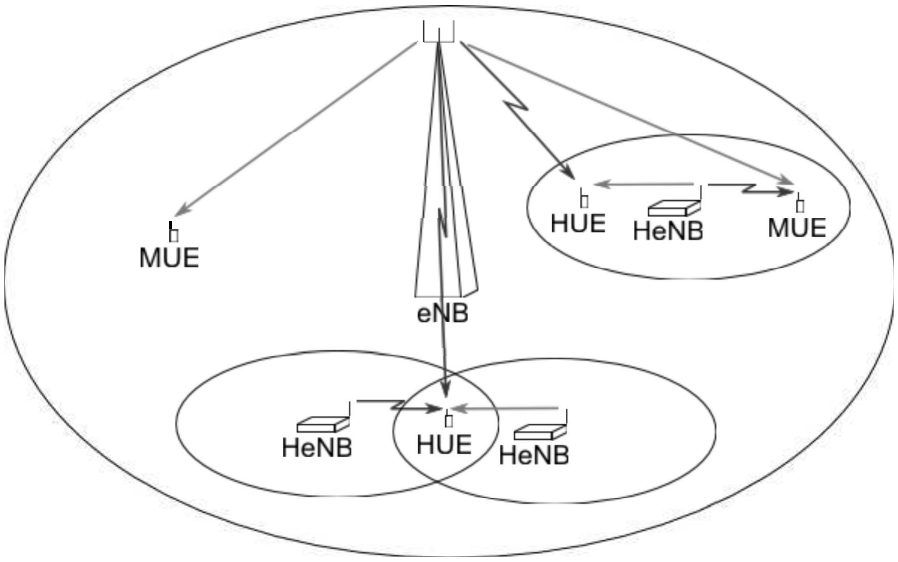

Figure 5.3: Co-tier and cross-tier interference in heterogeneous networks, interferences are marked in broken lines. Interferences from neighboring macrocells are not shown

this traffic model is unrealistic in real systems, especially for users who use voice communications. As long as the QoS requirement is met, the user cannot benefit from extra frequency band or further boost of signal strength.

In this work, the data traffic is modeled in a less abstract level. Three kinds of services are specified, namely, VoIP service, data service and web service. The VoIP users have the highest priority, which means the frequency resources will be first allocated to the VoIP users. The data rate requirement of VoIP users is fixed to 64 kbps, in another word, the throughput per unit energy can only be improved by reducing the power margin but not by increasing the data rate. Thus, this kind of user is also called margin adaptive (MA). The data users are also margin adaptive, but their priority is lower than the VoIP users. The data rate requirement for data users is a random number in the range of [512 - 2000] kbps. In contrast, the web users have a minimum data rate requirement, and the data rate should be maximized subject to the power limit. This kind of user is also called rate adaptive (RA) [55]. The assumed distribution of the users with different services is summarized in Tab. 5.2.

Aggressor	Victim	Type
eNB	MUE	Co-tier
eNB	HUE	Cross-tier
HeNB	MUE	Cross-tier
HeNB	HUE	Co-tier

Table 5.1: Co-tier and cross-tier interference table

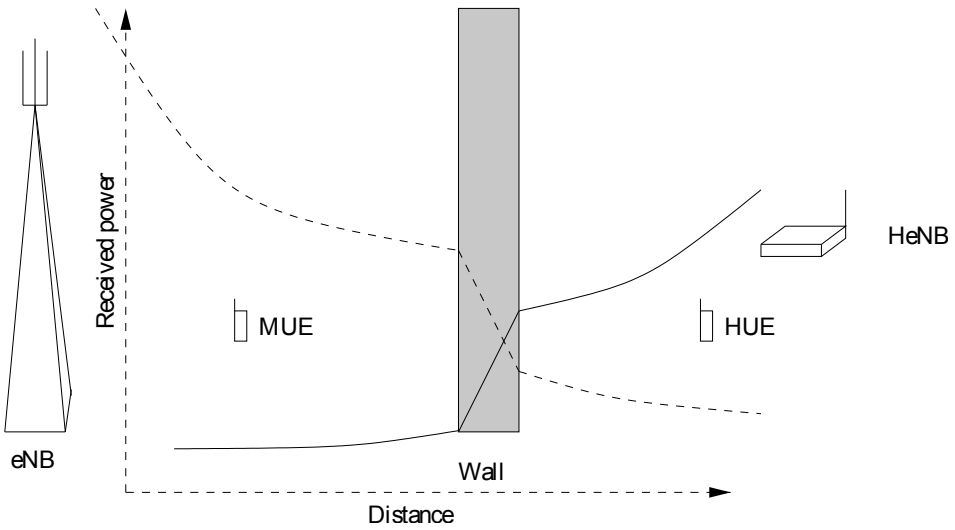

Figure 5.4: Rx power in heterogeneous network

Resource allocation

The resource allocation scheme should take both efficiency and fairness into account. Due to the frequency selective channels, each UE has different CQIs on different PRBs. The UEs with largest variation in their CQIs are most sensitive in the resource allocation. Therefore, those UEs should choose their PRBs first. The variance is used in this work to measure the variation in CQI.

Suppose there are in total

$$N_s = N_{\mathrm{MA},s} + N_{\mathrm{RA},s} \tag{5.6}$$

users associated to cell s, where $N_{\mathrm{MA},s}$ is the number of MA users and $N_{\mathrm{RA},s}$ is the number of RA user, respectively. The users are first sorted according to their service type. For each service type, the users are again sorted according to the variance of their CQIs. The user which has the highest variance pick the PRBs from the available PRB set $\mathcal{P}_s$, until its minimum data rate requirement R_i is met. And these PRBs are subtracted from set $\mathcal{P}_s$. After that, the user with second highest variance will pick. This process goes on iteratively until there is no PRB left or all the users have their minimum data rate requirements satisfied. If there are still PRBs left, those PRBs will be assigned to the RA user in the second round. The RA users pick the PRBs one at a time until there is no PRB left. Assuming the users are already sorted, and the user index is in ascending order, the resource allocation algorithm is summarized

Service	Priority	Rate requirement	Ratio
VoIP	High	64 kbps	10%
Data	Mid	[512-2000] kbps	40%
Web	Low	$\geq$ 64 kbps	50%

Table 5.2: Different types of service

Algorithm 2 Resource allocation algorithm

for each $s \in [1, S]$ **do**
  for each $i \in [1, \cdots, N_s]$ **do**
    while $\widetilde{R}_i < R_i$ & $\mathcal{P}_j \neq \emptyset$ **do**
      $\kappa \leftarrow \arg\max_{\tilde{\kappa} \in \mathcal{P}_s} Q_{i,\tilde{\kappa}}$
      $a_{i,\kappa} \leftarrow 1$
      $\mathcal{K}_i \leftarrow \mathcal{K}_i \cup \{\kappa\}$
      $\mathcal{P}_s \leftarrow \mathcal{P}_s \setminus \{\kappa\}$
      $\widetilde{R}_i \leftarrow B \sum_{\kappa} a_{i,\kappa} \cdot g(Q_{i,\kappa})$
    end while
  end for
  // Assign the left PRBs to RA users
  while $\mathcal{P}_s \neq \emptyset$ **do**
    for each $i \in [N_{\mathrm{MA},s} + 1, \cdots, N_s]$ **do**
      $\kappa \leftarrow \arg\max_{\tilde{\kappa} \in \mathcal{P}_s} Q_{i,\tilde{\kappa}}$
      $a_{i,\kappa} \leftarrow 1$
      $\mathcal{K}_i \leftarrow \mathcal{K}_i \cup \{\kappa\}$
      $\mathcal{P}_s \leftarrow \mathcal{P}_s \setminus \{\kappa\}$
    end for
  end while
end for

in Algorithm 2, where κ is the index of PRBs, $\emptyset$ is the empty set. The assignment parameter $a_{i,\kappa}$ is defined as

$$a_{i,\kappa} = \begin{cases} 1 & \text{PRB } \kappa \text{ is assigned to user } i \\ 0 & \text{otherwise} \end{cases}, \tag{5.7}$$

which is initially assigned to be 0. The calculation of $\widetilde{R}_{i,\kappa}$ utilizes the CQI to data rate mapping function $g(\cdot)$. And B is the bandwidth of a PRB.

This resource allocation algorithm is used by both eNBs and HeNBs. Since the only information the base stations need to make the resource allocation is the CQIs of their own users, this resource allocation algorithm is completely decentralized.

5.1.2 Autonomous Tx power control

One of the most important KPI in cellular network is the overall throughput. To maximize the overall throughput by power control, the objective function can be written as

$$\mathbf{U}_{\mathrm{opt}} = \arg\max_{\mathbf{U} \in \mathcal{U}^{S_{\mathrm{FC}}}} \sum_{i} F_i(\mathbf{U}), \tag{5.8}$$

where $\mathcal{U}$ is the set of feasible Tx power. Clearly, finding optimal solution for this optimization problem requires enormous effort. Moreover, the optimal solution must

be centralized. That implies perfect communications among eNBs and HeNBs, which can not be realized in current LTE systems. In addition, the data rate based utility function is not the only design criterion. The utility function based on coverage is also very important, and it is also evaluated in this work.

The conventional way to achieve interference mitigation through Tx power control usually depends on strong assumption of availability of full knowledge of the network or capability of the hardware, whereas the proposed CQI-based power control does not have this kind of dependency.

Conventional power control

In [23], a distance-based power control scheme is proposed. In this scheme, the femtocell Tx power is configured such that the UE at a pre-defined radius $d_{\max}$ would receive on average at least the same amount of power from the strongest macrocell, even if the macrocell signal has to go through building walls. Since this algorithm is aiming at average performance, fast fading is ignored. Find the eNB, which has the strongest signal at the UE as

$$\varsigma = \arg \max_{j \in \mathcal{S}_{\mathrm{MC}}} P_{i,j}(t), \tag{5.9}$$

where $\mathcal{S}_{\mathrm{MC}}$ is the set of all macrocells. And define the femtocell pathloss for radius $d_{\max}$ as $L_{i,s,\max}$

The distance-based HeNB Tx power can be calculated as

$$U_{s,\mathrm{dist}}(t) = \min \left(\frac{U_{\varsigma}(t) G_{\varsigma}(t) L_{i,s,\max}}{L_{s,\varsigma}(t)}, U_{\max} \right), \quad \forall s \in \mathcal{S}_{\mathrm{FC}} \tag{5.10}$$

where $U_{\max}$ is the maximum Tx power of HeNB, $L_{s,\varsigma}(t)$ is the estimated pathloss between eNB ς and HeNB s and $\mathcal{S}_{\mathrm{FC}}$ is the set of all femtocells..

Effectively, the Rx power of macrocell ς at the location of HeNB is estimated by

$$\widehat{P}_{s,\varsigma}(t) = \frac{U_{\varsigma}(t) G_{\varsigma}(t)}{L_{s,\varsigma}(t)}, \tag{5.11}$$

and used to determine the Tx power of the HeNB. The performance of this method heavily relies on the accuracy of the pathloss. However, since the pathloss is calculated by empirical models, they are not completely reliable.

The distance-based power control can be improved by taking one step further and replace the estimated Rx power at the location of HeNB by the measured one, supposing the HeNB device is capable of doing the measurement. And the Tx power is given by

$$U_{s,\mathrm{meas}}(t) = \min \left(P_{s,\varsigma}(t) L_{i,s,\max}, U_{\max} \right), \quad \forall s \in \mathcal{S}_{\mathrm{FC}}, \tag{5.12}$$

where $P_{s,\varsigma}(t)$ is the measured Rx power of macrocell ς at the location of HeNB. Since the Rx power is from measurements, fast fading is taken into account. Therefore, the performance of the measurement-based scheme is better than the distance-based scheme.

Static CQI-based power control

By observing the traffic model, one can find that the HeNB needs relatively small Tx power to satisfy MA users. However, to give RA users the maximum achievable data rate, each HeNB must transmit with much larger power and thus cause higher interference to other users nearby. Therefore, the Tx power should be controlled in such a manner that the HeNBs do not always try to provide maximum data rate for RA users. More specifically, an offset value $\Upsilon_{i,s}(t)$ is applied on user i upon its minimum data rate requirement. After that, the RA users can be treated as MA users.

Technically, the RA users are not really rate adaptive in this case, unless $\Upsilon_{i,s}(t) \to \infty$. They are only served with their minimum data rate demand, if $\Upsilon_{i,s}(t) = 0$. Larger offset data rate means the HeNB is more "selfish" to its own users and thus produces more interference to other users. In another word, the indoor throughput is potentially higher and the outdoor coverage is potentially poorer. A carefully chosen data rate offset should be able to offer a good balance between overall throughput and coverage. It is worth mentioning that $\Upsilon_{i,s}(t) \to \infty$ does not necessarily mean transmitting with maximum power, since the HUE may need a smaller power to reach the maximum data rate. In this sense, even a fixed $\Upsilon_{i,s}(t) \to \infty$ can reduce interference, without sacrificing any throughput, comparing to an unoptimized network.

Furthermore, since in indoor environment, multi-path components have a smaller delay spread, the HeNB-HUE channel is assumed to be flat here. Based on this idea, a power control algorithm using CQI as input can be derived. A desired CQI for each HUE can be calculated with the data rate demands and available bandwidth resources. The Tx power can be tuned according to the relationship between the desired CQI and actual CQI. Furthermore, the data rate offset can be configured by upper layer protocols, according to applications.

The power control algorithm is performed by each femtocell independently. At certain time t, the total data rate demand $\widetilde{F}_s(t)$ of femtocell s is calculated by summing up the data rate demand of all its serving HUEs

$$\widetilde{F}_s(t) = \sum_{i=1}^{N_{\mathrm{MA},s}} \widetilde{F}_i(t) + \sum_{i=N_{\mathrm{MA},s}+1}^{N_s} (\widetilde{F}_i(t) + \Upsilon_{i,s}(t)), \tag{5.13}$$

where $\widetilde{F}_i(t)$ is the data rate demand of user i. The number of PRBs required by user i is then estimated by the proportion of this user's data rate demand to the total data rate demand of the femtocell

$$K_i(t) \leftarrow \lceil \frac{\widetilde{F}_i(t)}{\widetilde{F}_s(t)} \cdot (K_{\mathrm{PRB}} - N_s + 1) \rceil, \tag{5.14}$$

where K_{PRB} is the total number of available PRBs. The round up operation guarantees that each user gets at least one PRB and the summation of PRBs over all the HUEs does not exceed the total number of available PRBs. The desired bandwidth efficiency

Algorithm 3 Power control algorithm with fixed data rate offset

```
for each s ∈ S_FC do
    for each t ∈ [t_min, t_max] do
        F̃_s(t) ← Σ_{i=1}^{N_MA,s} F̃_i(t) + Σ_{i=N_MA,s+1}^{N_s} (F̃_i(t) + ϒ_{i,s}(t))
        for all HUE do
            K_i(t) ← ⌈ F̃_i(t) / F̃_s(t) · (K_PRB − N_s + 1) ⌉
            χ_i(t) ← ⌈ η^{-1}( F̃_i(t) / (B·K_i(t)) ) ⌉
            if Q_i(t) < χ_i(t) & U_s(t − T_b) < U_max then
                U_s(t) ← U_s(t − T_b) + ΔU
            else if Q_i(t) > χ_i(t) & U_s(t − T_b) > U_min then
                U_s(t) ← U_s(t − T_b) − ΔU
            else
                U_s(t) ← U_s(t − T_b)
            end if
        end for
    end for
end for
```

is given by $\frac{\widetilde{F}_i(t)}{B \cdot K_i(t)}$. The desired CQI χ_i can be calculated with the inverse of CQI to bandwidth efficiency mapping function as

$$\chi_i(t) \leftarrow \lceil \eta^{-1}(\frac{\widetilde{F}_i(t)}{B \cdot K_i(t)}) \rceil, \tag{5.15}$$

where B is the bandwidth of a PRB. After that, in each time slot, the realtime CQI is compared to the desired CQI. If the realtime CQI is too low, the Tx power is increased and vice versa. The whole procedure is shown in Algorithm 3.

The HUEs are usually indoor and move only with pedestrian speed. Consequently, their CQIs vary slowly and can be perfectly predicted. Hence, after the algorithm reaches a steady state, there will be only seldom vibrations in the Tx power. The Tx power increment ΔU determines how fast the algorithm converges. Since CQI is discrete valued, the variation in SINR $\Delta\gamma$, which changes CQI by 1, can be calculated from Figure 4.5. Assuming the interference stay unchanged, the CQI can be changed by 1, if the variation in Rx power ΔP has the same value as $\Delta\gamma$ in dB. Considering there are femtocells with overlapped coverage area, ΔU is set to $\Delta\gamma/2$ in this work.

Dynamic CQI-based power control

The data rate offset can be empirically calibrated through simulations. Other than using a fixed value, it can also be set according to the number of interfered users, assuming a HeNB constantly tracks the number of users in its service range. Since MUEs, especially the indoor MUEs are most vulnerable to interference, the data rate

offset is set to 0, if any MUE nearby is detected. Otherwise, the data rate offset is set as an exponential decay function to reduce interference to HUEs. This algorithm is summarized in Algorithm 4.

Algorithm 4 Dynamic setting of data rate offset

if $N_{\mathrm{MUE},s}(t) > 0$ **then**
  $\Upsilon_{i,s}(t) \leftarrow 0, \forall i \in [1, \cdots, N_s]$
else
  $\Upsilon_{i,s}(t) \leftarrow \Delta\Upsilon^{1-N_{\mathrm{HUE},s}(t)}, \forall i \in [1, \cdots, N_s]$
end if

5.1.3 Numerical results

Simulation environment

As shown in Figure 5.5 (a), the simulation is conducted for an urban area with 19 eNBs, each serving 3 cells. The inter-site distance is 500 meters. Multiple buildings are randomly located in the simulated area. On average, each cell has one building with 40 apartments. The apartments are located in dual-stripe blocks as shown in Figure 5.5 (b) [2]. 20% percent of the randomly chosen apartments are equipped with HeNBs in the middle of the rooms. The activation rate of HeNBs is 50%. The penetration loss is $L_{\mathrm{iw}} = 5$ dB for the inner wall and $L_{\mathrm{ow}} = 10$ dB for the outer wall. The frequency sharing scheme is partial sharing, where the eNBs have access to the whole spectrum and the HeNBs can use only 10% of it. Some other parameters of the eNB and HeNB are summarized in Table 5.3.

	HeNB	eNB
Carrier frequency	2 GHz	2GHz
Spectrum	1 MHz	10 MHz
Antenna pattern	Omni-directional	3-sector
Max. Tx power	20 dBm	46 dBm
Antenna gain	5 dBi	14 dBi

Table 5.3: Simulation parameters.

User	Average speed	Mobility pattern
Outdoor pedestrian	1 m/s	Along streets
Outdoor vehicular	10 m/s	Along streets
Indoor pedestrian	1 m/s	Indoor, random

Table 5.4: User mobility parameters.

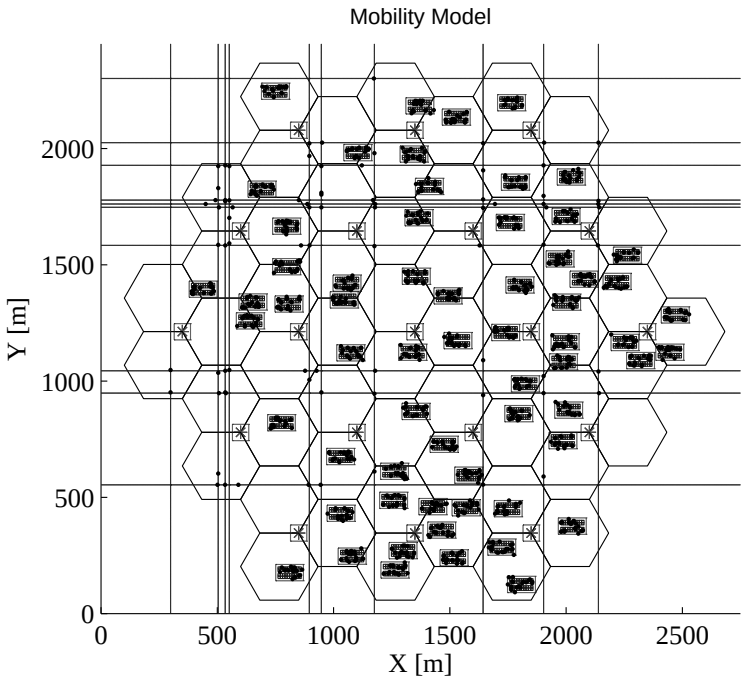

(a)

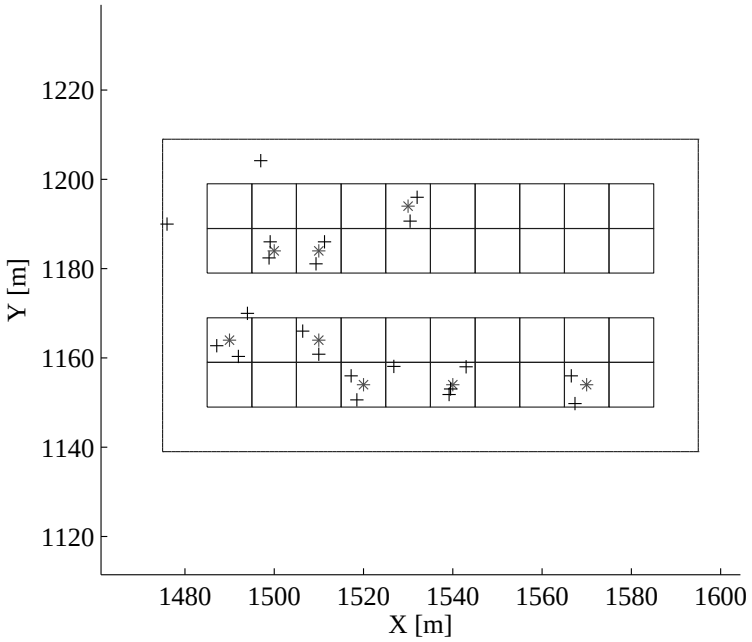

(b)

Figure 5.5: (a) Network layout with hexagonal grids. Horizontal and vertical lines denotes streets. (b) Dual stripe model. HeNBs are located in the center of apartments.

eNB-indoor UE	$L_{i,j,\mathrm{dB}} = 15.3 + 37.6 \log d_{i,j} + q \cdot L_{\mathrm{iw}} + L_{\mathrm{ow}}$
eNB-outdoor UE	$L_{i,j,\mathrm{dB}} = 15.3 + 37.6 \log d_{i,j}$
HeNB-indoor UE	$L_{i,j,\mathrm{dB}} = \max(38.46 + 20 \log d_{i,j}, 15.3 + 37.6 \log d_{i,j}) + 0.7 d'_{i,j} + q \cdot L_{\mathrm{iw}}$
HeNB-outdoor UE	$L_{i,j,\mathrm{dB}} = \max(38.46 + 20 \log d_{i,j}, 15.3 + 37.6 \log d_{i,j}) + 0.7 d'_{i,j} + q \cdot L_{\mathrm{iw}} + L_{\mathrm{ow}}$

Table 5.5: Pathloss models.

In total 400 MUEs are simulated, with 80% of them located indoor. In addition, each HeNB serves 2 HUEs, which are in the same apartment. Mobility models are employed to create realistic movement patterns of the UEs. The indoor UEs can move freely inside the apartments and outdoor UEs can only move along streets, which are laid orthogonally on the map. The mobility parameters are given in Table 5.4.

The channel gain H is modeled as Rayleigh process, and the pathloss L is modeled as described in Table 5.5, where d is the distance between base station and UE, d' is the distance between the UE and its projection on the building wall, q is the number of inner walls separating base station and UE.

Evaluation metrics

Two KPIs are defined for evaluation, namely, average throughput and coverage in terms of user satisfaction ratio. For the sake of simplicity, the mismatch of CQI prediction is not considered here. Therefore, the throughput of user i is calculated as

$$F_i(t) = \sum_{\kappa \in \mathcal{K}_i} B \cdot \eta \left(Q_{i,s}(t, \kappa) \right). \tag{5.16}$$

The user satisfaction ratio is defined as

$$\eta_{\mathrm{sat}} = \frac{N_{\mathrm{sat}}}{N_{\mathrm{UE}}}, \tag{5.17}$$

where N_{sat} is the number of satisfied UEs and N_{UE} is the total number of UEs. A user is satisfied, if its minimum data rate demand is fulfilled. Generally speaking, the coverage KPI has a more important role in cellular networks, considering the fact that mobile subscribers usually have more tolerance to slow connections than to being out of service.

Simulation results

For the static CQI-based power control, data rate offset with both very high value approaching infinity and very low value of 0 is considered. For the dynamic power control, $\Delta\Upsilon$ is set to 5 Mbps. For reference, the conventional measurement-based

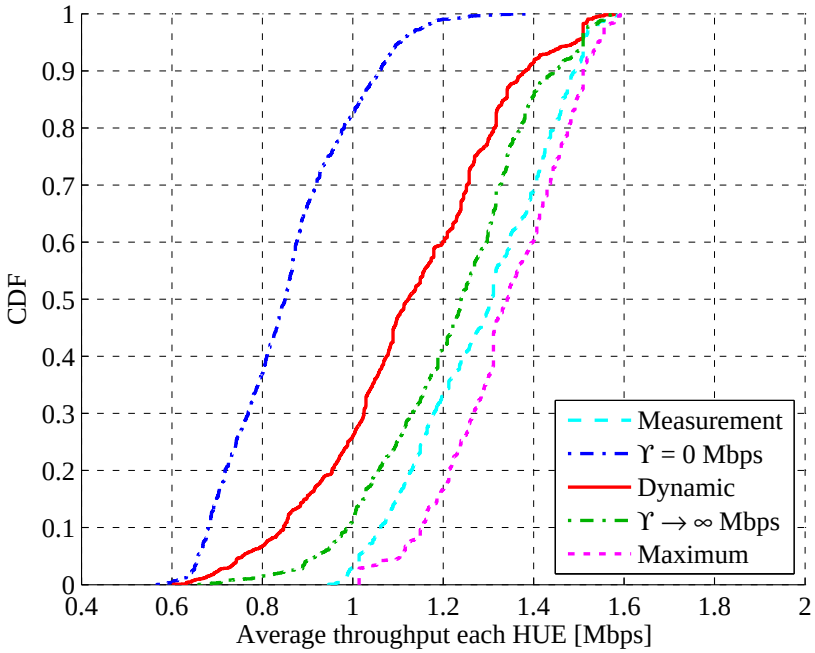

Figure 5.6: CDF of throughput for all HUEs

algorithm is also tested. The Rx power $P_{s,\varsigma}(t)$ is available at HeNB s. In addition, $L_{i,s,\max}$ is calculated with Table 5.5, which means the estimation of pathloss at HeNB is perfect. In addition, the results of having all HeNBs transmitting with their maximum power is shown as unoptimized results.

In Figure 5.6 and Figure 5.7, the cumulative distribution functions (CDFs) of throughput for all HUEs and MUEs are compared, respectively. Since the probability of having multiple HeNBs serving the same area and thus interfere with each other is small, using maximum Tx power gives higher SINR for the HUEs. Hence, it offers the best average throughput for HUEs, as shown in Figure 5.6. However, the price is strong interference to MUEs, which can be seen from the worst throughput CDF curve in Figure 5.7.

The measurement-based power control (labeled as "Measure" in the figures) try to match the Rx power of the HUE to the Rx power from the closest eNB. Therefore, the HeNBs located at cell edges have very low Tx power, due to the large pathloss at cell edge for eNBs. Consequently, the throughput of HUEs is worse in this case, as depicted in Figure 5.6. However, the throughput of MUEs is higher, due to smaller interference, as illustrated in Figure 5.7.

The two extreme data rate offsets offers the performance bound for static CQI-based power control. For $\Upsilon = 0$, HeNBs generate minimum amount of interference to MUEs, while still guarantee that every HUEs is served with its minimum data rate demand. Therefore, $\Upsilon = 0$ leads to the lowest throughput for HUEs but highest throughput for MUEs. In comparison, with $\Upsilon \to \infty$, the throughput of HUEs is increased dra-

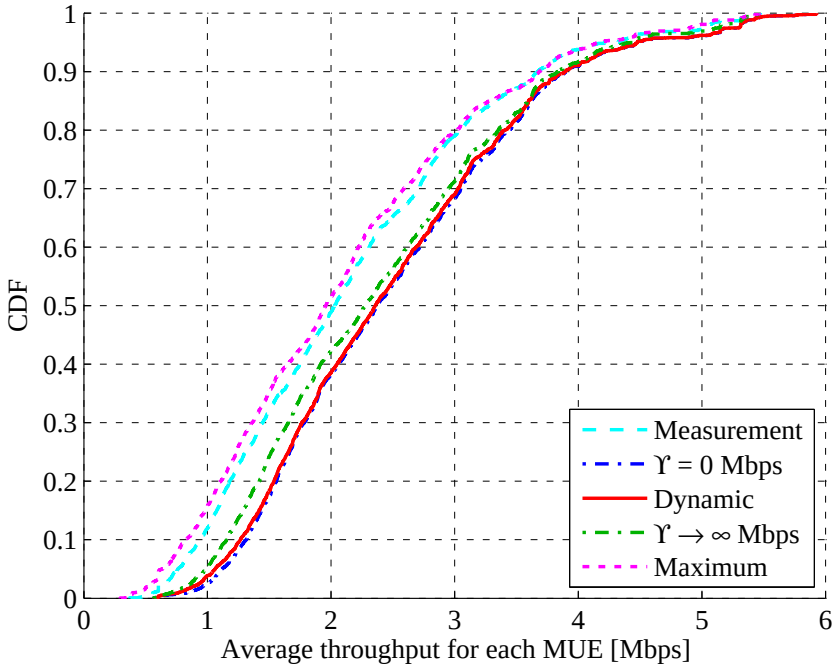

Figure 5.7: CDF of throughput for all MUEs

matically, and the throughput of MUEs is not affected so much. Bounded by these two extreme cases, the throughput of dynamic CQI-based power control for HUEs is between $\Upsilon = 0$ and $\Upsilon \to \infty$ and for MUE is almost the same as $\Upsilon = 0$.

Due to the fact that the number of MUEs is generally larger than of HUEs, the advantage in throughput for $\Upsilon \to \infty$ can also be observed for all UEs, as shown in Figure 5.8. However the advantage is not so significant. Meanwhile, $\Upsilon = 0$ gives much lower average throughput and all the other schemes performs similarly.

More details can be observed from Figure 5.9, where the mean throughput among all UEs is plotted for different data rate offset values. The measurement-based algorithm offers almost no improvement in mean throughput, whereas the dynamic CQI-based algorithm outperforms them both. Only with very small Υ values ($\Upsilon < 0.5$ Mbps), the static CQI-based algorithm has smaller mean throughput than the unoptimized system. As the data rate offset increases, the mean throughput also increases until a convergence is reached. Up to this point, the CQI-based algorithms do not show significant improvement in throughput performance. However, the real advantage can be seen from the coverage performance.

In Figure 5.10, the user satisfaction ratios are compared for different schemes. Only around 92.5% of the UEs have their minimum data rate demand met. With the conventional measurement-based algorithm, this number is increased to 93%. For static CQI-based algorithm, the user satisfaction ratio drops while Υ increases. But through the whole range of Υ, the overall coverage is always above 95%. Comparing to the conventional scheme, the advantage is evident. Moreover, the dynamic algorithm

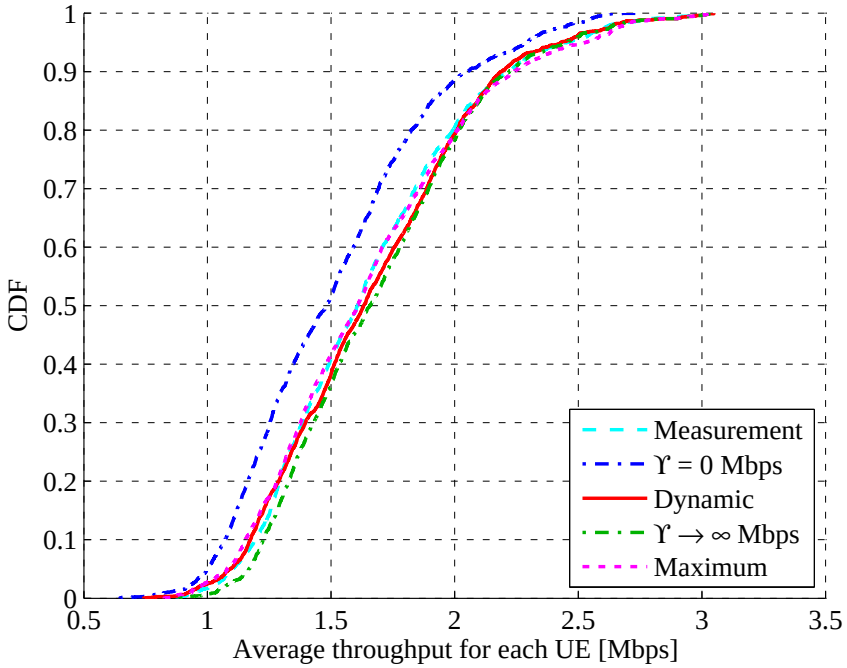

Figure 5.8: CDF of throughput for all UEs

offers an overall coverage of around 96%, almost as high as $\Upsilon = 0$. Therefore, one can conclude that comparing to the static CQI-based algorithm, the dynamic algorithm provides either almost the same coverage with much better throughput (for $\Upsilon = 0$), or better coverage with comparable throughput. Consider the fact that coverage is more important in cellular networks, the dynamic algorithm is preferred.

To summarize, the conventional measurement-based algorithm relies on the HeNB's ability of measuring Rx power of eNB and very accurate pathloss model. Even though these assumptions are quite strong, the improvement in performance is limited. The CQI-based algorithms works with less assumptions and thus is easier to implement. Still both the throughput and coverage are better. Furthermore, the dynamic algorithm provides a good balance between throughput and coverage, by adapting the data rate offset to the number of interfered UEs.

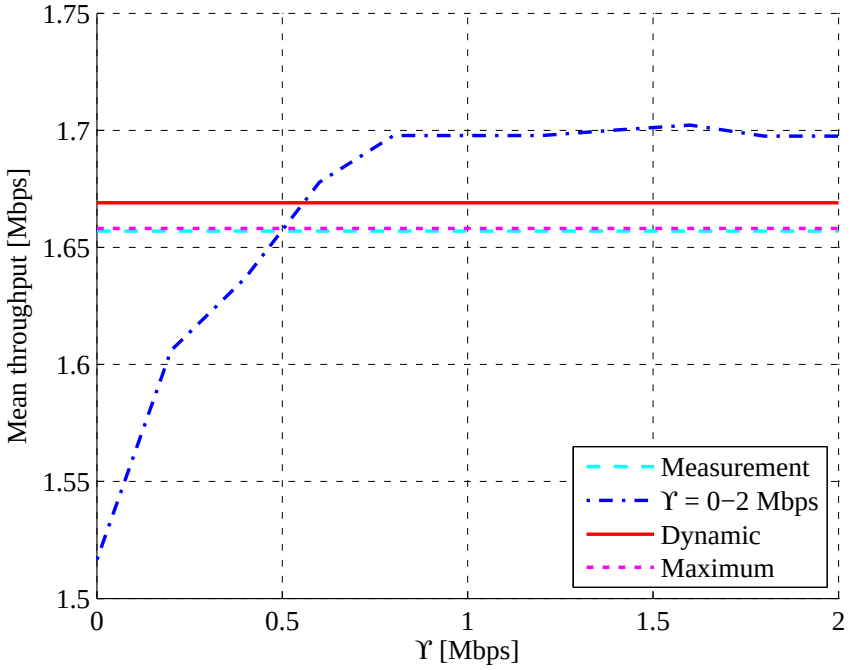

Figure 5.9: Mean throughput for different data rate offset

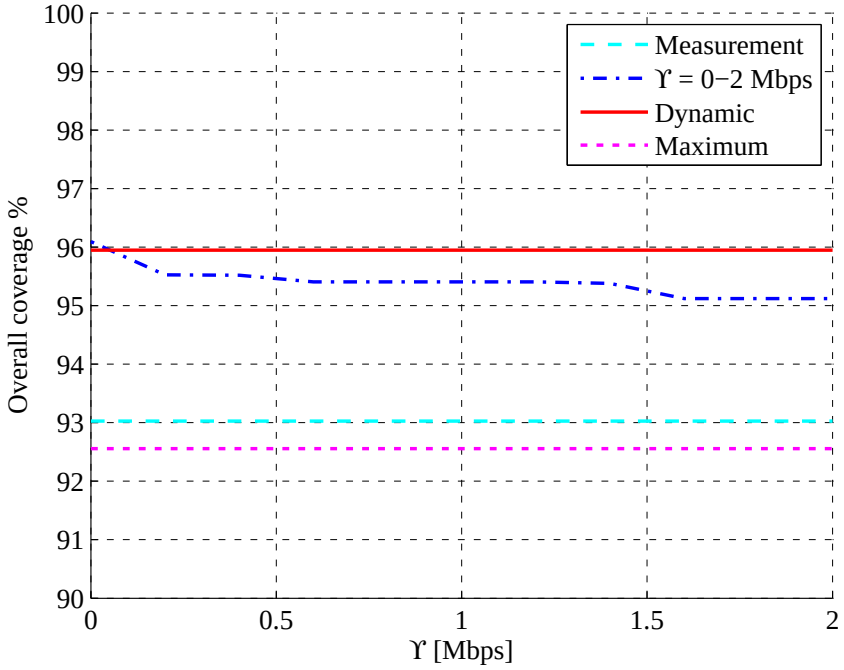

Figure 5.10: Average user satisfaction rate for different data rate offset

6 Conclusion and Outlook

6.1 Summary

The next generation mobile cellular network aims at providing very high data rate and ubiquitous connectivity. To achieve these goals, sophisticated network control methods are required. Since the 4th generation mobile cellular system is constituted of many advanced techniques, 3GPP standards are established to provide unified technical specifications and thus ensure compatibility. Based on 3GPP specifications, various strategies of wireless network control are addressed in this thesis.

As the most fundamental part of mobile networks, link level modeling of wireless channel is first investigated. Existing modeling methodologies are studied and compared. Based on the geometry-based stochastic channel model and deterministic ray-launcher, a semi-stochastic MIMO channel model is derived. The deterministic part of the semi-stochastic channel model can effectively utilize geometric description of the propagation environment, whereas the stochastic part can generate enough randomness for Monte-Carlo simulations. When comparing with real data from a measurement campaign in the German city of Ilmenau, the semi-stochastic model shows better accuracy than the WINNER model. Thus, the benefit of using environment data is proven.

Although with good description of the propagation environment, wireless channel can be properly modeled, in reality, the BSs do not possess perfect information about the up-to-date channel state. The most important channel state information comes from the CQI feedback of the users. Due to the scarcity of spectrum resources, the CQI feedback is made of quantized SINR. In the 3GPP standards, the CQI feedback for several PRBs consists only 4 bits. Meanwhile, the SINR is always varying, because of the movement of the users. To understand the variation of SINR, statistical properties of SINR are presented analytically. Moreover, various prediction schemes based on SINR are studied. Since different prediction schemes show different behavior for BSs moving with different speed, using an approximated autocovariance function, optimal prediction schemes can be chosen to adapt to the speed. The prediction noise can be approximated by a Gaussian distributed noise; thereby the analytical expression of bandwidth efficiency can be obtained.

Furthermore, HARQ is also considered in the analysis of feedback strategies. An analytical expression of the bandwidth efficiency in the presence of HARQ is derived, on the condition that the buffer size is large enough. The buffer size affects not only throughput but also latency. For a larger buffer size, the throughput is larger, however a larger latency is also to be expected. Another interesting fact is, since

the retransmission effectively improves the effective SNR, a biased predictor is not necessarily worse than an unbiased one. This work shows that for noisy predictor, a small positive bias leads to improvement in bandwidth efficiency, for a large prediction noise.

Since at the BS side, the channel state is available only in the form of CQI, network control algorithms can be developed based on real time CQIs. A case study of transmit power control for femtocells is offered in this work. As a solution to improve indoor coverage, femtocells are introduced as low-power, indoor BSs. Due to the shared frequency spectrum among femtocells and macrocells, co-channel interference is inevitable. Conventional interference suppression methods usually require full knowledge of the network structure or depend on the accuracy of the pathloss model. The presented power control scheme takes only the feedback CQIs as input. By differentiating service types of users and applying different QoS constraints, the transmit power of femtocells can be managed in a self-organizing fashion. For MA users, the Tx power is only sufficient to meet their rate demands, whereas, RA users are also treated as MA users with an offset data rate. Furthermore, the offset data rate can be chosen according to the number of interfered users in the vicinity of the femtocell. The self-organizing power control does not need prior information about the network structure and thus is easy to implement. It shows superior performance comparing to conventional methods in both capacity and coverage.

6.2 Outlook

Due to the immensity of the knowledge about wireless networks, the studies offered in this work are only a tip of the iceberg. It is hoped that the perspectives presented in this work can lead to further in-depth investigations on network control strategies for wireless networks.

Firstly, the semi-stochastic MIMO channel modeling methodology can be extended to vehicle-to-vehicle (V2V) communications with both moving MS and BS. Different characteristics of the V2V channels also demand stochastically generated scatterers.

Secondly, the analytical expression of bandwidth efficiency along with its association to effective SNR and CQI can be exploited for system optimization. The bias of the predictor and buffer size can be optimized subject to bandwidth efficiency and latency.

Finally, some more optimization work can done to the Tx power control schemes to further improve the coverage and capacity. Due to the simplicity of this scheme, it would be really interesting to have this algorithm implemented in real systems and tested for the performance.

A Multivariate Gaussian integral

Start from the well known Gaussian integral

$$\int_{-\infty}^{\infty} \exp\left\{-q^2\right\} \mathrm{d}x = (\pi)^{\frac{1}{2}}, \tag{A.1}$$

it is easy to get

$$\int_{-\infty}^{\infty} \cdots \int_{-\infty}^{\infty} \exp\left\{-\frac{1}{2}\sum_{i=1}^{N} a_i q_i^2\right\} \mathrm{d}q_1 \cdots \mathrm{d}q_N = \frac{(2\pi)^{\frac{N}{2}}}{\sqrt{a_1 a_2 \cdot a_N}}, \tag{A.2}$$

Denote q by a linear transformation

$$q_i = \sum_{j=1}^{N} B_{i,j} x_j, \quad 1 \leq i \leq N \tag{A.3}$$

where $\det(B) \neq 0$. The matrix notation is given by

$$\sum_{i=1}^{N} a_i q_i^2 = \mathbf{x}^{\mathrm{T}}\mathbf{B}^{\mathrm{T}}\mathbf{A}\mathbf{B}\mathbf{x} = \mathbf{x}^{\mathrm{T}}\mathbf{C}\mathbf{x}, \tag{A.4}$$

where $\mathbf{A}$ is a positive definite diagonal matrix. Its elements can be written as

$$A_{i,j} = a_i \delta_{i,j}, \tag{A.5}$$

where $\delta_{i,j}$ is the Kronecker delta and

$$\sqrt{a_1 a_2 \cdot a_N} = (\det(\mathbf{A}))^{\frac{1}{2}}. \tag{A.6}$$

Matrix $\mathbf{B}$ is actually the Jacobian matrix, therefore, the following holds true [48]:

$$\mathrm{d}q_1 \cdots \mathrm{d}q_N = |\det(\mathbf{B})| \mathrm{d}x_1 \cdots \mathrm{d}x_N. \tag{A.7}$$

Moreover, the determinant of $\mathbf{C}$ can be calculated with

$$\det(\mathbf{C}) = \det(\mathbf{B}^{\mathrm{T}}\mathbf{A}\mathbf{B}) = \det(\mathbf{B})^2 \det(\mathbf{A}). \tag{A.8}$$

Substitute (A.4) and (A.7) into the left side of (A.2) results in

$$\int_{-\infty}^{\infty} \cdots \int_{-\infty}^{\infty} \exp\left\{-\frac{1}{2}\sum_{i=1}^{N} a_i q_i^2\right\} \mathrm{d}q_1 \cdots \mathrm{d}q_N$$
$$= \int_{-\infty}^{\infty} \cdots \int_{-\infty}^{\infty} \exp\left\{-\frac{1}{2}\mathbf{x}^{\mathrm{T}}\mathbf{C}\mathbf{x}\right\} |\det(\mathbf{B})| \mathrm{d}x_1 \cdots \mathrm{d}x_N. \tag{A.9}$$

Finally, with (A.8), the multivariate Gaussian integral can be derived:

$$\frac{1}{(2\pi)^{\frac{N}{2}}} \int_{-\infty}^{\infty} \cdots \int_{-\infty}^{\infty} \exp\left\{-\frac{1}{2}\mathbf{x}^{\mathrm{T}}\mathbf{C}\mathbf{x}\right\} \mathrm{d}\mathbf{x} = \frac{1}{|\det(\mathbf{B})| \left(\det(\mathbf{A})\right)^{\frac{1}{2}}} \tag{A.10}$$
$$= \left(\det(\mathbf{C})\right)^{-\frac{1}{2}}. \tag{A.11}$$

Notation

$(\cdot)^*$	Complex conjugate
$(\cdot)^{\mathrm{H}}$	Hermitian transpose
$(\cdot)^{\mathrm{T}}$	Matrix transpose
J_0	Zero order Bessel function of the first kind
$\mathbb{C}$	Set of complex numbers
E	Expectation
diag	Diagonal matrix
tr	Matrix trace
unvec	Inverse operation of vec
vec	Vectorization
$\odot$	Element-wise product
$\otimes$	Kronecker product
B	Bandwidth, page 44
F	Throughput, page 44
G	Antenna gain, page 42
K	Number of subcarriers, page 9
L	Number of channel taps, page 7
N_{Rx}	Number of receive antennas, page 12
N_{Tx}	Number of transmit antennas, page 12
N_{sin}	Number of sinusoids, page 20
N_{PRB}	Number of PRBs, page 82
N_{UE}	Total number of UEs, page 82

N_{sat} Total number of satisfied UEs, page 99

P Rx power, page 13

P_{e} Error probability, page 42

R Correlation function, page 8

S Number of base stations, page 89

S_{FC} Number of femtocell base stations, page 89

S_{MC} Number of macrocell base stations, page 89

T Symbol duration, page 7

T_{b} PRB duration, page 62

T_{s} Sampling interval, page 7

U Average Tx power, page 42

W Frequency domain additive white Gaussian Noise, page 12

X Frequency domain transmitted signal, page 10

Δf Subcarrier spacing, page 10

Δt Time difference, page 8

Φ Initial phase, page 20

Υ Offset data rate, page 95

β Calibration parameter in EESM, page 43

η Spectral efficiency, page 44

η_{sat} User satisfaction ratio, page 99

γ Signal to interference plus noise ratio, page 13

γ_{e} Effective signal to noise ratio, page 43

κ PRB index, page 43

$\mathbf{H}_{\text{corr}}$ Channel impulse response matrix generated with full correlation matrix, page 23

$\mathbf{H}_{\text{f}}$ Channel frequency response matrix, page 13

$\mathbf{H}_{\text{iid}}$ Channel impulse response matrix for i.i.d. model, page 22

$\mathbf{H}_{\text{kron}}$ Channel impulse response matrix generated with the Kronecker model, page 24

$\mathbf{H}_{\mathrm{t}}$ Channel impulse response matrix, page 12

$\mathbf{H}_{\mathrm{weich}}$ Channel impulse response matrix generated with the Weichselberger model, page 25

$\mathbf{I}$ Identity matrix, page 33

$\mathbf{Q}$ Frequency domain spatial signal covariance matrix, page 33

$\mathbf{Q}_{\mathrm{Rx}}$ Rx spatial signal covariance matrix, page 24

$\mathbf{Q}_{\mathrm{Tx}}$ Tx spatial signal covariance matrix, page 24

$\mathbf{R}$ Correlation matrix, page 64

$\mathbf{R}_{\mathrm{H}}$ Spatial correlation matrix, page 23

$\mathbf{R}_{\mathrm{Rx}}$ Rx spatial correlation matrix, page 23

$\mathbf{R}_{\mathrm{Tx}}$ Tx spatial correlation matrix, page 23

$\mathbf{U}_{\mathrm{Rx}}$ Eigenbase of Rx spatial correlation matrix, page 24

$\mathbf{U}_{\mathrm{Tx}}$ Eigenbase of Tx spatial correlation matrix, page 24

$\mathbf{\Omega}$ Power coupling matrix, page 25

$\mathbf{\Sigma}$ Covariance matrix, page 55

$\mathbf{r}$ Correlation vector, page 64

$\mathbf{w}$ Filter vector, page 64

$\mathbf{w}_{\mathrm{f}}$ Additive white Gaussian noise vector in frequency domain, page 13

$\mathbf{w}_{\mathrm{t}}$ Additive white Gaussian noise vector, page 12

$\mathbf{x}_{\mathrm{f}}$ Transmitted signal vector in frequency domain, page 13

$\mathbf{x}_{\mathrm{t}}$ Transmitted signal vector, page 12

$\mathbf{y}_{\mathrm{f}}$ Received signal vector in frequency domain, page 13

$\mathbf{y}_{\mathrm{t}}$ Received signal vector, page 12

$\mathcal{B}$ Set of subcarriers in a subband, page 43

$\mathcal{M}$ Set of UEs, page 82

$\mathcal{P}$ Set of PRBs, page 82

$\mathcal{S}$ Set of cells, page 13

$\overline{P}$ Average Rx power, page 47

ϕ Angle of departure, page 27

ψ Angle of arrival, page 20

σ^2 Variance, page 8

τ Delay, page 7

$\tau_{\max}$ Maximum delay spread, page 7

ε Mean squared error, page 63

$\widetilde{\mathbf{\Omega}}$ Element-wise square root of the power coupling matrix, page 25

ξ Complex amplitude, page 7

ζ Normalized complex amplitude, page 19

a PRB assignment parameter, page 93

c Speed of light, page 9

d Distance between base station and user, page 89

f_{D} Maximum Doppler frequency, page 8

f_{c} Carrier frequency, page 9

h Channel impulse response, page 7

k Subcarrier index, page 10

l Discrete delay index, page 7

n Discrete time index, page 10

n_{Rx} Index of receive antenna, page 12

n_{Tx} Index of transmit antenna, page 12

n_{sin} Index of sinusoid, page 20

r_{f} Frequency correlation, page 11

r_{t} Temporal correlation, page 8

t Time index, page 7

t_{d} Feedback delay, page 62

v Moving speed, page 9

x Transmitted signal, page 7

y Received signal, page 7

Abbreviations

3GPP 3rd Generation Partnership Project
ACF Auto-correlation Function
ACK Acknowledgment
AMC Adaptive Modulation And Coding
AoA Angle Of Arrival
AoD Angle Of Departure
AR Autoregressive
ARQ Automatic Repeat Request
AWGN Additive White Gaussian Noise
BLER Block Error Rate
BS Base Station
CC Chase Combining
CCI Co-channel Interference
CDF Cumulative Distribution Function
CFR Channel Frequency Response
CIR Channel Impulse Response
CORLA Cube Oriented 3D Ray Launching Algorithm
CQI Channel Quality Indicator
CRC Cyclic Redundancy Check
CSG Closed Subscriber Group
CSI Channel State Information
DFT Discrete Fourier Transform
DVB-T Digital Video Broadcasting - Terrestrial
E-UTRAN Evolved Universal Terrestrial Radio Access
EESM Effective Exponential SNR Mapping
eNB Evolved Node B
FEC Forward Error Correction
FFT Fast Fourier Transform

GSCM Geometry-based Stochastic Channel Model
HARQ Hybrid Automatic Repeat Request
HeNB Home Evolved Node B
HPBW Half Power Beam Width
HSS Home Subscription Server
HUE Home User Equipment
i.i.d. Independent And Identically Distributed
ICI Inter-cell Interference
IDFT Inverse Discrete Fourier Transform
IFFT Inverse Fast Fourier Transform
IIR Infinite Impulse Response
IP Internete Protocol
IR Incremental Redundancy
KPI Key Performance Indicator
LoS Line Of Sight
LSP Large Scale Parameter
LTE Long-term Evolution
LTE-A Long-term Evolution Advanced
MA Margin Adaptive
MAC Media Access Control
MCS Modulation And Coding Scheme
MIMO Multi-input Multi-output
MME Mobility Management Entity
MMSE Minimum Mean Squared Error
MPC Multi-path Component
MS Mobile Station
MSE Mean Squared Error
MUE Macrocell User Equipment
NACK Negative Acknowledgment
NLMS Normalized Least Mean Square
NLoS Non-line Of Sight
OFDM Orthogonal Frequency Division Multiplexing
OFDMA Orthogonal Frequency Division Multiple Access
OSM Open Street Map

P-GW PDN Gateway
PAS Power Azimuth Spectrum
PCCC Parallel Concatenated Convolutional Code
PDCCH Physical Downlink Control Channel
pdf Probability Density Function
PDP Power-delay Profile
PDSCH Physical Downlink Shared Channel
PF Proportional Fair
PHY Physical Layer
PIROPA Parallel Implemented Ray Optical Prediction Algorithm
PRB Physical Resource Block
PUCCH Physical Uplink Control Channel
PULPA Polarized Uniform Linear Patch Array
PUSCH Physical Uplink Shared Channel
QAM Quadrature Amplitude Modulation
QoS Quality Of Service
QPP Quadratic Permutation Polynomial
QPSK Quadrature Phase Shift Keying
RA Rate Adaptive
RE Resource Element
Rx Receive
S-GW Serving Gateway
SAE System Architecture Evolution
SCM Spatial Channel Model
SCME Spatial Channel Model Extension
SINR Signal To Interference Plus Noise Ratio
SIR Signal To Interference Ratio
SISO Single-input Single-output
SNR Signal To Noise Ratio
SON Self-organizing Network
SPUCPA Stacked Polarimetric Uniform Circular Patch Array
SSCM Semi-stochastic Channel Model
TTI Transmission Time Interval
Tx Transmit

Abbreviations

UE User Equipment
ULA Uniform Linear Array
UMTS Universal Mobile Telecommunications System
UP User Plane
V2V Vehicle-to-vehicle
VoIP Voice Over Internet Protocol
WINNER Wireless World Initiative New Radio
WLAN Wireless Local Area Network
WSS Wide-sense Stationary
WSSUS Wide-sense Stationary Uncorrelated-scattering

List of Tables

3.1 Parameters for deterministic stage and stochastic stage 32
3.2 Measurement setup of Ilmenau campaign 32

4.1 The 4-bit CQI table in LTE [8] 41
4.2 Optimal value for β in LTE 44
4.3 Minimum effective SNR for CQI feedback 44
4.4 Simulation parameters 58
4.5 Statistics of differences between neighboring CQI 65
4.6 HARQ model parameters for LTE 74

5.1 Co-tier and cross-tier interference table 91
5.2 Different types of service 92
5.3 Simulation parameters. 97
5.4 User mobility parameters. 97
5.5 Pathloss models. 99

List of Figures

2.1 Two dimensional structure of channel impulse response. 8
2.2 Power-delay profile for (a) typical urban, (b) bad urban, (c) rural area, (d) hilly terrain, from COST 207 [30]. The figures show the average power for each tap, normalized by the total power. 9
2.3 Two dimensional structure of CFR corresponds to CIR in Figure 2.1 . . 10
2.4 MIMO channel 12
2.5 Rx signal level of a network with 7 base stations and 21 cells in hexagonal layout, where the basestations are located on the joints of the hexagonal cells 14
2.6 LTE system architecture 15
2.7 LTE downlink signal generation 16

3.1 Multi-path propagation and movements of mobile station cause frequency selective time varying fading. 23
3.2 Deterministic channel models: (a) Ray-tracing; (b)Ray-launching. . . . 25
3.3 The relationship among the radio channel, the single directional channel and the double directional channel. 27
3.4 Clusterized multi-path MIMO channel model 28
3.5 Power-delay profiles for a NLoS environment in (a) Semi-stochastic channel model (b) WINNER model C2 scenario (typical urban macrocell) 30
3.6 Overview of Ilmenau measurement campaign 33
3.7 Measured CFR of path 9a-9b from Ilmenau data 34
3.8 Ergodic channel capacity for path 9a-9b 35
3.9 Equivalent baseband CIR for an OFDM system with 128 subcarriers . . 36
3.10 (a) Building information of a part of Munich. Building edges are marked with solid lines. (b) Reconstructed 2.5 D geographical data using uniform building height 38

4.1 Resource structure of LTE 40
4.2 SINR to CQI mapping for SISO transmission 41
4.3 BLER for CQI 1-15 in AWGN channel 42
4.4 SINR to effective SNR mapping for 4 PRBs, using EESM 43
4.5 Effective SNR to CQI mapping function, extracted from the BLER curves 45
4.6 Bandwidth efficiency of LTE with perfect CQI feedback, comparing to channel capacity 46
4.7 Time sequence for CQI feedback in LTE systems 47
4.8 Normalized autocovariance function and approximation 57

4.9 Approximated autocovariance function and simulation sample autocovariance with and without considering the location change of the UE . 59
4.10 Approximated autocovariance and its relationship to f_{D} 60
4.11 Estimated speed comparing to actual speed 61
4.12 Temporal variation of SINR and CQI values 62
4.13 (a) (b) (c): Simulated SINR curves for UE at 3 km/h, 10 km/h, 30 km/h, respectively. (d): at 30 km/h with additional boundary conditions $\Delta Q_{\max} = 1$, feedback delay is $t_{\mathrm{d}} = 10$ ms 66
4.14 MSE of predicted CQI value for single user 68
4.15 Average throughput for single user 68
4.16 Measured autocovariance function for UEs moving of different speeds . 69
4.17 Measured error distribution and Gaussian approximation at 50 km/h . 71
4.18 Average throughput for single user using Gaussian approximation . . . 71
4.19 Bandwidth efficiency for LTE with Gaussian distributed prediction noise 72
4.20 SNR gain due to HARQ retransmission at 10% BLER point for CQI 7 75
4.21 Bandwidth efficiency for LTE with Gaussian distributed prediction noise and HARQ 77
4.22 Bandwidth efficiency with biased predictor, $\sigma_\epsilon^2 = 100$ 79
4.23 Bandwidth efficiency with biased predictor, $\sigma_\epsilon^2 = 10$ 79
4.24 Latency for single user with HARQ 80
4.25 Success rate for single user with HARQ 80
4.26 Average throughput for single UE with HARQ, unlimited buffer 81
4.27 Average throughput for single UE with HARQ, limited buffer 81
4.28 Mean value of average throughput for multiple users 85
4.29 Fairness index for multiple users 85

5.1 Partial frequency sharing 88
5.2 3GPP electrical antenna tilt model 90
5.3 Co-tier and cross-tier interference in heterogeneous networks, interferences are marked in broken lines. Interferences from neighboring macrocells are not shown 91
5.4 Rx power in heterogeneous network 92
5.5 (a) Network layout with hexagonal grids. Horizontal and vertical lines denotes streets. (b) Dual stripe model. HeNBs are located in the center of apartments. 98
5.6 CDF of throughput for all HUEs 100
5.7 CDF of throughput for all MUEs 101
5.8 CDF of throughput for all UEs 102
5.9 Mean throughput for different data rate offset 103
5.10 Average user satisfaction rate for different data rate offset 103

Bibliography

[1] "Open street maps." [Online]. Available: www.openstreetmap.org

[2] 3GPP R4-092042, "Simulation assumptions and parameters for FDD HeNB RF requirements," Alcatel-Lucent, picoChip Designs, Vodafone.

[3] 3GPP TR 25.943 V8.0.0, "Technical specification group radio access network; deployment aspects," Dec. 2008.

[4] 3GPP TR 25.996 V8.0.0, "Technical specification group radio access network; spatial channel model for multiple input mlutiple output (MIMO) simulations," 2008.

[5] 3GPP TS 36.211 V8.9.0, "Evolved universal terrestrial radio access (E-UTRA); physical channels and modulation," Dec. 2009.

[6] 3GPP TS 36.212 V8.8.0, "Evolved universal terrestrial radio access (E-UTRA); multiplexing and channel coding," Dec. 2009.

[7] 3GPP TS 36.213 V10.11.0, "Evolved universal terrestrial radio access (E-UTRA); physical layer procedures," Dec. 2013.

[8] 3GPP TS 36.213 V8.8.0, "Evolved universal terrestrial radio access (E-UTRA); physical layer procedures," Sep. 2009.

[9] 3GPP TS 36.814 V9.0.0, "Evolved universal terrestrial radio access (E-UTRA); further advancements for E-UTRA physical layer aspects," Mar. 2010.

[10] M. Andrews, V. Capdevielle, A. Feki, and P. Gupta, "Autonomous spectrum sharing for mixed LTE femto and macro cells deployments," in *Computer Communications, IEEE Conference on (INFOCOM)*, San Diego, USA, Mar. 2010.

[11] D. Astely, E. Dahlman, A. Furuskar, Y. Jading, M. Lindstrom, and S. Parkvall, "LTE: the evolution of mobile broadband," *Communications Magazine, IEEE*, vol. 47, no. 4, pp. 44–51, Apr. 2009.

[12] T. Aulin, "A modified model for the fading signal at a mobile radio channel," *Vehicular Technology, IEEE Transactions on*, vol. 28, no. 3, pp. 182–203, Aug 1979.

[13] K. Baddour and N. Beaulieu, "Autoregressive modeling for fading channel simulation," *Wireless Communications, IEEE Transactions on*, vol. 4, no. 4, pp. 1650–1662, Jul. 2005.

[14] R. H. Bartels, J. C. Beatty, and B. A. Barsky, *An Introduction to Splines for Use in Computer Graphics and Geometric Modelling*. Morgan Kaufmann Publishers, 1998.

[15] D. Baum, J. Hansen, and J. Salo, "An interim channel model for beyond-3g systems: extending the 3gpp spatial channel model (scm)," in *Vehicular Technology Conference(VTC-Spring), IEEE 61st*, Stockholm, Sweden, May 2005.

[16] K. C. Beh, A. Doufexi, and S. Armour, "Performance evaluation of hybrid ARQ schemes of 3GPP LTE OFDMA system," in *Personal, Indoor and Mobile Radio Communications (PIMRC),IEEE 18th International Symposium on*, Athens, Greece, Sep. 2007.

[17] C. Berrou, A. Glavieux, and P. Thitimajshima, "Near shannon limit error-correcting coding and decoding: Turbo-codes," in *Communications (ICC), IEEE International Conference on*, Geneva, Switzerland, May 1993.

[18] D. Calin, H. Claussen, and H. Uzunalioglu, "On femto deployment architectures and macrocell offloading benefits in joint macro-femto deployments," *Communication Magazine, IEEE*, vol. 48, no. 1, pp. 26–32, 2010.

[19] J. A. L. Calvo, X. Xu, and F. Schröder, "Investigation on mobile radio propagation channel models based on measurement data," in *18th International Student Conference on Electrical Engineering*, Prague, Czech Republic, May 2014.

[20] J.-F. Cheng, A. Nimbalker, Y. Blankenship, B. Classon, and T. Blankenship, "Analysis of circular buffer rate matching for LTE turbo code," in *Vehicular Technology Conference (VTC-Fall), IEEE 68th*, Calgary, Canada, Sep. 2008.

[21] R. H. Clarke, "A statistical theory of mobile radio reception," *Bell Labs System Technical Journal*, vol. 47, pp. 957–1000, Jul-Aug 1968.

[22] H. Claussen, L. T. W. Ho, and L. G. Samuel, "Financial analysis of a pico-cellular home network deployment," in *Communications (ICC), IEEE International Conference on*, Glasgow, Scotland, Jun. 2007.

[23] ——, "Self-optimization of coverage for femtocell deployments," in *Wireless Telecommunications Symposium (WTS)*, Pomona, USA, Apr. 2008, pp. 278 – 285.

[24] R. Comroe and J. Costello, D.J., "ARQ schemes for data transmission in mobile radio systems," *Selected Areas in Communications, IEEE Journal on*, vol. 2, no. 4, pp. 472–481, Jul. 1984.

[25] T. Cui, F. Lu, V. Sethuraman, A. Goteti, S. P. Rao, and P. Subrahmanya, "First order adaptive IIR filter for CQI prediction in HSDPA," in *Wireless Communications and Networking Conference (WCNC), 2010 IEEE*, Sydney, Australia, Apr. 2010.

[26] N. Czink, X. Yin, H. Ozcelik, M. Herdin, E. Bonek, and B. Fleury, "Cluster characteristics in a MIMO indoor propagation environment," *Wireless Communications, IEEE Transactions on*, vol. 6, no. 4, pp. 1465–1475, Apr 2007.

[27] H. Dai, Y. Wang, C. Shi, and W. Zhang, "The evaluation of CQI delay compensation schemes based on Jakes' model and ITU scenarios," in *Vehicular Technology Conference. (VTC Fall). IEEE 76th*, Quebec, Canada, Sep. 2012.

[28] S. N. Donthi and N. B. Mehta, "An accurate model for EESM and its application to analysis of CQI feedback schemes and scheduling in LTE," *Wireless Communications, IEEE Transactions on*, vol. 10, no. 10, pp. 3436–3448, Oct. 2011.

[29] A. Engels, M. Reyer, X. Xu, R. Mathar, J. Zhang, and H. Zhuang, "Autonomous self-optimization of coverage and capacity in LTE cellular networks," *Vehicular Technology, IEEE Transactions on*, vol. 62, no. 5, pp. 1989–2004, 2013.

[30] M. Falli, Ed., *COST 207 : Digital land mobile radio communications: Final report*. Luxembourg: Office for Official Publications of the European Communities, 1989.

[31] G. J. Foschini, "Layered space-time architecture for wireless communication in a fading environment when using multi-element antennas," *Bell Lab Technical Journal*, vol. 1, no. 2, pp. 41–59, 1996.

[32] P. Frenger, S. Parkvall, and E. Dahlman, "Performance comparison of HARQ with chase combining and incremental redundancy for hsdpa," in *Vehicular Technology Conferenc (VTC Fall), IEEE 54th*, Atlantic City, NJ, USA, Oct 2001.

[33] M. Gans, "A power-spectral theory of propagation in the mobile-radio environment," *Vehicular Technology, IEEE Transactions on*, vol. 21, no. 1, pp. 27–38, Feb 1972.

[34] L. Gavrilovska and D. Talevski, "Novel scheduling algorithms for LTE downlink transmission," in *19th Telecommunications Forum (TELFOR)*, Nov. 2011.

[35] M. Goldenbaum, R. Akl, S. Valentin, and S. Stanczak, "On the effect of feedback delay in the downlink of multiuser ofdm systems," in *Information Sciences and Systems (CISS), 2011 45th Annual Conference on*, Baltimore, MD, USA, Mar 2011.

[36] A. Goldsmith, S. Jafar, N. Jindal, and S. Vishwanath, "Capacity limits of MIMO channels," *Selected Areas in Communications, IEEE Journal on*, vol. 21, no. 5, pp. 684–702, Jun. 2003.

[37] Y. J. Guo, *Advances in Mobile Radio Access Networks*. Artech House, 2004.

[38] D. He, G. Liang, J. Portilla, and T. Riesgo, "A novel method for radio propagation simulation based on automatic 3D environment reconstruction," in *Antennas and Propagation (EUCAP), 6th European Conference on*, Prague, Czech, March 2012.

[39] H. Holma and A. Toskala, Eds., *LTE for UMTS: OFDMA and SC-FDMA Based Radio Access*. John Wiley & Sons, Ltd., 2009.

[40] *IEEE Standard for Information Technology- Local and Metropolitan Area Networks- Specific Requirements- Part 11: Wireless LAN Medium Access Control (MAC) and Physical Layer (PHY) Specifications Amendment 5: Enhancements for Higher Throughput*, IEEE Computer Society 802.11 n Std., Oct 2009.

[41] J. C. Ikuno, M. Wrulich, and M. Rupp, "Performance and modeling of LTE H-ARQ," in *International Workshop on Smart Antennas (WSA)*, Berlin, Germany, Feb. 2009.

[42] J. Ikuno, S. Pendl, M. Simko, and M. Rupp, "Accurate SINR estimation model for system level simulation of LTE networks," in *Communications (ICC), IEEE International Conference on*, Ottawa, Canada, Jun 2012.

[43] M. A. Ismail, X. Xu, and R. Mathar, "Autonomous antenna tilt and power configuration based on CQI for LTE cellular networks," in *The 10th International Symposium on Wireless Communication Systems (ISWCS)*, Ilmenau, Germany, Aug. 2013, pp. 405–409.

[44] IST-WINNER II D1.1.2 V1.2, "WINNER II Channel Model IST-4-027756," 2007, http://www.ist-winner.org.

[45] W. C. Jakes, *Microwave Mobile Communications*. Piscataway, NJ: IEEE Press, 1994.

[46] A. Jalali, R. Padovani, and R. Pankaj, "Data throughput of CDMA-HDR a high efficiency-high data rate personal communication wireless system," in *Vehicular Technology Conference (VTC Spring), IEEE 51st*, Tokyo, Japan, May 2000.

[47] E. Jorswieck and H. Boche, "Optimal transmission strategies and impact of correlation in multiantenna systems with different types of channel state information," *Signal Processing, IEEE Transactions on*, vol. 52, no. 12, pp. 3440–3453, 2004.

[48] V. J. Katz, "Change of variables in multiple integrals: Euler to Cartan," *Mathematics Magazine*, vol. 55, no. 1, pp. 3–11, Jan 1982.

[49] P. Kela, J. Puttonen, N. Kolehmainen, T. Ristaniemi, T. Henttonen, and M. Moisio, "Dynamic packet scheduling performance in UTRA Long Term Evolution downlink," in *Wireless Pervasive Computing (ISWPC), 3rd International Symposium on*, Santorini, Greece, May 2008.

[50] J. Kermoal, L. Schumacher, K. Pedersen, P. Mogensen, and F. Frederiksen, "A stochastic MIMO radio channel model with experimental validation," *Selected Areas in Communications, IEEE Journal on*, vol. 20, no. 6, pp. 1211–1226, Aug. 2002.

[51] F. Khan, *LTE for 4G Mobile Broadband: Air Interface Technologies and Performance*, 1st ed. Cambridge University Press, 2009.

[52] K.-H. Li, M.-A. Ingram, and A. Van Nguyen, "Impact of clustering in statistical indoor propagation models on link capacity," *Communications, IEEE Transactions on*, vol. 50, no. 4, pp. 521–523, Apr 2002.

[53] Y. G. Li and G. L. Stüber, Eds., *Orthogonal Frequency Division Multiplexing for Wireless Communications*. Springer, 2006.

[54] J. Ling, D. Chizhik, and R. Valenzuela, "Predicting multi-element receive and transmit array capacity outdoors with ray tracing," in *Vehicular Technology Conference (VTC Spring), IEEE 53rd*, Rhodes, Greece, May 2001.

[55] C. Liu, A. Schmeink, and R. Mathar, "Dual optimal resource allocation for heterogeneous transmission in OFDMA systems," in *Globecom, IEEE*, Honolulu, Hawaii, USA, Dec. 2009.

[56] Z. Lu, Y. Sun, X. Wen, T. Su, and D. Ling, "An energy-efficient power control algorithm in femtocell networks," in *Computer Science Education (ICCSE), 7th International Conference on*, Melbourne, Australia, Jul 2012.

[57] H. Mahmoud and I. Guvenc, "A comparative study of different deployment modes for femtocell networks," in *Personal, Indoor and Mobile Radio Communications, IEEE 20th International Symposium on (PIMRC)*, Tokyo, Japan, Sep. 2009.

[58] R. Mathar, M. Reyer, and M. Schmeink, "A cube oriented ray launching algorithm for 3D urban field strength prediction," in *Communications (ICC), IEEE International Conference on*, Glasgow, Scotland, Jun. 2007.

[59] J. Mietzner, C. Xiao, P. Hoeher, and K. Ben Letaief, "A note on discrete-time triply-selective MIMO Rayleigh fading channel models," *Wireless Communications, IEEE Transactions on*, vol. 7, no. 3, pp. 837–837, 2008.

[60] M. Morita, Y. Matsunaga, and K. Hamabe, "Adaptive power level setting of femtocell base stations for mitigating interference with macrocells," in *Vehicular Technology Conference Fall (VTC Fall), IEEE 72nd*, Ottawa, Canada, Sep. 2010.

[61] L. Nagy, "Comparison and application of FDTD and ray optical method for indoor wave propagation modeling," in *Antennas and Propagation (EuCAP), the Fourth European Conference on*, Barcelona, Spain, Apr. 2010.

[62] M. Narandzic, C. Schneider, R. Thoma, T. Jamsa, P. Kyosti, and X. Zhao, "Comparison of SCM, SCME, and WINNER channel models," in *Vehicular Technology Conference (VTC Spring), IEEE 65th*, Dublin, Ireland, Apr. 2007.

[63] M. Ni, "Channel quality feedback strategies for LTE networks," Master's thesis, RWTH-Aachen University, Aachen, Germany, Dec 2012.

[64] M. Ni, X. Xu, and R. Mathar, "A channel feedback model with robust SINR prediction for LTE systems," in *The 7th European conference on antennas and propatation (EuCAP)*, Gothenburg, Sweden, Apr 2013.

[65] A. Nimbalker, Y. Blankenship, B. Classon, and T. Blankenship, "ARP and QPP interleavers for LTE turbo coding," in *Wireless Communications and Networking Conference (WCNC), IEEE*, Las Vegas, USA, Mar. 2008.

[66] J. O'Carroll, H. Claussen, and L. Doyle, "Partial GSM spectrum reuse for femtocells," in *Personal, Indoor and Mobile Radio Communications, IEEE 20th International Symposium on (PIMRC)*, Tokyo, Japan, Sep. 2009.

[67] H. Ozcelik, N. Czink, and E. Bonek, "What makes a good MIMO channel model?" in *Vehicular Technology Conference (VTC Spring), IEEE 61st*, Stockholm, Sweden, May 2005.

[68] H. Ozcelik, M. Herdin, W. Weichselberger, J. Wallace, and E. Bonek, "Deficiencies of 'Kronecker' MIMO radio channel model," *Electronics Letters*, vol. 39, no. 16, pp. 1209–1210, 2003.

[69] M. Pop and N. Beaulieu, "Limitations of sum-of-sinusoids fading channel simulators," *Communications, IEEE Transactions on*, vol. 49, no. 4, pp. 699–708, Apr 2001.

[70] T. S. Rappaport, *Wireless Communications: Principles and Practice*, 2nd ed. Prentice Hall PTR, 2002.

[71] A. A. M. Saleh and R. A. Valenzuela, "A statistical model for indoor multipath propagation," *IEEE Journal on Selected Areas in Communications*, vol. 5, no. 2, pp. 128–137, Feb 1987.

[72] N. Saquib, E. Hossain, L. B. Le, and D. I. Kim, "Interference management in OFDMA femtocell networks: issues and approaches," *Wireless Communications, IEEE*, vol. 19, no. 3, pp. 86–95, 2012.

[73] C. Schneider, G. Sommerkorn, and C. Jandura, "Multi-user MIMO channel reference data for channel modelling and system evaluation from measurements," in *Smart Antennas (WSA), International ITG Workshop on*, Berlin, Feb 2009.

[74] F. Schröder, M. Reyer, and R. Mathar, "Efficient implementation and evaluation of parallel radio wave propagation," in *5th European Conference on Antennas and Propagation (EuCAP)*, Rome, Italy, Apr. 2011.

[75] S. Schwarz, C. Mehlfuhrer, and M. Rupp, "Low complexity approximate maximum throughput scheduling for LTE," in *Signals, Systems and Computers (ASILOMAR), the 44th Asilomar Conference on*, Pacific Grove, CA, USA, Nov 2010.

[76] E. Seidel and E. Saad, "LTE home node BS and its enhancements in release 9," Nomor Research White Paper, May 2010.

[77] Z. Shen, J. Andrews, and B. Evans, "Adaptive resource allocation in multiuser OFDM systems with proportional rate constraints," *Wireless Communications, IEEE Transactions on*, vol. 4, no. 6, pp. 2726–2737, Nov 2005.

[78] H. Shin and M. Win, "MIMO diversity in the presence of double scattering," *Information Theory, IEEE Transactions on*, vol. 54, no. 7, pp. 2976–2996, 2008.

[79] D.-S. Shiu, G. Foschini, M. Gans, and J. Kahn, "Fading correlation and its effect on the capacity of multielement antenna systems," *Communications, IEEE Transactions on*, vol. 48, no. 3, pp. 502–513, 2000.

[80] M. Steinbauer, A. Molisch, and E. Bonek, "The double-directional radio channel," *Antennas and Propagation Magazine, IEEE*, vol. 43, no. 4, pp. 51–63, Aug. 2001.

[81] G. Stüber, *Principles of Mobile Communication*, 2nd ed. Kluwer Academic Publishers, 2002.

[82] S. Talakoub, L. Sabeti, B. Shahrrava, and M. Ahmadi, "A linear log-MAP algorithm for turbo decoding and turbo equalization," in *Wireless and Mobile Com-*

puting, Networking and Communications (WiMob), IEEE International Conference on, Montreal, Canada, Aug 2005.

[83] I. E. Telatar, "Capacity of multi-antenna gaussian channels," *European Transactions on Telecommunications*, vol. 10, no. 6, pp. 585–595, 1999.

[84] H. Touheed, A. U. Quddus, and R. Tafazolli, "Predictive CQI reporting for HSDPA," in *Personal, Indoor and Mobile Radio Communications. PIMRC. IEEE 19th International Symposium on*, Sep. 2008.

[85] R. Valenzuela, "A ray tracing approach to predicting indoor wireless transmission," in *Vehicular Technology Conference, 1993 IEEE 43rd*, May 1993, pp. 214–218.

[86] A. van Zelst and J. S. Hammerschmidt, "A single coefficient spatial correlation model for multiple-input multiple-output (MIMO) radio channel," in *URSI XXVIIth General Assembly*, Maastricht, the Netherlands, Aug 2002.

[87] W. Weichselberger, M. Herdin, H. Ozcelik, and E. Bonek, "A stochastic MIMO channel model with joint correlation of both link ends," *Wireless Communications, IEEE Transactions on*, vol. 5, no. 1, pp. 90–100, Jan. 2006.

[88] A. Winkelbauer, "Moments and absolute moments of the normal distribution," arXiv:1209.4340 [math.ST], Sep 2012.

[89] G. Wölfle, R. Hoppe, and F. M. Landstorfer, "A fast and enhanced ray optical propagation model for indoor and urban scenarios, based on an intelligent preprocessing of the database," in *10th IEEE International Symposium on Personal, Indoor, and Mobile Radio Communications (PIMRC)*, Osaka, 1999.

[90] C. Xiao, J. Wu, S.-Y. Leong, Y. Zheng, and K. Letaief, "A discrete-time model for triply selective MIMO rayleigh fading channels," *Wireless Communications, IEEE Transactions on*, vol. 3, no. 5, pp. 1678–1688, 2004.

[91] C. Xiao, Y. R. Zheng, and N. Beaulieu, "Novel sum-of-sinusoids simulation models for Rayleigh and Rician fading channels," *Wireless Communications, IEEE Transactions on*, vol. 5, no. 12, pp. 3667 –3679, Dec 2006.

[92] H. Xu, D. Chizhik, H. Huang, and R. Valenzuela, "A generalized space-time multiple-input multiple-output (MIMO) channel model," *Wireless Communications, IEEE Transactions on*, vol. 3, no. 3, pp. 966–975, May 2004.

[93] X. Xu and R. Mathar, "Low complexity joint channel estimation and decoding for LDPC coded MIMO-OFDM systems," in *Vehicular Technology Conference (VTC Spring), IEEE 73rd*, Budapest, Hungary, May 2011.

[94] X. Xu, G. Kutrolli, and R. Mathar, "Autonomous downlink power control for LTE femtocells based on channel quality indicator," in *IEEE 24th International Symposium on Personal, Indoor and Mobile Radio Communications: Mobile and Wireless Networks (PIMRC)*, London, UK, Sep. 2013.

[95] ——, "Dynamic downlink power control strategies for LTE femtocells," in *7th International Conference on Next Generation Mobile Applications, Services, and Technologies (NGMAST)*, Prague, Czech, Sep. 2013.

[96] ——, "Energy efficient power management for 4G heterogeneous cellular networks," in *IEEE 9th International Conference on Wireless and Mobile Computing, Networking and Communications (WiMob)*, Lyon, France, Oct. 2013.

[97] X. Xu and R. Mathar, "Factor graph based detection and channel estimation for MIMO-OFDM systems in doubly selective channel," in *th International Symposium on Wireless Communication Systems (IEEE ISWCS)*, York, United Kingdom, Sep. 2010.

[98] ——, "Autoregressive modeling of frequency selective channels for synchronized OFDM systems," in *6th European Conference on Antennas and Propagation (EUCAP)*, Prague, Czech, Mar. 2012.

[99] X. Xu, M. Ni, and R. Mathar, "Improving QoS by predictive channel quality feedback for LTE," in *21st International Conference on Software Telecommunications and Computer Networks (Softcom)*, Primosten, Croatia, Sep. 2013.

[100] X. Xu, T. N. Pham, and R. Mathar, "Second-order statistics of channel state information in a multi-cell mobile network with fast fading," in *IEEE 25th International Symposium on Personal, Indoor and Mobile Radio Communications: Mobile and Wireless Networks (PIMRC)*, Washington DC, USA, Sep. 2014.

[101] X. Xu, M. Reyer, F. Schröder, A. Engels, and R. Mathar, "A semi-stochastic radio propagation model for wireless MIMO channels," in *8th International Symposium on Wireless Communication Systems (ISWCS)*, Aachen, Germany, Nov. 2011.

[102] X. Xu, F. Schröder, B. Gevreckce, G. Kutrolli, M. Ni, and R. Mathar, "A physical layer simulator based on radio wave propagation for LTE cellular networks," in *7th European Conference on Antennas and Propagation (EuCAP)*, Gothenburg, Sweden, Apr. 2013.

[103] D. Young and N. Beaulieu, "The generation of correlated Rayleigh random variates by inverse discrete Fourier transform," *Communications, IEEE Transactions on*, vol. 48, no. 7, pp. 1114–1127, Jul. 2000.

[104] Y. R. Zheng and C. Xiao, "Simulation models with correct statistical properties for Rayleigh fading channels," *Communications, IEEE Transactions on*, vol. 51, no. 6, pp. 920–928, Jun. 2003.

Curriculum Vitae

Xiang Xu

14.10.1982	Born in Chaohu, Anhui province, China
09.1988 - 07.1994	Chaohu Renminlu Primary School, China
09.1994 - 07.1997	Chaohu No. 1 Middle School, China
09.1997 - 07.2000	Chaohu No. 1 High School, China
07.2000	Secondary School Diploma National College Entrance Examination, China
09.2000 - 07.2004	Department of Electronic Science and Technology University of Science and Technology of China, Hefei, China
07.2004	Bachelor of Science in Electrical Engineering
07.2004 - 09.2004	Internship, China Telecom
10.2004 - 07.2005	International Education College Tongji University, Shanghai, China
10.2005 - 12.2007	Faculty of Engineering Christian-Albrechts-University of Kiel, Germany
11.2007	Master of Science in Digital Communications
03.2008 - 12.2010	Scholarship holder in DFG graduate school "Software for Mobile Communication Systems", RWTH-Aachen University
From 01.2011	Scientific staff in Institute for Theoretical Information Technology RWTH-Aachen University